# TO AUGMENT OR NOT TO AUGMENT? DIAGNOSING DISTRIBUTIONAL SYMMETRY BREAKING

**Anonymous authors**
Paper under double-blind review

## ABSTRACT

Symmetry-aware methods for machine learning, such as data augmentation and equivariant architectures, encourage correct model behavior on all transformations (e.g. rotations or permutations) of the original dataset. These methods can improve generalization and sample efficiency, under the assumption that the transformed datapoints are highly probable, or "important", under the test distribution. In this work, we develop a method for critically evaluating this assumption. In particular, we propose a metric to quantify the amount of anisotropy, or symmetry-breaking, in a dataset, via a two-sample neural classifier test that distinguishes between the original dataset and its randomly augmented equivalent. We validate our metric on synthetic datasets, and then use it to uncover surprisingly high degrees of anisotropy in several benchmark point cloud datasets. We show theoretically that distributional symmetry-breaking can actually prevent invariant methods from performing optimally even when the underlying labels are truly invariant, as we show for invariant ridge regression in the infinite feature limit. Empirically, we find that the implication for symmetry-aware methods is dataset-dependent: equivariant methods still impart benefits on some anisotropic datasets, but not others. Overall, these findings suggest that understanding equivariance — both when it works, and why — may require rethinking symmetry biases in the data.

## 1 INTRODUCTION

By integrating physical symmetries into the model architecture as group invariances, equivariant neural networks often achieve superior performance across materials science (Liao et al., 2023), robotics (Wang et al., 2024a), drug discovery (Igashov et al., 2024), fluid dynamics (Wang et al., 2021), computer vision (Esteves et al., 2019), and beyond. The success of equivariant methods is typically explained in terms of improved sample efficiency and generalizability, resulting from the ability to relate data sample $x$ and transformed data sample $gx$ (Cohen & Welling, 2016b). For $g \in G$ a group symmetry transformation, such as a rotation or permutation, a function $f$ is equivariant if $f(gx) = g(fx)$, and invariant if $f(gx) = f(x)$. Similarly, a model NN is equivariant if it is architecturally constrained such that $\mathrm{NN}(gx) = g\,\mathrm{NN}(x)$, tying the predictions for $x$ and $gx$.. Alternatively, data augmentation may be used to enforce equivariance by applying a random $g$ to each input $x$ in the training set and its corresponding label. For all of these equivariance methods, it is an *explicit assumption* that the ground truth function $f$ is equivariant (Thomas et al., 2018; Cohen & Welling, 2016a; Cohen et al., 2018). However, there is also often an *implicit assumption* that transformed samples $gx$ occur relatively uniformly in distribution, i.e. the input density $p(x) \approx p(gx)$. Theoretical results on the benefits of equivariance and data augmentation almost always assume that $x$ and $gx$ are equally likely under the data distribution (Elesedy & Zaidi, 2021; Chen et al., 2020; Mei et al., 2021).

In this paper, we study *distributional symmetry breaking* (Wang et al., 2024b;d)—when a datapoint $x$ and its transform $gx$ are *not* equally likely under the data distribution. Formally, this means that for a data distribution $p_X : X \to \mathbb{R}$, some $x \in X$, and some $g \in G$, $p_X(x) \neq p_X(gx)$. One can also view this in terms of the orbit of $x$ under $G$, defined as $\{gx\}_{g \in G}$: distributional symmetry breaking occurs when samples within the orbit are not equally likely. This paper takes a step towards the goal of understanding how distributional symmetry breaking affects the performance of equivariant methods, including the ubiquitous practice of data augmentation. Intuitively, although equivariance can help performance by providing the correct inductive bias on all transformations of the input data, it may

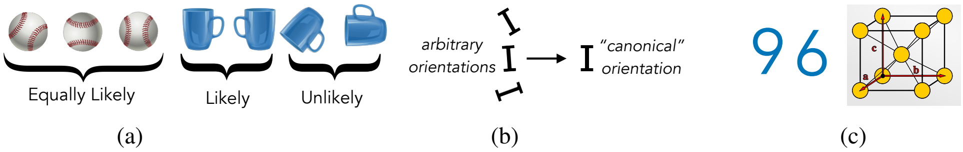

Figure 1: (a) **Distributional symmetry breaking**: Baseballs are likely to occur in any orientation in photos, and are therefore uniform across orbits. In contrast, coffee mugs are more likely to appear with the handle on the side. The latter is an example of distributional symmetry breaking. (b) **Canonicalization**: Canonicalization is when an object only ever appears in one, "canonical", orientation. This is the strongest form of distributional symmetry breaking. (c) **Inherent vs. user-defined canonicalization**: Datapoints can be canonicalized for reasons that are inherent, such as the orientation of a digit determining whether it is a 6 or a 9. However, it can also be user-defined, such as the orientation of a crystal lattice, without any deeper connection to the data-generating process.

also discard useful information. For example, consider the oft-discussed example of classifying "6"s and "9"s in the MNIST dataset. The two digits look very similar[1] when rotationally aligned, but are easily distinguishable under their naturally occurring orientations. Thus under rotational augmentation, this task becomes much more difficult. In general, this discarded orientation information may be *inherent*, such as the previous MNIST example, or *user-defined*, such as the conventions used to orient crystal structures (Figure 1). In practice, Cohen et al. (2018) demonstrated that rotational equivariance only improves performance on MNIST when the dataset is artificially rotated. Thus at a high level, distributional symmetry breaking can impact how non-equivariant methods perform relative to equivariant methods in-distribution.

Yet, quantifying the amount of symmetry breaking in a distribution remains challenging, particularly in the absence of domain knowledge (Wang et al., 2024b; 2023; 2024d). We thus propose a metric to measure the degree of distributional symmetry breaking, which can place a distribution on the spectrum between fully symmetrized (or "isotropic") on one side where all points in each orbit $\{gx\}_{g\in G}$ are in distribution, and fully canonicalized—where only a single sample $x$ in each orbit $\{gx\}_{g\in G}$ is in distribution—on the other (Figure 1). We note that canonicalization corresponds to a case of strong distributional symmetry breaking with explicit orientational alignment. We hope this metric will prove useful both as a practical, easily implementable tool for data exploration, and as a lens for rethinking the more fundamental questions of why, and when, equivariant methods succeed.

Concretely, we propose a two-sample classifier test (Lopez-Paz & Oquab, 2017), in which a model is trained to distinguish between samples from $p_X$ (the original data distribution) and $\bar{p}_X$ (the augmented data distribution) (Figure 2). The accuracy of this classifier on a held-out test set is a natural, *interpretable* measure, between 0 and 1.0, of distance between $p_X$ and $\bar{p}_X$. This (1) allows for interpretability methods (applied to the classifier itself), and (2) sidesteps the kernel selection required by Chiu & Bloem-Reddy (2023) in their tests for distributional symmetry, offloading it to the less impactful choice of architecture. Applying this metric to a variety of datasets, including QM9 (Wu et al., 2017), revised MD17 (Christensen & von Lilienfeld, 2020), OC20 (Chanussot* et al., 2021), and ModelNet40 (Wu et al., 2015), we find that all are highly non-uniform under 3D rotations.

Complementing these empirical findings, we provide nuanced theory on the trade-offs between different equivariant methods under distributional symmetry-breaking, and show equivariant methods can be harmful depending on properties of the data distribution. We use ridge(less) regression as a model, which captures some of the behavior of neural networks when applied in the neural tangent kernel space (D'Ascoli et al., 2020; Atanasov et al., 2023; Jacot et al., 2018). We show that even when the ground-truth function is invariant, data augmentation can be harmful when invariant and non-invariant features are strongly correlated. As our main contributions, we:

[1] Distributional symmetry breaking differs from *functional symmetry breaking* (Wang et al., 2024d), where the mapping between inputs and outputs is not fully equivariant (e.g. during a phase transition in a material). For the purposes of this paper, we treat "6" and "9" as distinct digits that simply look similar — distributional, not functional, symmetry breaking. This is supported by the observation in e.g. Wang et al. (2024b) that they can be correctly classified with high accuracy.

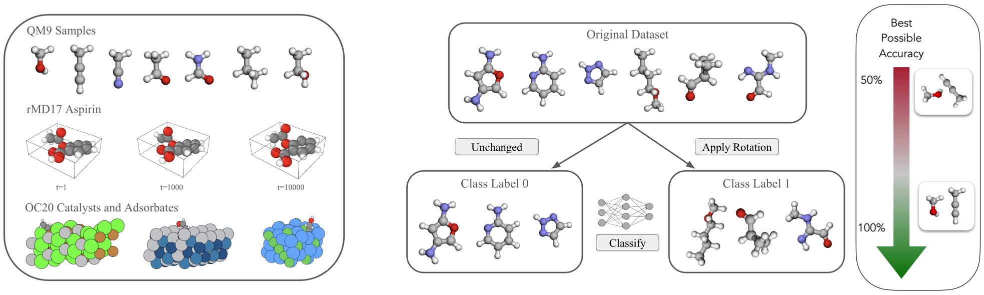

Figure 2: (left) Visualizations of unrotated samples from several materials datasets, with their canonicalization visible. (right) A classifier test for determining if a sample is from the original dataset, or rotated. With no distributional symmetry breaking, then no classifier can achieve better than 50% test accuracy. However, if the original dataset was fully canonicalized, the classifier can theoretically achieve perfect accuracy (for an infinite group; otherwise, $1-1/(2|G|)$).

- Define a flexible metric for measuring distributional symmetry breaking in a dataset (Section 2). This is a tool for probing datasets' symmetry biases without *a priori* knowledge of their creation.
- Provide a novel theoretical analysis of invariant ridge regression under distributional asymmetry, showing that data augmentation sometimes hurts (Section 4).
- Use our metric to discover that point cloud benchmarks, including QM9 and ModelNet40, are highly canonicalized (Section 5). We correspondingly evaluate the impact of equivariant methods (augmentation, constrained architecture, and stochastic averaging), and find surprising results on the relation to distributional symmetry breaking.

## 2 Proposed Metric

Consider data points $x \in \mathscr{X}$ drawn from a distribution $p_X$, acted on by a compact group $G$. We assume that there is a ground truth labeling function $f : \mathscr{X} \to \mathscr{Y}$ that is equivariant, i.e. $f(gx) = gf(x)$. We do *not* assume that $p_X(x) = p_X(gx)$; instead, we wish to quantify the degree to which $p_X$ breaks distributional symmetry by failing to satisfy this equality, i.e., **to define a metric** $m(p_X)$ **which measures how close** $p_X$ **is to symmetric.** To this end, define the symmetrized density $\bar{p}_X(x) := \int_{g\in G} p_X(gx)dg$. The density $\bar{p}_X$ is the closest invariant distribution to $p_X$: for any $G$-invariant measure $\mu$ on $\mathscr{X}$ it minimizes $\int_x (i(x) - p_X(x))^2 d\mu(x)$ over all invariant densities $i$.

We assume a dataset of samples from $p_X$, and obtain samples from $\bar{p}_X$ by applying random $G$-augmentations. As our metric of distributional symmetry breaking, we now wish to approximate some notion of distance $d$ between $p_X$ and $\bar{p}_X$ based on a finite number of samples — but this is not straightforward to choose or compute.

Chiu & Bloem-Reddy (2023) set $d$ to be the maximum mean discrepancy (MMD) with respect to some choice of kernel, corresponding to a non-parametric two sample statistical test. However, there is not always a clear choice of kernel. For example, for materials datasets of geometric graphs, Chiu & Bloem-Reddy (2023) do not provide an applicable kernel that includes chemical information. Rectifying this requires choosing a kernel suitable for $\mathscr{X}$, which may be non-trivial, and as noted in Lopez-Paz & Oquab (2017), may not return values in units that are directly interpretable.

We propose instead applying a two sample classifier test, a common tool for detecting and quantifying distribution shift in machine learning (Lopez-Paz & Oquab, 2017). We train a small neural network NN to distinguish between distributions as a binary classification task, and define the distance $d$ between distributions as the *test* accuracy:

$$d_{class}(p_0, p_1) = \mathbb{E}_{c\sim \text{Bern}(\frac{1}{2})} \mathbb{E}_{x\sim p_c} \left[ \mathbb{1}\big(\text{NN}(x) = c\big) \right].$$

Our metric is then $m(p_X) := d_{class}(p_X, \bar{p}_X)$. Concretely, we construct a binary classification dataset from an original dataset as shown in Figure 2 and Algorithm 1, with half of the dataset transformed by random group elements (label 1), and the rest unchanged (label 0).

**Algorithm 1** Metric for Distributional Symmetry Breaking, $m(p_X)$

```
Inputs: Unlabeled train/test sets $\mathscr{D}_{train}$ and $\mathscr{D}_{test}$, group $G$, binary classifier network NN
For $split \in \{train, test\}$:
    Randomly divide $\mathscr{D}_{split}$ into equally sized $D_{split}$ and $\widetilde{D}_{split}$
    For each $x \in \widetilde{D}_{split}$, uniformly sample $g \sim G$ and apply $g$ to $x$
    Define classification dataset $D^c_{split} := \{(x,0) : x \in D_{split}\} \cup \{(x,1) : x \in \widetilde{D}_{split}\}$
Train binary classifier NN on the dataset $D^c_{train}$ with the standard BCE loss
Return NN's test accuracy, $\mathbb{E}_{(x,c)\in D^c_{test}}\left[\mathbb{1}\left(\text{NN}(x) = c\right)\right]$
```

**Interpretation of $m(p_X)$** The trained classifier's test accuracy is easily interpretable, reflecting how often it can distinguish between the original and symmetrized distributions. If $p_X$ is already group-invariant, then $p_X = \bar{p}_X$ and no network can reliably distinguish between samples from the two, so $m(p_X) \approx 1/2$. If in contrast $p_X$ is canonicalized in a discernable way, then $m(p_X) \approx 1$.

To build intuition for how $m(p_X)$ interpolates between these two extremes, let us also compute it for the case of a finite group, with a dataset consisting of a single orbit $\{gx_1 : g \in G\} := \{x_1, x_2, \ldots x_r\}$. Parametrize the data distribution as $p(x_i) = \theta_i$, $\sum_i \theta_i = 1$. What is the optimal classification accuracy between a uniform distribution over $x_1, x_2, \ldots x_r$ (class 1), and $p$ (class 0), under infinite samples? For each $i$, the optimal classifier assigns 1 if $\frac{1}{r} > \theta_i$, and 0 otherwise. The resulting optimal accuracy is $c(p_X) := 1 - \frac{1}{2}\sum_{i=1}^r \min(\frac{1}{r}, \theta_i)$. For example, for a multimodal distribution with probability mass equally distributed among $m$ modes, the best possible accuracy is $1 - \frac{m}{2r}$, which interpolates between $\frac{1}{2}$ when $m = r$ and $1 - \frac{1}{2r}$ for a perfectly canonicalized distribution. In this analysis, we have assumed infinite samples, an adequately expressive NN, and perfect optimization (although it is accurate for MNIST; see section 5). In reality, these factors will affect $m(p_X)$, although ablations (Table 7) indicate little sensitivity to the size of NN. For an infinite group (e.g. $SO(3)$), we instead have $m(p_X) \leq 1$, and rely on a validation set to avoid overfitting.

## 3 Related Work

**Learning symmetry breaking** Several works seek to discover *functional symmetry breaking*, where the task may be only partially, rather than fully equivariant, i.e. there are some $x$ and $g$ such that $f(gx) \neq gf(x)$ (Wang et al., 2024d; Finzi et al., 2021; McNeela, 2023; Hofgard et al., 2024; Smidt et al., 2021; Urbano & Romero, 2024a). We distinguish this (more common) notion from our focus, *distributional symmetry breaking* ($p(x) \neq p(gx)$), which Wang et al. (2023; 2024c) showed can harm the performance of equivariant models. Indeed, several works proposing equivariant methods have noted that the improvement of their method relative to baselines relies on applying test-time augmentations (Cohen et al., 2018; Kaba et al., 2023). This motivates our method.

**Learning how to augment** Learning an augmentation distribution is one way to address either kind of symmetry breaking. Benton et al. (2020a) address functional symmetry breaking by learning an augmentation distribution. For example, Miao et al. (2023) encode an input using an invariant network, then use this encoding to sample from a learned distribution, feeding randomly transformed inputs into a classifier. Urbano & Romero (2024b) pursue a similar goal in a self-supervised setting, and show their method can be used to canonicalize data, or detect when an input is transformed out of distribution. Learning to predict transformations applied to data, which is possible only with distributional symmetry breaking, was proposed for representation learning by Gidaris et al. (2018).

**Detecting distributional symmetry** In the unsupervised setting, Desai et al. (2022) and Yang et al. (2023) train discriminative networks for symmetry discovery in a similar way to our binary classifier, but do not produce a quantitative measure of distributional asymmetry on benchmarks. Chiu & Bloem-Reddy (2023) consider non-parametric hypothesis tests for distributional symmetry, and use the distance between the group-averaged and original distributions as the test statistic. Soleymani et al. (2025) devise a robust kernel test for invariance, where a witness $g \in G$ must be provided to prove $p$ is non-invariant. Charvin et al. (2023) propose an information theoretic framework for detecting distributional *equivariance* (rather than invariance, as we consider here).

**Pros and cons of invariant methods** Our theoretical work follows up on Elesedy & Zaidi (2021); Chen et al. (2020), who show that when $p_x$ is invariant, symmetrization or data augmentation improve risk. Most existing work that studies the benefits of invariance in over-parameterized settings similar to ours also assumes invariant $p_x$ (Mei et al., 2021; Bietti et al., 2021). On the limitations of invariant methods, Shao et al. (2024) established that any equivariant algorithm applied to extrinsically equivariant data, under certain assumptions on the hypothesis class, cannot obtain optimal sample complexity in terms of PAC learnability. Lin et al. (2024); Huang et al. (2025) also study unexpected effects of data augmentation, although not focusing on the effects of symmetry.

## 4 Theory: Invariant Regression under Data Asymmetry

To exhibit the subtleties of distributional symmetry-breaking, we analyze high-dimensional ridge regression under non-symmetric covariance. We show that even when the ground-truth function is invariant, *data augmentation and symmetrization can be harmful when invariant and non-invariant features are strongly correlated.* This is intuitive: a non-invariant feature is useful for an invariant task if it correlates well with an invariant feature used by the ground truth function, and augmentation makes such a non-invariant feature unusable. Perhaps surprisingly, data augmentation is always helpful in the under-parameterized regime, while in the over-parameterized regime it can be harmful even when data is fully symmetric.

Suppose $G \leq O(d)$ acts linearly on $\mathbb{R}^d$, and let $y_i = x_i^\top \beta + \varepsilon_i$ for i.i.d. $x_i \sim \mathcal{N}(0, \Sigma)$, $\varepsilon_i \sim \mathcal{N}(0, \sigma^2)$, and invariant[2] ground truth $\beta$ (i.e. $g\beta = \beta$ for all $g \in G$). Importantly, we do not assume $g\Sigma g^\top = \Sigma$ (so $p_x$ may not be invariant). Given data $\{(x_i, y_i)\}_{i=1}^n$ and $\lambda > 0$, we consider the ridge regression problem, $\hat{\beta}_\lambda = \arg\min_\beta \frac{1}{n}\|y - X^\top \beta\|^2 + \lambda\|\beta\|^2 = (\hat{\Sigma} + \lambda I)^{-1}\hat{\Sigma}_{yx}$ where $\hat{\Sigma} = X^\top X/n$ and $\hat{\Sigma}_{yx} = X^\top y/n$ for $X \in \mathbb{R}^{n \times d}$ the matrix of samples and $y \in \mathbb{R}^n$ the label vector.

There are several natural approaches to enforcing invariance. Under the standard inner product, $\mathbb{R}^d$ decomposes into two orthogonal subspaces $V_0$ and $V_\perp$, where $V_0$ is the $d_0$-dimensional set of vectors invariant to $G$. In the first approach, Elesedy & Zaidi (2021) consider *test-time symmetrization*, $\mathbb{E}_g[g\hat{\beta}] = P_0\hat{\beta}$, where $P_0$ is the orthogonal projection onto $V_0$. The second approach is to use only the *invariant features* in the data, $\hat{\beta}_{\lambda,\text{inv}} = \arg\min_\beta \frac{1}{n}\|y - (XP_0)^\top\beta\|^2 + \lambda\|\beta\|^2 = (\hat{\Sigma}_{\text{inv}} + \lambda I)^{-1}\hat{\Sigma}_{yx,\text{inv}}$ where $\hat{\Sigma}_{\text{inv}} = (XP_0)^\top XP_0/n = P_0\hat{\Sigma}P_0$ and $\hat{\Sigma}_{yx,\text{inv}} = (XP_0)^\top y/n = P_0\hat{\Sigma}_{yx}$. In the linear setting, this turns out to be the **same** as ridge regression when (1) restricting $\beta$ to be invariant, or (2) under *infinite data augmentation*, i.e. the model sees $(gx_i, y)$ $\forall g \in G$ (Appendix A.2).

For any estimator $\hat{\beta}$, we are interested in its generalization error (or risk) on unseen data. Conditioned on the input data $X$, it takes the form $R_X(\hat{\beta}) = \mathbb{E}_{x,\varepsilon}[(x^\top\beta - x^\top\hat{\beta})^2|X] = \mathbb{E}_\varepsilon[\|\beta - \hat{\beta}\|_\Sigma^2|X]$, where $\|\beta\|_\Sigma^2 = \beta^\top\Sigma\beta$. Elesedy & Zaidi (2021) prove that when $p_x$ is invariant, one can always do better by symmetrizing at test time: $\mathbb{E}_X[R_X(P_0\hat{\beta})] \leq \mathbb{E}_X[R_X(\hat{\beta})]$ (even for non-linear predictors). We study two settings when $p_x$ is not invariant.

- **Under-parametrized ridgeless regime:** When $d < n - 1$ and $\lambda \to 0$, correlations between invariant and non-invariant features can drive $\mathbb{E}_X[R_X(P_0\hat{\beta})]$, the risk of test-time symmetrization, to infinity. But surprisingly, data augmentation is helpful regardless of any asymmetry in $p_x$.

In this regime, our intuition — that correlation between invariant features and non-invariant features (expressed through large $\Sigma^{-1}\Sigma_{\text{inv}}$) harms equivariant methods — bears out for test-time symmetrization, but not data augmentation. We thus pass to the over-parameterized setting, which captures some of the behavior of real-world neural networks (D'Ascoli et al., 2020; Atanasov et al., 2023; Jacot et al., 2018).

- **Over-parametrized regime:** When $d > n$, we use a minimal model to show data augmentation can be harmful when there are strong correlations, particularly when they lie in a space of dimension significantly smaller than $d$.

[2] While such a $\beta$ must be 0 if $G = O(d)$, the same is not true for $G \leq O(d)$, e.g. $G$ a subgroup of the permutation group that acts on only a subspace of $\mathbb{R}^d$.

### 4.1 The under-parameterized ridgeless regime

Using straightforward expressions for the bias-variance decomposition (see Lemma 1, Appendix), we show that data augmentation always improves generalization when $d < n-1$ and $\lambda \to 0$.

**Theorem 1.** *In the under-parameterized ridgeless setting, assuming $\Sigma$ is full-rank, $\mathbb{E}[R_X(\hat{\beta})] = \frac{\sigma^2 d}{n-d-1} \geq \mathbb{E}[R_X(\hat{\beta}_{\text{inv}})] = \frac{\sigma^2 d_0}{n-d_0-1}$, so augmentation helps. In contrast, for test-time symmetrization we have $\mathbb{E}[R_X(P_0\hat{\beta})] = \frac{\sigma^2}{n-d-1}\operatorname{Tr}(\Sigma^{-1}\Sigma_{\text{inv}}) \geq \frac{\sigma^2 d_0}{n-d-1}$, with equality when $p_x$ is invariant.*

While Elesedy & Zaidi (2021, Theorem 7) prove a non-negative gap for test-time symmetrization when $p_x$ is invariant, we see its risk can be much larger than that of regular (unconstrained) linear regression, when $\Sigma^{-1}$ does not "align" with $\Sigma_{\text{inv}}$. (This is illustrated in an example in Appendix A.5.)

### 4.2 The over-parameterized regime

We next consider $d > n$, taking the regime $n, d \to \infty$ and $d/n \to \gamma > 1$ to get deterministic estimates of the risk (assuming $\Sigma$ has bounded spectrum). It is known that as $\gamma \to 1$, the test risk of the usual ridgeless estimator $\hat{\beta}$ blows up. (Hastie et al., 2022). Similarly, one may easily show that *data augmentation can lead to a blow-up in risk even when $p_x$ is perfectly symmetric*. Namely, at the interpolation threshold $d_0/n \to \gamma_0 = 1$, effective dimension (consisting of invariant features) equals sample size.

**Fact 1.** *For identity covariance $\Sigma = I$, in the $\lambda \to 0$ limit we have asymptotic risk $R(\hat{\beta}_{\text{inv}}) = (1-\gamma_0^{-1}) + \sigma^2(\gamma_0^{-1}/(1-\gamma_0^{-1}))$, which explodes as $\gamma_0 \to 1$.*

To try to isolate the effect of the interpolation threshold from that of symmetry-breaking, we suppose $\gamma_0 > 1$, i.e. there are many possible invariant features to choose from. For tractability, we consider a minimal model for the covariance. Letting $d_c < \min(d_0, d-d_0)$ be the number of strong "coupling modes," let $\Sigma = (\sigma_c - \sigma_w)\sum_{k=1}^{d_c} u_k u_k^\top + \sigma_w I$, where $\sigma_c > \sigma_w$ are the coupling and weak (or "white") eigenvalues, and $u_k = (v_{0,k} + v_{\perp,k})/\sqrt{2}$ are perfect superpositions of orthogonal basis elements of $V_0$ and $V_\perp$. We consider $\sigma_w \to 0$ as the limit of strong correlations. Using random matrix theory (Atanasov et al., 2024b; Bach, 2024b), we characterize the asymptotic risk for data augmentation (Appendix A.6).[3] We find that data augmentation is *guaranteed* to perform worse when # correlational modes $\ll$ ambient dimension (Figure 3), while in other settings the story is more complex.

**Theorem 2.** *Let $d_c/n \to \gamma_c$ and consider the ridgeless limit $\lambda \to 0$, and $n, d \to \infty$. In the limit of strong correlations: (i) if $\gamma_c < 1$, both methods are unbiased and data augmentation has larger variance; (ii) For $\gamma_c > 1$, both methods have bias $C(\beta)\|\beta\|^2(\gamma_c - 1)/2\gamma_c$ where $C(\beta)$ (eq.* (53)*) is an explicit constant measuring how much of $\beta$ lies in the coupling subspace, and if moreover $\gamma_0 - \gamma_c/2 < 1/2$, then data augmentation has larger variance for small $\sigma_w > 0$.*

## 5 Experiments

Our theoretical analysis suggests that equivariant methods can be detrimental under distributional symmetry breaking; we now investigate this phenomenon on widely-used datasets. Our experiments serve multiple goals. First, we validate $m(p_X)$ by synthetically augmenting *subsets* of MNIST, verifying that $m(p_X)$ has the correct behavior. Second, we compute our metric, $m(p_X)$, to investigate the degree of distributional symmetry breaking in several benchmark datasets, and detect high levels of distributional symmetry breaking. We then compare equivariant and non-equivariant methods on the datasets' associated regression tasks, testing the applicability of our theory. We expect that, due to the distribution shift induced by augmentation on highly canonicalized datasets, training augmentation will hurt performance. Surprisingly, however, this is not the case for QM7b and QM9. These counterintuitive results motivate further investigation of task-dependent and local distributional symmetry breaking. Most of these results are contained in Table 1, and additional experimental details and results can be found in Appendix D. We now discuss each dataset in turn.

[3] This involves a version of the "two-point" deterministic equivalence studied by Atanasov et al. (2024a), of which we provide a different proof.

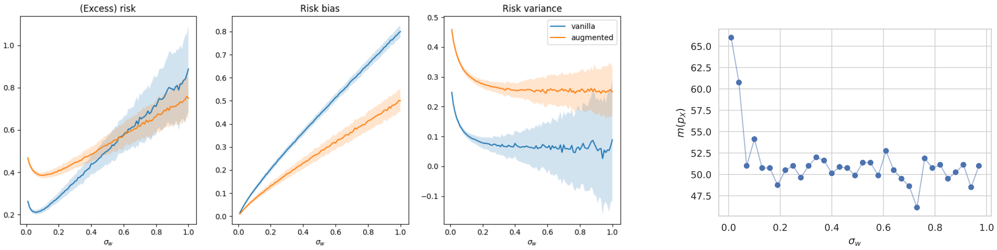

Figure 3: **Left:** Results in our minimal model for the over-parameterized regime, with mean and standard deviation across 200 trials. Small $\sigma_w$ corresponds to strong correlations between invariant and non-invariant features, and large $\sigma_w$ to no distributional symmetry breaking. In agreement with our theory, data augmentation is harmful in the former setting. See Appendix A.7.2 for details on the group and hyperparameters. **Right:** Corresponding values of $m(p_X)$ at varying $\sigma_w$, accurately reflecting the change in distributional symmetry-breaking.

Table 1: Comparison of train/test augmentation, group-averaged, and equivariant models across datasets. Augmentation: TT = train+test, TF = train only, FT = test only, FF = none. MNIST uses a $C_4$ group-averaged model; other datasets use stochastic group-averaging. MAE is reported for QM7b/QM9; equivariant baselines from `e3nn` Geiger et al. (2022). Best overall in bold, best within augmentation underlined. CNN used for MNIST, graph transformer for point clouds (Shi et al., 2022; Ying et al., 2021). See Figure 11 for results relative to FF.

| Setting / Dataset<br>Units | QM7b $\vec{\mu}$<br>a.u. (↓) | QM7b $\alpha_{\text{iso}}$<br>$a_0^3$ (↓) | QM9 $C_v$<br>cal/mol K (↓) | QM9 $\lvert\vec{\mu}\rvert$<br>D (↓) | QM9 $\Delta\varepsilon$<br>eV (↓) | MNIST (%)<br>% (↑) | ModelNet40<br>% (↑) |
|---|---|---|---|---|---|---|---|
| Equivariant | **0.043** | 0.662 | **0.119** | **0.139** | **0.153** | 97.8 | 60.08 |
| Group Averaged | 0.044 | **0.500** | 0.128 | 0.216 | 0.170 | 97.8 | 60.12 |
| TT | 0.055 | 0.523 | 0.157 | 0.263 | 0.183 | 96.35 | 61.89 |
| FF | 0.104 | 0.695 | 0.158 | 0.291 | 0.195 | **98.89** | **78.65** |
| TF | 0.054 | 0.522 | 0.154 | 0.262 | 0.183 | 96.56 | 62.75 |
| FT | 0.16 | 1.185 | 0.207 | 0.412 | 0.260 | 40.41 | 16.48 |
| Classifier Metric (%) | 89.93 | | 97.6 | | | 87.50 | 92.45 |

We start with **MNIST** (Deng, 2012), where digits should intuitively be mostly canonicalized with respect to 90° rotations ($C_4$). $m(p_X)$ verifies this, showing that transformed and untransformed samples can be distinguished with nearly optimal ($1 - \frac{1}{2*4} = 87.5\%$) accuracy (matching the calculation from Section 2). We further sanity check $m(p_X)$ by rotating $p$-fractions of the dataset (Figure 14), where it achieves nearly optimal accuracy at intermediate levels of canonicalization, too. This is a relatively easy task, so there is not a large difference between augmentation settings, yet the no augmentation (FF) setting does perform slightly better, see Appendix D.2. This behavior is also seen in ModelNet40.

Moving from 2D images to 3D shape classification, **ModelNet40** (Wu et al., 2015) provides a more complex benchmark dataset for shape recognition consisting of 12,311 CAD models across 40 common object categories. The version most commonly used in recent works is a pre-aligned variant (Sedaghat et al., 2016), as confirmed by high $m(p_X)$. We also apply the metric per class (Figure 4), indicating that certain classes are more canonicalized than others. Consistent with our intuition, the FF setting outperforms other augmentation strategies, demonstrating that here augmenting destroys useful information and makes the learning task harder.

Shifting to molecular property prediction, **QM9** consists of 133k small stable organic molecules with $\leq 9$ heavy atoms, together with scalar quantum mechanical properties (Ramakrishnan et al., 2014; Wu et al., 2017). $m(p_X)$ shows that QM9 is highly canonicalized with respect to rotations (see also Figure 2). The molecular conformers were generated using the commercial software CORINA Wu et al. (2017), which contains options to align SMILES strings by default (Sadowski et al., 1994; Schwab, 2010; Molecular Networks Altamira), an example of user-defined canonicalization (as in Figure 1) where we do not have direct accces to the canonicalization function. Analyzing the decision boundary of $m(p_X)$ allows for fine-grained analysis of this unknown canonicalization, and can be used to probe the canonicalization for discontinuities (see Appendix D.4). We find that the degree to which equivariance is beneficial varies per property (also seen in e.g. Liao & Smidt (2022); see Appendix D.4 for additional properties), *yet for nearly all properties, training augmentation/equivariance still helps performance!* We next consider a molecular dataset that has non-scalar labels to further study this behavior.

**QM7b** is a 7,211 molecule subset of GDB-13 (a database of stable and synthetically accessible organic molecules) composed of molecules with $\leq 7$ heavy atoms (Blum & Reymond, 2009; Montavon et al., 2013). We use a version of the dataset (Yang et al., 2019) containing non-scalar material response properties to explore how distributional symmetry breaking affects higher order geometric quantities. $m(p_X)$ shows this dataset has a high degree of distributional symmetry breaking, which we believe follows from pre-processing steps reported in Yang et al. (2019), such as using a kernel-based similarity metric to arrange atoms. We find that equivariance and augmentation are particularly beneficial for predicting the vector dipole moment ($\vec{\mu}$), more so than for scalar properties in the dataset (see Figure 11); nevertheless, augmentation again improves performance for both types of properties. Thus, we see a discrepancy between MNIST/ModelNet40 and QM9/QM7b, in agreement with the theory that equivariance can be helpful or harmful depending on the dataset.

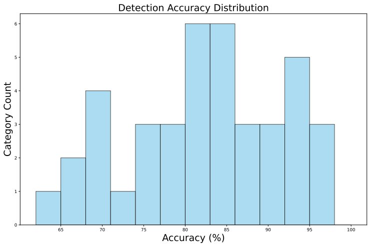

Figure 4: ModelNet40 $m(p_X)$ histogram over classes.

## 5.1 Additional Large-Scale Materials Datasets

We quantify distributional symmetry breaking in additional materials science datasets (including an LLM dataset) to demonstrate the utility of $m(p_X)$.

We explore two larger scale materials benchmarking datasets for predicting molecular energies and forces (**rMD17**, containing 100k structures from molecular dynamics simulations, and **OC20**, consisting of adsorbates placed on periodic crystalline catalysts (Christensen & von Lilienfeld, 2020; Chanussot* et al., 2021)). Interestingly, the degree of distributional symmetry breaking varies widely between molecules in MD17 (Figure 5; see Figure 37 for all molecules). We hypothesize that this is both due to the initial conditions for the simulation, and the differing physical structures of each molecule. For OC20, both the adsorbate and the adsorbate + catalyst are highly canonicalized, likely due to the catalyst's alignment with the $xy$ plane.

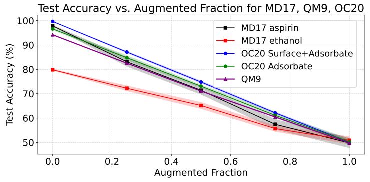

Figure 5: Test accuracy vs rotated fraction for aspirin and ethanol from rMD17, OC20 surface+adsorbate, OC20 adsorbate, and QM9.

Finally, we explore an **LLM materials dataset**, as there is growing interest in training large language models (LLMs) on diverse datatypes, including molecular data. To this end, Gruver et al. (2024) convert crystals into a text format, which requires listing their atoms in some ordering, and then train an LLM to generate new crystal structures. The authors independently noted that permutation augmentations hurt generative performance (their Appendix A.1), even though the task is ostensibly permutation invariant. We postulated that this phenomenon was due to distributional symmetry-breaking, i.e. conventions in the generation of atom order. We thus trained a classifier head on a pretrained DistilBERT transformer to distinguish between permuted and unpermuted datapoints, and found $m(p_X) = 95\%$ accuracy. (Indeed, their Figure 2 reveals clear ordering in the atoms; but with thousands of datapoints, a systematic test is useful for quantitative verification.)

In summary, our experiments show that many benchmark point cloud datasets are secretly quite aligned (or, nearly canonicalized[4]). We emphasize that $m(p_X)$ is an easy-to-train metric that ML

[4] Although high $m(p_X)$ does not precisely mean the datasets are perfectly canonicalized, particularly for infinite groups like $SO(3)$, it does mean that datapoints have clear, sparse preferred orientations.

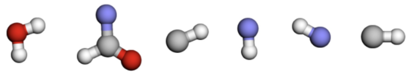

| $m(p_X)$ | Local QM9 | Global QM9 |
|---|---|---|
| Original | 67.6% | 98.5% |
| Rotated | 49.9% | 49.5% |
| Canonicalized | 99.8% | 99.8% |

| N | $m(p_X)$ (5 runs) |
|---|---|
| 10 | 55.6% ± 8.44 |
| 50 | 72.7% ± 4.51 |
| 100 | 81.5% ± 4.79 |
| 200 | 88.8% ± 0.62 |
| 500 | 93.6% ± 0.39 |
| 700 | 96.5% ± 0.12 |
| 1024 (global) | 96.6% ± 0.04 |

Figure 6: Left: The local QM9 dataset (top) and results (bottom). Right: Local ModelNet40 results.

practicioners can use to determine the degree of distributional symmetry breaking present when this may not be known a priori. Additionally, even though all datasets have high degrees of distributional asymmetry, the relative performance of data augmentation varies by dataset. In particular, train-time augmentation on ModelNet40 and MNIST hurt test-time performance on the unaugmented test set ("TF") relative to training without augmentations ("FF"), which makes sense from a distribution shift perspective. Yet, train-time augmentation on QM9 helps even on the unaugmented test set! In the following sections, we offer potential hypotheses behind this phenomenon.

### 5.2 Task-Dependent Metric

The value $m(p_X)$ determines whether there is discernible lack of uniformity over group transformations in the unlabeled dataset. However, it does not capture whether that distributional symmetry breaking (e.g. preferred orientations) is correlated with the specific task labels, such as in the case of MNIST 6s/9s. If it does, then we hypothesize that augmenting is a poor choice, as it discards task-relevant information contained in orientations. However, if the distributional symmetry breaking has no relation to the task of interest, then it is more subtle whether full-group data augmentation will hurt performance, as shown in Section 5.

Towards this goal, we briefly introduce a metric of *task-useful* distributional symmetry breaking (see Appendix C for full details). Let $c\colon \mathscr{X} \to G$ be a canonicalization function, denoting where on each orbit $x$ is. Since data augmentation destroys any information contained in $c(x)$, we wish to understand the dependence between orientations $c(x)$ and labels $f(x)$. A natural way to do this is to predict $f(x)$ directly from $c(x)$, where $c(x)$ is a randomly initialized, untrained equivariant neural network.[5] We then compare the test criterion $\mathscr{L}(c(x) \to f(x))$ to that obtained when the inputs are randomly transformed by elements of the given group, $\mathscr{L}_{\text{rot}} = \mathscr{L}(c(gx) \to f(gx)), g \sim G$ which removes any task-relevant information in the orientations (where $\mathscr{L}$ is the performance on the test set, e.g. accuracy/MAE).

**Results (Table 2):** We first explore an artificial **QM7b dipole** canonicalization. This is a constructed example of a very task-relevant canonicalization, where molecules are aligned such that their dipole moments are along the $z$ axis. This makes it easy for a non-equivariant model to predict dipoles, while an equivariant model cannot exploit this alignment. This is confirmed empirically in Table 10, where with the dipole canonicalization, the FF augmentation setting outperforms an equivariant model. The task-dependent metric indeed yields a large signal when applied to the dipole-canonicalized dataset. **ModelNet** is another case where equivariance harms performance, and the task-dependent metric shows a large signal. In contrast, for the **QM9** properties shown, the metric shows a small signal. Thus, our preliminary experiments show that the task-dependent metric is generally larger for tasks where equivariance does *not* improve performance. In the future, we aim to more rigorously determine whether there exists a threshold above which equivariance is unlikely to provide benefits.

### 5.3 Locality Experiments

One hypothesis for the effectiveness of equivariant methods is that the features are equivariant functions of their receptive fields, meaning equivariant CNNs and GNNs naturally have local equivari-

[5] This is closely related to the concepts of V-information (Xu & Raginsky, 2017) and the information bottleneck (via the canonicalization) (Tishby et al., 1999).

Table 2: Task-dependent metric: Accuracy (ModelNet) or MAE (QM7b/QM9) of predicting $f(x)$ from $c(x)$ versus a baseline with random rotations. The relative signal shows how $\mathscr{L}$ changes under rotation: $\mathscr{L}$rot$/\mathscr{L}$ for error metrics (lower better) and $\mathscr{L}/\mathscr{L}$rot for accuracy (higher better). Values are averaged over five seeds.

| Dataset | $\mathscr{L}$ | $\mathscr{L}_{\text{rot}}$ | Relative Improvement $\mathscr{L}$ Compared to $\mathscr{L}_{\text{rot}}$ |
|---|---|---|---|
| QM7b Dipole $\mu$ (↓) | 0.12 | 0.45 | **3.75** |
| QM7b Orig $\mu$ (↓) | 0.43 | 0.45 | 1.04 |
| ModelNet (↑) | 12 | 2 | **6** |
| QM9 $C_v$ (↓) | 3.02 | 3.19 | 1.05 |
| QM9 $\lvert\vec{\mu}\rvert$ (↓) | 1.12 | 1.16 | 1.04 |
| QM9 $G$ (↓) | 30.5 | 30.83 | 1.01 |

ance (Musaelian et al., 2023). The idea is that it may be useful to compute locally equivariant features, e.g. featurizations of small, recurrent chemical motifs in molecules, rather than just globally equivariant features (Du et al., 2022; Lippmann et al., 2025). This provides a plausible explanation for the effectiveness of equivariant methods on highly canonicalized datasets such as QM9. Moreover, augmenting inputs to a local (e.g. message-passing) architecture implicitly conveys a bias towards local equivariance. While it is challenging to establish a causal link, we can at least use $m(p_X)$ to quantify the hypothesis that local motifs are comparatively more isotropic in orientation.

Concretely, we generate the local QM9 dataset by extracting local neighborhoods (by bonds) from each molecule in QM9. In Figure 6, we compare $m(p_X)$ between local and ordinary QM9 in three settings: the original datasets (exploration), and under random rotation and manual canonicalization (as sanity checks, which should yield 50% and 100%, respectively). We find that the detection accuracy is much lower for local QM9, indicating a lower degree of local distributional symmetry breaking! For ModelNet40, we analogously constructed a local dataset by randomly selecting one point from each original, 1024-point point cloud, and then collecting its $N$ nearest neighbors. When the number of sampled points is small, the metric drops significantly, indicating that local regions of the point clouds are not inherently canonicalized; this effect reduces with the size of the neighborhood. Overall, these findings suggest that the distributional symmetry-breaking present in several point cloud benchmark datasets is far weaker at the local scale, and may partially explain the success of rotationally equivariant methods on canonicalized datasets.

## 6 Conclusion

In this work, we aimed to provide both empirical and theoretical analysis of distributional asymmetry and its implications for learning. Our interpretable metrics quantify the degree of symmetry-breaking present in a dataset without using any specific knowledge of the domain, thus providing practioners with a simple diagnostic for detecting distributional symmetry breaking in their datasets. Experiments revealed a high degree of symmetry-breaking in every benchmark dataset, yet augmentation only impeded (test) performance for ModelNet40 and MNIST.

Overall, these findings have intriguing implications for equivariant learning. First, they affirm that if evaluated only on in-distribution validation data, non-equivariant models may appear accurate, yet fail to generalize under transformations. Assessing whether this is problematic requires domain expertise: see Figure 10 for a flowchart on how to use our metrics for practitioners. Moreover, *applying* canonicalization to data has been proposed as a flexible method for making black-box models globally equivariant (Kaba et al., 2023). However, if molecular datasets both are already canonicalized and still experience benefits from augmentation and equivariance, this suggests that they provide some *additional*, possibly *domain-specific* benefit beyond global equivariance that is currently unexplained. Finally, data augmentation is often considered universally beneficial for invariant tasks, yet we show that it can sometimes hurt performance on the test set.

**Future Work** Predicting when and why different data augmentations can benefit learning, even in the case of nearly canonicalized data, is a useful future direction. For example, one could examine whether distributional asymmetry beneficially reduces function space complexity, e.g. covering number.

**Reproducibility Statement** We describe experimental and model details in Appendix D. We also include our code with our submission and plan to make the code public.

## REFERENCES

Brandon Anderson, Truong-Son Hy, and Risi Kondor. Cormorant: Covariant molecular neural networks. In *Advances in neural information processing systems (NeurIPS)*, 2019.

Alexander Atanasov, Blake Bordelon, Sabarish Sainathan, and Cengiz Pehlevan. The onset of variance-limited behavior for networks in the lazy and rich regimes. In *The Eleventh International Conference on Learning Representations*, 2023. URL https://openreview.net/forum?id=JLINxPOVTh7.

Alexander Atanasov, Jacob A. Zavatone-Veth, and Cengiz Pehlevan. Risk and cross validation in ridge regression with correlated samples, 2024a. URL https://arxiv.org/abs/2408.04607.

Alexander Atanasov, Jacob A. Zavatone-Veth, and Cengiz Pehlevan. Scaling and renormalization in high-dimensional regression, 2024b. URL https://arxiv.org/abs/2405.00592.

F. Bach. *Learning Theory from First Principles*. Adaptive Computation and Machine Learning series. MIT Press, 2024a. ISBN 9780262381369. URL https://books.google.co.uk/books?id=R_T8EAAAQBAJ.

Francis Bach. High-dimensional analysis of double descent for linear regression with random projections. *SIAM Journal on Mathematics of Data Science*, 6(1):26–50, 2024b. doi: 10.1137/23M1558781. URL https://doi.org/10.1137/23M1558781.

Albert P. Bartók, Risi Kondor, and Gábor Csányi. On representing chemical environments. *Phys. Rev. B*, 87:184115, May 2013. doi: 10.1103/PhysRevB.87.184115. URL https://link.aps.org/doi/10.1103/PhysRevB.87.184115.

Gregory Benton, Marc Finzi, Pavel Izmailov, and Andrew G Wilson. Learning invariances in neural networks from training data. In H. Larochelle, M. Ranzato, R. Hadsell, M.F. Balcan, and H. Lin (eds.), *Advances in Neural Information Processing Systems*, volume 33, pp. 17605–17616. Curran Associates, Inc., 2020a. URL https://proceedings.neurips.cc/paper_files/paper/2020/file/cc8090c4d2791cdd9cd2cb3c24296190-Paper.pdf.

Gregory Benton, Marc Finzi, Pavel Izmailov, and Andrew G. Wilson. Learning invariances in neural networks. In *Advances in Neural Information Processing Systems 33 (NeurIPS 2020)*, pp. 21732–21744, 2020b. URL https://arxiv.org/abs/2010.11882. arXiv preprint arXiv:2010.11882.

Alberto Bietti, Luca Venturi, and Joan Bruna. On the sample complexity of learning under geometric stability. In A. Beygelzimer, Y. Dauphin, P. Liang, and J. Wortman Vaughan (eds.), *Advances in Neural Information Processing Systems*, 2021. URL https://openreview.net/forum?id=vlf0zTKa5Lh.

L. C. Blum and J.-L. Reymond. 970 Million Druglike Small Molecules for Virtual Screening in the Chemical Universe Database GDB-13. *Journal of the American Chemical Society*, 131:8732–8733, 2009. doi: 10.1021/ja902302h.

A. Caponnetto and E. De Vito. Optimal rates for the regularized least-squares algorithm. *Foundations of Computational Mathematics*, 7(3):331–368, 2007. doi: 10.1007/s10208-006-0196-8. URL https://doi.org/10.1007/s10208-006-0196-8.

Lowik Chanussot*, Abhishek Das*, Siddharth Goyal*, Thibaut Lavril*, Muhammed Shuaibi*, Morgane Riviere, Kevin Tran, Javier Heras-Domingo, Caleb Ho, Weihua Hu, Aini Palizhati, Anuroop Sriram, Brandon Wood, Junwoong Yoon, Devi Parikh, C. Lawrence Zitnick, and Zachary Ulissi. Open catalyst 2020 (oc20) dataset and community challenges. *ACS Catalysis*, 2021. doi: 10.1021/acscatal.0c04525.

Hippolyte Charvin, Nicola Catenacci Volpi, and Daniel Polani. Towards information theory-based discovery of equivariances. In *NeurIPS 2023 Workshop on Symmetry and Geometry in Neural Representations*, 2023. URL https://openreview.net/forum?id=oD8DD5jQ5I.

Shuxiao Chen, Edgar Dobriban, and Jane H. Lee. A group-theoretic framework for data augmentation. *Journal of Machine Learning Research*, 21(245):1–71, 2020. URL http://jmlr.org/papers/v21/20-163.html.

Kenny Chiu and Benjamin Bloem-Reddy. Non-parametric hypothesis tests for distributional group symmetry. In *NeurIPS AI for Science Workshop*, 2023.

Stefan Chmiela, Alexandre Tkatchenko, Huziel E. Sauceda, Igor Poltavsky, Kristof T. Schütt, and Klaus-Robert Müller. Machine learning of accurate energy-conserving molecular force fields. 2017. doi: 10.1126/sciadv.1603015. URL https://www.science.org/doi/10.1126/sciadv.1603015. Publisher: American Association for the Advancement of Science.

Anders S Christensen and O Anatole von Lilienfeld. On the role of gradients for machine learning of molecular energies and forces. *Machine Learning: Science and Technology*, 1(4): 045018, oct 2020. doi: 10.1088/2632-2153/abba6f. URL https://dx.doi.org/10.1088/2632-2153/abba6f.

Deborah Cohen, Amit Daniely, Amir Globerson, and Gal Elidan. Learning rules-first classifiers. In *AISTATS*, Proceedings of Machine Learning Research. PMLR, 16–18 Apr 2019.

Taco S. Cohen and Max Welling. Steerable CNNs. *arXiv preprint arXiv:1612.08498*, 2016a.

Taco S. Cohen, Mario Geiger, Jonas Köhler, and Max Welling. Spherical CNNs. In *International Conference on Learning Representations*, 2018. URL https://openreview.net/forum?id=Hkbd5xZRb.

T.S. Cohen and M. Welling. Group equivariant convolutional networks. In *Proceedings of the International Conference on Machine Learning (ICML)*, 2016b.

Stéphane D'Ascoli, Maria Refinetti, Giulio Biroli, and Florent Krzakala. Double trouble in double descent: Bias and variance(s) in the lazy regime. In Hal Daumé III and Aarti Singh (eds.), *Proceedings of the 37th International Conference on Machine Learning*, volume 119 of *Proceedings of Machine Learning Research*, pp. 2280–2290. PMLR, 13–18 Jul 2020. URL https://proceedings.mlr.press/v119/d-ascoli20a.html.

Congyue Deng, Or Litany, Yueqi Duan, Adrien Poulenard, Andrea Tagliasacchi, and Leonidas J Guibas. Vector neurons: A general framework for so (3)-equivariant networks. In *Proceedings of the IEEE/CVF International Conference on Computer Vision*, pp. 12200–12209, 2021.

Li Deng. The mnist database of handwritten digit images for machine learning research. *IEEE Signal Processing Magazine*, 29(6):141–142, 2012.

Krish Desai, Benjamin Nachman, and Jesse Thaler. Symmetry discovery with deep learning. *Physical Review D*, 105(9):096031, 2022.

Edgar Dobriban and Yueqi Sheng. Distributed linear regression by averaging. *The Annals of Statistics*, 2018. URL https://api.semanticscholar.org/CorpusID:88517039.

Weitao Du, He Zhang, Yuanqi Du, Qi Meng, Wei Chen, Nanning Zheng, Bin Shao, and Tie-Yan Liu. SE(3) equivariant graph neural networks with complete local frames. In Kamalika Chaudhuri, Stefanie Jegelka, Le Song, Csaba Szepesvari, Gang Niu, and Sivan Sabato (eds.), *Proceedings of the 39th International Conference on Machine Learning*, volume 162 of *Proceedings of Machine Learning Research*, pp. 5583–5608. PMLR, 17–23 Jul 2022. URL https://proceedings.mlr.press/v162/du22e.html.

Nadav Dym, Hannah Lawrence, and Jonathan W Siegel. Equivariant frames and the impossibility of continuous canonicalization. In *Proceedings of the 41st International Conference on Machine Learning*, ICML'24. JMLR.org, 2024.

Bryn Elesedy and Sheheryar Zaidi. Provably strict generalisation benefit for equivariant models. In *International conference on machine learning*, pp. 2959–2969. PMLR, 2021.

Carlos Esteves, Yinshuang Xu, Christine Allen-Blanchette, and Kostas Daniilidis. Equivariant multi-view networks. In *Proceedings of the IEEE/CVF international conference on computer vision*, pp. 1568–1577, 2019.

Marc Anton Finzi, Gregory Benton, and Andrew Gordon Wilson. Residual pathway priors for soft equivariance constraints. In A. Beygelzimer, Y. Dauphin, P. Liang, and J. Wortman Vaughan (eds.), *Advances in Neural Information Processing Systems*, 2021. URL https://openreview.net/forum?id=k505ekjMzww.

Mario Geiger, Tess Smidt, Alby M., Benjamin Kurt Miller, Wouter Boomsma, Bradley Dice, Kostiantyn Lapchevskyi, Maurice Weiler, Michał Tyszkiewicz, Simon Batzner, Dylan Madisetti, Martin Uhrin, Jes Frellsen, Nuri Jung, Sophia Sanborn, Mingjian Wen, Josh Rackers, Marcel Rød, and Michael Bailey. Euclidean neural networks: e3nn, April 2022. URL https://doi.org/10.5281/zenodo.6459381.

Spyros Gidaris, Praveer Singh, and Nikos Komodakis. Unsupervised representation learning by predicting image rotations. In *International Conference on Learning Representations*, 2018. URL https://openreview.net/forum?id=S1v4N2l0-.

Nate Gruver, Anuroop Sriram, Andrea Madotto, Andrew Gordon Wilson, C. Lawrence Zitnick, and Zachary Ward Ulissi. Fine-tuned language models generate stable inorganic materials as text. In *The Twelfth International Conference on Learning Representations*, 2024. URL https://openreview.net/forum?id=vN9fpfqoP1.

Trevor Hastie, Andrea Montanari, Saharon Rosset, and Ryan J. Tibshirani. Surprises in high-dimensional ridgeless least squares interpolation. *The Annals of Statistics*, 50(2):949 – 986, 2022. doi: 10.1214/21-AOS2133. URL https://doi.org/10.1214/21-AOS2133.

Elyssa Hofgard, Rui Wang, Robin Walters, and Tess E. Smidt. Relaxed equivariant graph neural networks. *arXiv preprint arXiv:2407.20471*, 2024.

Kevin Han Huang, Peter Orbanz, and Morgane Austern. Gaussian and non-gaussian universality of data augmentation, 2025. URL https://arxiv.org/abs/2202.09134.

Ilia Igashov, Hannes Stärk, Clément Vignac, Arne Schneuing, Victor Garcia Satorras, Pascal Frossard, Max Welling, Michael Bronstein, and Bruno Correia. Equivariant 3d-conditional diffusion model for molecular linker design. *Nature Machine Intelligence*, pp. 1–11, 2024.

Arthur Jacot, Franck Gabriel, and Clement Hongler. Neural tangent kernel: Convergence and generalization in neural networks. In S. Bengio, H. Wallach, H. Larochelle, K. Grauman, N. Cesa-Bianchi, and R. Garnett (eds.), *Advances in Neural Information Processing Systems*, volume 31. Curran Associates, Inc., 2018. URL https://proceedings.neurips.cc/paper_files/paper/2018/file/5a4be1fa34e62bb8a6ec6b91d2462f5a-Paper.pdf.

Sékou-Oumar Kaba, Arnab Kumar Mondal, Yan Zhang, Yoshua Bengio, and Siamak Ravanbakhsh. Equivariance with learned canonicalization functions. In *International Conference on Machine Learning*, pp. 15546–15566. PMLR, 2023.

David M. Klee, Ondrej Biza, Robert Platt, and Robin Walters. Image to sphere: Learning equivariant features for efficient pose prediction, 2023. URL https://arxiv.org/abs/2302.13926.

Joseph Kleinhenz and Ameya Daigavane. e3tools. URL https://github.com/prescient-design/e3tools/tree/main.

Yi-Lun Liao and Tess Smidt. Equiformer: Equivariant graph attention transformer for 3d atomistic graphs. *arXiv preprint arXiv:2206.11990*, 2022.

Yi-Lun Liao, Brandon Wood, Abhishek Das, and Tess Smidt. Equiformerv2: Improved equivariant transformer for scaling to higher-degree representations. *arXiv preprint arXiv:2306.12059*, 2023.

Chi-Heng Lin, Chiraag Kaushik, Eva L. Dyer, and Vidya Muthukumar. The good, the bad and the ugly sides of data augmentation: An implicit spectral regularization perspective. *Journal of Machine Learning Research*, 25(91):1–85, 2024. URL http://jmlr.org/papers/v25/22-1312.html.

Peter Lippmann, Gerrit Gerhartz, Roman Remme, and Fred A. Hamprecht. Beyond canonicalization: How tensorial messages improve equivariant message passing. In *Proceedings of the International Conference on Learning Representations (ICLR)*, 2025. URL https://openreview.net/forum?id=vDp6StrKIq. Poster, arXiv preprint arXiv:2405.15389v3.

David Lopez-Paz and Maxime Oquab. Revisiting classifier two-sample tests. In *International Conference on Learning Representations*, 2017. URL https://openreview.net/forum?id=SJkXfE5xx.

Daniel McNeela. Almost equivariance via lie algebra convolutions. *arXiv preprint arXiv:2310.13164*, 2023.

Song Mei, Theodor Misiakiewicz, and Andrea Montanari. Learning with invariances in random features and kernel models. In Mikhail Belkin and Samory Kpotufe (eds.), *Proceedings of Thirty Fourth Conference on Learning Theory*, volume 134 of *Proceedings of Machine Learning Research*, pp. 3351–3418. PMLR, 15–19 Aug 2021. URL https://proceedings.mlr.press/v134/mei21a.html.

Ning Miao, Tom Rainforth, Emile Mathieu, Yann Dubois, Yee Whye Teh, Adam Foster, and Hyunjik Kim. Learning instance-specific augmentations by capturing local invariances. In Andreas Krause, Emma Brunskill, Kyunghyun Cho, Barbara Engelhardt, Sivan Sabato, and Jonathan Scarlett (eds.), *Proceedings of the 40th International Conference on Machine Learning*, volume 202 of *Proceedings of Machine Learning Research*, pp. 24720–24736. PMLR, 23–29 Jul 2023. URL https://proceedings.mlr.press/v202/miao23a.html.

Molecular Networks Altamira. 3D Structure Generator CORINA Classic. http://www.mn-am.com. MN-AM, Nuremberg, Germany.

Grégoire Montavon, Matthias Rupp, Vivekanand Gobre, Alvaro Vazquez-Mayagoitia, Katja Hansen, Alexandre Tkatchenko, Klaus-Robert Müller, and O Anatole von Lilienfeld. Machine learning of molecular electronic properties in chemical compound space. *New Journal of Physics*, 15(9):095003, 2013. URL http://stacks.iop.org/1367-2630/15/i=9/a=095003.

Kieran Murphy, Carlos Esteves, Varun Jampani, Srikumar Ramalingam, and Ameesh Makadia. Implicit-pdf: Non-parametric representation of probability distributions on the rotation manifold, 2022. URL https://arxiv.org/abs/2106.05965.

A. Musaelian, S. Batzner, A. Johansson, L. Sun, C. J. Owen, M. Kornbluth, and B. Kozinsky. Learning local equivariant representations for large-scale atomistic dynamics. *Nature Communications*, 14(1):579, February 2023. ISSN 2041-1723. doi: 10.1038/s41467-023-36329-y.

Long Nguyen, Xuan J. Wainwright, Martin and I. Jordan, Michael˙ On surrogate loss functions and $f$-divergences. *The Annals of Statistics*, 37(2):876–904, 2009. doi: 10.1214/08-AOS595. URL https://projecteuclid.org/journals/annals-of-statistics/volume-37/issue-2/On-surrogate-loss-functions-and-f-divergences/10.1214/08-AOS595.full.

Pratik Patil. *Facets of regularization in high-dimensional learning: Cross-validation, risk monotonization, and model complexity*. PhD thesis, Carnegie Mellon University, 12 2022. URL https://kilthub.cmu.edu/articles/thesis/Facets_of_regularization_in_high-dimensional_learning_Cross-validation_risk_monotonization_and_model_complexity/21692822.

Raghunathan Ramakrishnan, Pavlo O Dral, Matthias Rupp, and O Anatole von Lilienfeld. Quantum chemistry structures and properties of 134 kilo molecules. *Scientific Data*, 1, 2014.

Francisco Rubio and Xavier Mestre. Spectral convergence for a general class of random matrices. *Statistics & Probability Letters*, 81(5):592–602, 2011. ISSN 0167-7152. doi: https://doi.org/10.1016/j.spl.2011.01.004. URL `https://www.sciencedirect.com/science/article/pii/S0167715211000113`.

J. Sadowski, J. Gasteiger, and G. Klebe. Comparison of automatic three-dimensional model builders using 639 x-ray structures. *Journal of Chemical Information and Computer Sciences*, 34:1000–1008, 1994. doi: 10.1021/ci00020a039.

C. H. Schwab. Conformations and 3d pharmacophore searching. *Drug Discovery Today: Technologies*, 7(4):e245–e253, 2010. doi: 10.1016/j.ddtec.2010.10.003. Winter 2010.

Nima Sedaghat, Mohammadreza Zolfaghari, Ehsan Amiri, and Thomas Brox. Orientation-boosted voxel nets for 3d object recognition. *arXiv preprint arXiv:1604.03351*, 2016.

Han Shao, Omar Montasser, and Avrim Blum. A theory of pac learnability under transformation invariances. In *Proceedings of the 36th International Conference on Neural Information Processing Systems*, NIPS '22, Red Hook, NY, USA, 2024. Curran Associates Inc. ISBN 9781713871088.

Yue Sheng and Edgar Dobriban. One-shot distributed ridge regression in high dimensions. In Hal Daumé III and Aarti Singh (eds.), *Proceedings of the 37th International Conference on Machine Learning*, volume 119 of *Proceedings of Machine Learning Research*, pp. 8763–8772. PMLR, 13–18 Jul 2020. URL `https://proceedings.mlr.press/v119/sheng20a.html`.

Yu Shi, Shuxin Zheng, Guolin Ke, Yifei Shen, Jiacheng You, Jiyan He, Shengjie Luo, Chang Liu, Di He, and Tie-Yan Liu. Benchmarking graphormer on large-scale molecular modeling datasets. *arXiv preprint arXiv:2203.04810*, 2022. URL `https://arxiv.org/abs/2203.04810`.

Tess E Smidt, Mario Geiger, and Benjamin Kurt Miller. Finding symmetry breaking order parameters with euclidean neural networks. *Physical Review Research*, 3(1):L012002, 2021.

Ashkan Soleymani, Behrooz Tahmasebi, Stefanie Jegelka, and Patrick Jaillet. A robust kernel statistical test of invariance: Detecting subtle asymmetries. In Yingzhen Li, Stephan Mandt, Shipra Agrawal, and Emtiyaz Khan (eds.), *Proceedings of The 28th International Conference on Artificial Intelligence and Statistics*, volume 258 of *Proceedings of Machine Learning Research*, pp. 4816–4824. PMLR, 03–05 May 2025. URL `https://proceedings.mlr.press/v258/soleymani25a.html`.

Bharath K. Sriperumbudur, Kenji Fukumizu, Arthur Gretton, Bernhard Schölkopf, and Gert R. G. Lanckriet. On integral probability metrics, $\phi$-divergences and binary classification. *arXiv preprint arXiv:0901.2698*, 2009. URL `https://arxiv.org/abs/0901.2698`.

Nathaniel Thomas, Tess Smidt, Steven Kearnes, Lusann Yang, Li Li, Kai Kohlhoff, and Patrick Riley. Tensor field networks: Rotation-and translation-equivariant neural networks for 3d point clouds. *arXiv preprint arXiv:1802.08219*, 2018.

Naftali Tishby, Fernando C. Pereira, and William Bialek. The information bottleneck method. In *Proc. of the 37-th Annual Allerton Conference on Communication, Control and Computing*, pp. 368–377, 1999. URL `https://arxiv.org/abs/physics/0004057`.

Alonso Urbano and David W. Romero. Self-supervised detection of perfect and partial input-dependent symmetries. *arXiv preprint arXiv:2312.12223*, 2024a.

Alonso Urbano and David W. Romero. Self-supervised detection of perfect and partial input-dependent symmetries. In Sharvaree Vadgama, Erik Bekkers, Alison Pouplin, Sekou-Oumar Kaba, Robin Walters, Hannah Lawrence, Tegan Emerson, Henry Kvinge, Jakub Tomczak, and Stephanie Jegelka (eds.), *Proceedings of the Geometry-grounded Representation Learning and Generative Modeling Workshop (GRaM)*, volume 251 of *Proceedings of Machine Learning Research*, pp. 113–131. PMLR, 29 Jul 2024b. URL `https://proceedings.mlr.press/v251/urbano24a.html`.

Dian Wang, Jung Yeon Park, Neel Sortur, Lawson LS Wong, Robin Walters, and Robert Platt. The surprising effectiveness of equivariant models in domains with latent symmetry. In *The Eleventh International Conference on Learning Representations*, 2023.

Dian Wang, Stephen Hart, David Surovik, Tarik Kelestemur, Haojie Huang, Haibo Zhao, Mark Yeatman, Jiuguang Wang, Robin Walters, and Robert Platt. Equivariant diffusion policy. *arXiv preprint arXiv:2407.01812*, 2024a.

Dian Wang, Xupeng Zhu, Jung Yeon Park, Mingxi Jia, Guanang Su, Robert Platt, and Robin Walters. A general theory of correct, incorrect, and extrinsic equivariance. *Advances in Neural Information Processing Systems*, 36, 2024b.

Dian Wang, Xupeng Zhu, Jung Yeon Park, Mingxi Jia, Guanang Su, Robert Platt, and Robin Walters. A general theory of correct, incorrect, and extrinsic equivariance. In *Proceedings of the 37th International Conference on Neural Information Processing Systems*, NIPS '23, Red Hook, NY, USA, 2024c. Curran Associates Inc.

Rui Wang, Robin Walters, and Rose Yu. Incorporating symmetry into deep dynamics models for improved generalization. In *International Conference on Learning Representations*, 2021.

Rui Wang, Elyssa Hofgard, Robin Walters, and Tess Smidt. Discovering symmetry breaking in physical systems with relaxed group convolution. *arXiv preprint arXiv:2310.02299*, 2024d.

Zhenqin Wu, Bharath Ramsundar, Evan N. Feinberg, Joseph Gomes, Caleb Geniesse, Aneesh S. Pappu, Karl Leswing, and Vijay Pande. MoleculeNet: a benchmark for molecular machine learning. *Chemical Science*, 9(2):513, October 2017. doi: 10.1039/c7sc02664a. URL https://pmc.ncbi.nlm.nih.gov/articles/PMC5868307/.

Zhirong Wu, Shuran Song, Aditya Khosla, Fisher Yu, Linguang Zhang, Xiaoou Tang, and Jianxiong Xiao. 3d shapenets: A deep representation for volumetric shapes. In *Proceedings of the IEEE conference on computer vision and pattern recognition*, pp. 1912–1920, 2015.

Aolin Xu and Maxim Raginsky. Information-theoretic analysis of generalization capability of learning algorithms. In I. Guyon, U. Von Luxburg, S. Bengio, H. Wallach, R. Fergus, S. Vishwanathan, and R. Garnett (eds.), *Advances in Neural Information Processing Systems*, volume 30. Curran Associates, Inc., 2017. URL https://proceedings.neurips.cc/paper_files/paper/2017/file/ad71c82b22f4f65b9398f76d8be4c615-Paper.pdf.

Jianke Yang, Robin Walters, Nima Dehmamy, and Rose Yu. Generative adversarial symmetry discovery. *arXiv preprint arXiv:2302.00236*, 2023.

Yuezhi Yang, Ka Un Lao, David M Wilkins, Robert A DiStasio Jr, and Alexandre Tkatchenko. Quantum mechanical static dipole polarizabilities in the qm7b and alphaml showcase databases. *Scientific Data*, 6(1):152, 2019. doi: 10.1038/s41597-019-0157-8.

Chengxuan Ying, Tianle Cai, Shengjie Luo, Shuxin Zheng, Guolin Ke, Di He, Yanming Shen, and Tie-Yan Liu. Do transformers really perform badly for graph representation? In *Thirty-Fifth Conference on Neural Information Processing Systems*, 2021. URL https://openreview.net/forum?id=OeWooOxFwDa.

Jacob A. Zavatone-Veth. Harvard APMTH 226: Lecture notes on the inductive biases of high-dimensional ridge regression, 2024. URL https://jzv.io/assets/pdf/am226_generalization_in_ridge_regression_lecture_notes.pdf.

# APPENDICES

# A THEORY

In this section, we elaborate on the theory of the main paper, including both more context and proofs of results. The earlier parts are dedicated to our study of ridge regression in Section 4.

- Appendix A.1: we review the result of Elesedy & Zaidi (2021), which says that when data is invariant in distribution, test symmetrization always improves generalization error. (Unlike our analysis, this holds even in the non-linear setting.)
- Appendix A.2: we show that using invariant features, or equivalently, restricting to invariant estimators — which we call *training symmetrization* — is equivalent to data augmentation in the ridge regression setting.
- Appendix A.3: we record the bias-variance decompositions of risk for vanilla ridge regressions, test-time symmetrization, and data augmentation.
- Appendix A.4: we prove Theorem 1, which generalizes Elesedy & Zaidi (2021, Theorem 7) to non-invariant data, and to data augmentation.
- Appendix A.5: we demonstrate in an explicit example that test-time symmetrization can arbitrarily increase risk when the data distribution is not invariant (in the under-parameterized regime).
- Appendix A.6: using random matrix theory, we derive asymptotic expressions (“deterministic equivalents”) for the bias and variance of each of our three estimators in the over-parameterized regime. **??** 1 is a direct corollary.
- Appendix A.7: we analytically study our minimal model of covariance, proving Theorem 2. We confirm our results empirically, as shown in Figure 3.

### A.1 Review of the generalization gap of Elesedy & Zaidi (2021)

Consider data $(x,y) \in \mathbb{R}^d \times \mathbb{R}$ generated as $y = f^*(x) + \varepsilon$ for $x \sim p_x$, a ground-truth invariant function $f^*$, and independent mean-zero finite-variance noise $\varepsilon$. Considering $L^2$ loss, the excess risk of a given function $f$ (say the result of learning on some fixed training dataset) is

$$R(f) = \mathbb{E}[(y - f(x))^2] - \mathbb{E}[(y - f^*(x))^2] = \mathbb{E}[(f(x) - f^*(x))^2] \tag{1}$$

since $\mathbb{E}[\varepsilon(f(x) - f^*(x)] = 0$. We define a new inner product on functions, $\langle f_1, f_2 \rangle_{p_x} = \mathbb{E}[f_1(x) f_2(x)]$. The excess risk of $f$ is then $\|f - f^*\|_{p_x}^2$, with the norm induced by this inner product.

Let $\bar{f}(x) = \mathbb{E}_g[f(gx)]$ be the symmetrization of $f$ with respect to uniformly random $g \in G$. We can think of this as test-time augmentation. We can ask what the difference is between the excess risk of $f$ and $\bar{f}$,

$$\Delta(f, \bar{f}) := \|f - f^*\|_{p_x}^2 - \|\bar{f} - f^*\|_{p_x}^2 = -2 \left\langle f^* - \bar{f}, f - \bar{f} \right\rangle_{p_x} + \|f - \bar{f}\|_{p_x}^2. \tag{2}$$

Elesedy and Zaidi show that when $x$ is invariant in distribution, $f - \bar{f}$ is orthogonal (in the inner product defined above) to invariant functions, and thus in particular to $f^* - \bar{f}$. In this case $\Delta(f, \bar{f}) \geq 0$, meaning for any $f$ one can always achieve better generalization using $\bar{f}$. When $p_x$ is not invariant, however, the inner product might make the overall expression negative. This case thus warrants further investigation.

### A.2 Equivalence of training symmetrization and data augmentation

We consider the estimator obtained by infinitely many augmentations,

$$\hat{\beta}_{\lambda,\text{aug}} = \arg\min_{\beta} \frac{1}{n} \sum_{i=1}^{n} \mathbb{E}_g[(y_i - (gx_i)^\top \beta)^2] + \lambda \|\beta\|^2 = (\hat{\Sigma}_{\text{aug}} + \lambda I)^{-1} \hat{\Sigma}_{yx,\text{inv}} \tag{3}$$

where $\hat{\Sigma}_{\text{aug}} = \mathbb{E}_g[g \hat{\Sigma} g^\top]$. As a linear map $\mathbb{R}^d \to \mathbb{R}^d$, $\hat{\Sigma}_{\text{aug}}$ is equivariant, so by Schur's lemma it is block-diagonal in $V_0, V_\perp$ (or more generally, in irreps). Since $\hat{\Sigma}_{yx,\text{inv}}$ is non-zero only in the $V_0$ component, $(\hat{\Sigma}_{\text{aug}} + \lambda I)^{-1} \hat{\Sigma}_{yx,\text{inv}} = (\hat{\Sigma}_{\text{inv}} + \lambda I)^{-1} \hat{\Sigma}_{yx,\text{inv}}$, and thus $\hat{\beta}_{\lambda,\text{aug}} = \hat{\beta}_{\lambda,\text{inv}}$. We therefore refer to $\hat{\beta}_{\lambda,\text{inv}}$ interchangeably as using data augmentation or invariant features.

### A.3 Bias-variance decompositions

The risk of any estimator $\hat{\beta}$ has a bias-variance decomposition $R_X(\hat{\beta}) = B_X(\hat{\beta}) + V_X(\hat{\beta})$ with

$$B_X(\hat{\beta}) = \left\| \mathbb{E}\left[\hat{\beta} \mid X\right] - \beta \right\|_\Sigma^2 \qquad V_X(\hat{\beta}) = \operatorname{Tr}(\operatorname{Cov}(\hat{\beta} \mid X)\Sigma) \tag{4}$$

In the case of vanilla ridge(less) regression, the expressions above have well-known and easily derived forms (Bach, 2024a; Hastie et al., 2022). We list the equivalent expressions for test-time symmetrization and data augmentation below. The proof is standard, being a simple expansion of definitions. One may notice that the expressions are the same as the vanilla case except (1) test-time symmetrization replaces $\Sigma$ with $\Sigma_{\text{inv}} = P_0 \Sigma P_0$, and (2) data augmentation replaces $\hat{\Sigma}$ with $\hat{\Sigma}_{\text{inv}}$.

**Lemma 1.** *For unaugmented ridge(less) regression, the bias and variance terms are standard:*

$$B_X(\hat{\beta}_\lambda) = \lambda^2 \beta^\top (\hat{\Sigma} + \lambda I)^{-1} \Sigma (\hat{\Sigma} + \lambda I)^{-1} \beta \qquad V_X(\hat{\beta}_\lambda) = \frac{\sigma^2}{n} \operatorname{Tr}(\hat{\Sigma}(\hat{\Sigma} + \lambda I)^{-2} \Sigma) \tag{5}$$

$$B_X(\hat{\beta}) = \beta^\top \Pi \Sigma \Pi \beta \qquad V_X(\hat{\beta}) = \frac{\sigma^2}{n} \operatorname{Tr}(\hat{\Sigma}^+ \Sigma) \tag{6}$$

*where $\Pi = I - \hat{\Sigma}^+ \hat{\Sigma}$ projects onto the null space of $X$. Test-time symmetrization gives*

$$B_X(P_0 \hat{\beta}_\lambda) = \lambda^2 \beta^\top (\hat{\Sigma} + \lambda I)^{-1} \Sigma_{\text{inv}} (\hat{\Sigma} + \lambda I)^{-1} \beta \qquad V_X(P_0 \hat{\beta}_\lambda) = \frac{\sigma^2}{n} \operatorname{Tr}(\hat{\Sigma}(\hat{\Sigma} + \lambda I)^{-2} \Sigma_{\text{inv}}) \tag{7}$$

$$B_X(P_0 \hat{\beta}) = \beta^\top \Pi \Sigma_{\text{inv}} \Pi \beta \qquad V_X(P_0 \hat{\beta}) = \frac{\sigma^2}{n} \operatorname{Tr}(\hat{\Sigma}^+ \Sigma_{\text{inv}}), \tag{8}$$

*whereas for invariant features and data augmentation, we obtain*

$$B_X(\hat{\beta}_{\lambda,\text{inv}}) = \lambda^2 \beta^\top (\hat{\Sigma}_{\text{inv}} + \lambda I)^{-1} \Sigma (\hat{\Sigma}_{\text{inv}} + \lambda I)^{-1} \beta \qquad V_X(\hat{\beta}_{\lambda,\text{inv}}) = \frac{\sigma^2}{n} \operatorname{Tr}(\hat{\Sigma}_{\text{inv}} (\hat{\Sigma}_{\text{inv}} + \lambda I)^{-2} \Sigma) \tag{9}$$

$$B_X(\hat{\beta}_{\text{inv}}) = \beta^\top \Pi_{\text{inv}} \Sigma \Pi_{\text{inv}} \beta \qquad V_X(\hat{\beta}_{\text{inv}}) = \frac{\sigma^2}{n} \operatorname{Tr}((\hat{\Sigma}_{\text{inv}})^+ \Sigma), \tag{10}$$

*where $\Pi_{\text{inv}} = P_0 - (\hat{\Sigma}_{\text{inv}})^+ \hat{\Sigma}_{\text{inv}}$. In latter case, we note that every instance of $\Sigma$ can equivalently be replaced with $\Sigma_{\text{inv}}$, being multiplied "on both sides" by invariant objects.*

### A.4 Proof of Theorem 1

When $d < n-1$, the matrices $\Pi$ and $\Pi_{\text{inv}}$ defined in Lemma 1 are almost surely equal to the zero matrix. Thus the vanilla, test-time symmetrization, and data augmentation estimators are all unbiased, and we compare only their variances.

Having assumed $x_i \sim \mathcal{N}(0, \Sigma)$, the empirical covariance is a scaling of Wishart-distributed matrix: $n\hat{\Sigma} \sim \mathscr{W}(\Sigma, n)$. Since $\Sigma$ is full rank, the standard form for the expectation of the inverse Wishart $\frac{1}{n}\hat{\Sigma}^{-1} \sim \mathscr{W}^{-1}(\Sigma^{-1}, n)$ gives

$$\mathbb{E}[\hat{\Sigma}^{-1}] = \frac{n\Sigma^{-1}}{n-d-1} \qquad \Rightarrow \qquad \mathbb{E}[V_X(\hat{\beta})] = \frac{\sigma^2 \operatorname{Tr}(\Sigma^{-1}\Sigma)}{n-d-1} = \frac{\sigma^2 d}{n-d-1}. \tag{11}$$

For test-time symmetrization, note that the trace term in the variance only depends on $V_0$ components of the inverse empirical covariance: $\operatorname{Tr}(\hat{\Sigma}^{-1}\Sigma_{\text{inv}}) = \operatorname{Tr}(P_0 \hat{\Sigma}^{-1} P_0 \Sigma_{\text{inv}})$. We thus use the fact that diagonal sub-matrices of inverse-Wishart matrices are inverse-Wishart of a certain form. Letting $V$ be the change of basis matrix into $V_0, V_\perp$, so that any matrix $M$ can be written as

$$V^\top M V = \begin{pmatrix} M_{00} & M_{0\perp} \\ M_{\perp 0} & M_{\perp\perp} \end{pmatrix}, \tag{12}$$

we have $nV^\top \hat{\Sigma} V \sim \mathscr{W}(V^\top \Sigma V, n)$ and $\frac{1}{n}(\hat{\Sigma}^{-1})_{00} \sim \mathscr{W}^{-1}((\Sigma^{-1})_{00}, n - d_\perp)$ where $d_\perp = \dim V_\perp$. We thus have

$$\mathbb{E}[V_X(P_0\hat{\beta})] = \frac{\sigma^2 \operatorname{Tr}((\Sigma^{-1})_{00}\Sigma_{00})}{(n-d_\perp) - d_0 - 1} = \frac{\sigma^2 \operatorname{Tr}(\Sigma^{-1}\Sigma_{\text{inv}})}{n-d-1}. \tag{13}$$

For invariant features, the relevant trace term is $\operatorname{Tr}((\hat{\Sigma}_{\text{inv}})^+ \Sigma_{\text{inv}}) = \operatorname{Tr}((\hat{\Sigma}_{00})^{-1}\Sigma_{00})$. The result follows the same logic as in the vanilla case: $n\hat{\Sigma}_{00} \sim \mathscr{W}(\Sigma_{00}, n)$, and thus

$$\mathbb{E}[(\hat{\Sigma}_{00})^{-1}] = \frac{n(\Sigma_{00})^{-1}}{n-d_0-1} \qquad \Rightarrow \qquad \mathbb{E}[V_X(\hat{\beta}_{\text{inv}})] = \frac{\sigma^2 \operatorname{Tr}((\Sigma_{00})^{-1}(\Sigma_{00}))}{n-d_0-1} = \frac{\sigma^2 d_0}{n-d_0-1}. \tag{14}$$

### A.5 Permutation example

Consider the case of $G = S_3$ acting on three-dimensional inputs $x \in \mathbb{R}^3$ by permuting coordinates. Let $V$ be the change of basis matrix into the $G$-invariant subspaces $V_0, V_\perp$, and write $M_{00}$ for the $(V_0, V_0)$-block of $V^\top M V$. We then consider a covariance

$$V^\top \Sigma V = \begin{pmatrix} \sigma_{\text{inv}}^2 & \rho & \rho \\ \rho & 1 & \tau \\ \rho & \tau & 1 \end{pmatrix} \qquad \Rightarrow \qquad (\Sigma^{-1})_{00} = \frac{1}{\sigma_{\text{inv}}^2 - \frac{2\rho^2}{1+\tau}} \tag{15}$$

such that $\operatorname{Tr}(\Sigma^{-1}\Sigma_{\text{inv}}) = \left(1 - \frac{2\rho^2}{\sigma_{\text{inv}}^2(1+\tau)}\right)^{-1}$. This term is large when $|\rho|$, the correlation strength between invariant and non-invariant features, is large compared to the invariant signal $\sigma_{\text{inv}}^2$. In particular, we have $\mathbb{E}[R_X(\hat{\beta})] < \mathbb{E}[R_X(P_0\hat{\beta})] \to \infty$ as $2\rho^2$ grows from $\frac{2}{3}\sigma_{\text{inv}}^2(1+\tau)$ to $\sigma_{\text{inv}}^2(1+\tau)$.

While we do not do so here, this example can be extended to general $G$ and $\Sigma$ by using the Schur complement formula for $(\Sigma^{-1})_{00}$, in which case the "size" of $\Sigma_{0\perp}$ in the Loewner order plays the role of the correlation $\rho$.

### A.6 Deterministic equivalents for bias and variance

In the proportional asymptotic regime, where $n, d \to \infty$ and $d/n \to \gamma$, we leverage the notion of *deterministic equivalence* of possibly random matrices $A_n$ and $B_n$. In particular, we write $A_n \simeq B_n$ when for any matrices $C_n$ of bounded trace norm,

$$|\operatorname{Tr}((A_n - B_n)C_n)| \to 0. \tag{16}$$

In our derivations below, we take advantage of the "calculus of deterministic equivalents" as developed by Dobriban & Sheng (2018); Sheng & Dobriban (2020), as well as proof techniques of Hastie et al. (2022), which in turn rely on the generalized Marchenko-Pastur theorem of Rubio & Mestre (2011). We also utilize the notions of first- and second-order degrees of freedom, $\mathrm{df}^1$ and $\mathrm{df}^2$, used by Atanasov et al. (2024b); Bach (2024b),[6] and introduced by Caponnetto & De Vito (2007) as "effective dimension."

Our goal is to find deterministic equivalents for the matrix products appearing in the bias and variance expressions in Lemma 1 (for $\lambda > 0$), which all take the two forms

$$B_{\mu\nu} = \lambda^2 \beta^\top (\hat{\Sigma}_\mu + \lambda I)^{-1} \Sigma_\nu (\hat{\Sigma}_\mu + \lambda I)^{-1} \beta \qquad V_{\mu\nu} = \frac{\sigma^2}{n} \operatorname{Tr}((\hat{\Sigma}_\mu + \lambda I)^{-2} \hat{\Sigma}_\mu \Sigma_\nu) \tag{17}$$

where $\mu, \nu$ run over empty or inv subscripts. Here, we assume the setting of the generalized Marchenko-Pastur theorem — namely, that we have the deterministic equivalence

$$\lambda (\hat{\Sigma}_\mu + \lambda I)^{-1} \simeq \kappa_\mu (\Sigma_\mu + \kappa_\mu I)^{-1} \tag{18}$$

where $\kappa_\mu$ is the unique positive solution to

$$\kappa_\mu = \frac{\lambda}{1 - T_\mu(\kappa_\mu)} \qquad T_\mu(\kappa) = \frac{1}{n} \mathrm{df}^1_\mu(\kappa) = \frac{1}{n} \operatorname{Tr}((\Sigma_\mu + \kappa I)^{-1} \Sigma_\mu) \tag{19}$$

and can be seen as the effective or renormalized ridge parameter; this includes the setting of i.i.d. Gaussian data, but extends much further, to the *Gaussian universality* regime (Hastie et al., 2022; Zavatone-Veth, 2024). We prove the deterministic equivalences

$$B_{\mu\nu} \simeq \frac{\kappa_\mu^2 \alpha_{\mu\nu}}{1 - \alpha_{\mu\mu}} \beta^\top (\Sigma_\mu + \kappa_\mu I)^{-2} \Sigma_\mu \beta + \kappa_\mu^2 \beta^\top (\Sigma_\mu + \kappa_\mu I)^{-1} \Sigma_\nu (\Sigma_\mu + \kappa_\mu I)^{-1} \beta \tag{20}$$

$$V_{\mu\nu} \simeq \sigma^2 \frac{\alpha_{\mu\nu}}{1 - \alpha_{\mu\mu}} \tag{21}$$

where we define generalized second-order degrees of freedom,

$$\alpha_{\mu\nu} = \frac{1}{n} \mathrm{df}^2_{\mu\nu}(\kappa_\mu) \qquad \mathrm{df}^2_{\mu\nu}(\kappa) = \operatorname{Tr}((\Sigma_\mu + \kappa)^{-2} \Sigma_\mu \Sigma_\nu). \tag{22}$$

We do not claim our calculation of these deterministic equivalents is novel; indeed our presentation closely follows the notes of Zavatone-Veth (2024), and the "two-point" equivalences we consider were recently analyzed in the context of cross validation by Patil (2022) and Atanasov et al. (2024a). To our knowledge, however, our work is the first to apply these techniques to study invariant learning.

#### A.6.1 Bias term

Note that

$$\lambda^2 (\hat{\Sigma}_\mu + \lambda I + \lambda \tau \Sigma_\nu)^{-1} \Sigma_\nu (\hat{\Sigma}_\mu + \lambda I + \lambda \tau \Sigma_\nu)^{-1} \Big|_{\tau=0} \tag{23}$$

$$= -\partial_\tau \lambda (\hat{\Sigma}_\mu + \lambda I + \lambda \tau \Sigma_\nu)^{-1} \Big|_{\tau=0} \tag{24}$$

We find a deterministic equivalent for the expression inside the derivative. First, note

$$\lambda (\hat{\Sigma}_\mu + \lambda I + \lambda \tau \Sigma_\nu)^{-1} = \lambda (I + \tau \Sigma_\nu)^{-1/2} (\hat{\Sigma}_\tau + \lambda I)^{-1} (I + \tau \Sigma_\nu)^{-1/2} \tag{25}$$

[6] Note that the notion used by Atanasov et al. (2024b) is scaled by $1/d$ with respect to that of Bach (2024b); we use the latter convention.

where we define

$$\hat{\Sigma}_\tau = (I+\tau\Sigma_\nu)^{-1/2}\hat{\Sigma}_\mu(I+\tau\Sigma_\nu)^{-1/2}, \tag{26}$$

That is, our expression is a product of deterministic matrices with the matrix ridge resolvent for a scaled version of the empirical covariance. This resolvent thus has the deterministic equivalent

$$\lambda(\hat{\Sigma}_\tau+\lambda I)^{-1} \simeq \kappa_\tau(\Sigma_\tau+\kappa_\tau I)^{-1} \tag{27}$$

where $\Sigma_\tau$ is the population covariance $\Sigma_\mu$ scaled in the same way as $\hat{\Sigma}_\tau$ is, and $\kappa_\tau$ is the unique positive solution to

$$\kappa_\tau = \frac{\lambda}{1-T_\tau(\kappa_\tau)}. \tag{28}$$

We thus have

$$\lambda(\hat{\Sigma}_\mu+\lambda I+\lambda\tau\Sigma_\nu)^{-1} \simeq \kappa_\tau(\Sigma_\mu+\tau I+\kappa_\tau\tau\Sigma_\nu)^{-1}. \tag{29}$$

Under the assumption that $\Sigma_\mu$ is trace class, one can exchange the $n,d\to\infty$ limit and the derivative to obtain

$$\lambda^2(\hat{\Sigma}_\mu+\lambda I)^{-1}\Sigma_\nu(\hat{\Sigma}_\mu+\lambda I)^{-1} \simeq -\partial_\tau\kappa_\tau(\Sigma_\mu+\kappa_\tau I+\kappa_\tau\tau\Sigma_\nu)^{-1}\Big|_{\tau=0} \tag{30}$$

Let us write $\delta = \partial_\tau\kappa_\tau|_{\tau=0}$, and note that $\kappa_\tau|_{\tau=0} = \kappa_\mu$. We get, first using the matrix identity $\partial M^{-1} = -M^{-1}(\partial M)M^{-1}$, and then combining terms,

$$-\delta(\Sigma_\mu+\kappa_\mu I)^{-1} + \kappa_\mu(\Sigma_\mu+\kappa_\mu I)^{-1}(\delta I+\kappa_\mu\Sigma_\nu)(\Sigma_\mu+\kappa_\mu I)^{-1} \tag{31}$$

$$= -\delta\Sigma_\mu(\Sigma_\mu+\kappa_\mu I)^{-2} + \kappa_\mu^2(\Sigma_\mu+\kappa_\mu I)^{-1}\Sigma_\nu(\Sigma_\mu+\kappa_\mu I)^{-1}. \tag{32}$$

It remains to evaluate $\delta$, which we do by differentiating the fixed-point equation at $\tau=0$,

$$\kappa_\tau - \kappa_\tau T_\tau = \lambda \qquad \rightarrow \qquad \delta - \delta T_\tau\Big|_{\tau=0} - \kappa_\mu\partial_\tau(T_\tau)\Big|_{\tau=0} = 0. \tag{33}$$

Recognizing $1-T_\tau|_{\tau=0}$ as $\lambda/\kappa_\mu$ (from the fixed-point equation at $\tau=0$), we get

$$\delta = \frac{\kappa_\mu^2}{\lambda}\partial_\tau(T_\tau)\Big|_{\tau=0} = -\frac{\kappa_\mu^2}{\lambda n}\delta\,\mathrm{Tr}((\Sigma_\mu+\kappa_\mu I)^{-2}\Sigma_\mu) - \frac{\kappa_\mu^3}{\lambda}\alpha_{\mu\nu} \tag{34}$$

Since $(\Sigma_\mu+\kappa_\mu I)^{-1} = (I+(\Sigma_\mu+\kappa_\mu I)^{-1}\Sigma_\mu)/\kappa$,

$$\frac{1}{n}\mathrm{Tr}((\Sigma_\mu+\kappa_\mu)^{-2}\Sigma_\mu) = \frac{1}{\kappa_\mu}(T_\tau|_{\tau=0}-\alpha_{\mu\mu}) = \frac{1}{\kappa_\mu}\left(1-\frac{\lambda}{\kappa_\mu}-\alpha_{\mu\mu}\right). \tag{35}$$

Subsequently,

$$\delta = -\frac{\kappa_\mu\delta}{\lambda}\left(1-\frac{\lambda}{\kappa_\mu}-\alpha_{\mu\mu}\right) - \frac{\kappa_\mu^3}{\lambda}\alpha_{\mu\nu} = -\left(\frac{\kappa_\mu}{\lambda}(1-\alpha_{\mu\mu})-1\right)\delta - \frac{\kappa_\mu^3}{\lambda}\alpha_{\mu\nu}. \tag{36}$$

We can then solve,

$$\delta = -\frac{\lambda}{\kappa_\mu(1-\alpha_{\mu\mu})}\frac{\kappa_\mu^3}{\lambda}\alpha_{\mu\nu} = -\kappa_\mu^2\frac{\alpha_{\mu\nu}}{1-\alpha_{\mu\mu}}. \tag{37}$$

### A.6.2 Variance term

We begin by noting that

$$\frac{\sigma^2}{n}\mathrm{Tr}((\hat{\Sigma}_\mu+\lambda I)^{-2}\hat{\Sigma}_\mu\Sigma_\nu) = -\frac{\sigma^2}{n}\partial_\lambda\,\mathrm{Tr}((\hat{\Sigma}_\mu+\lambda I)^{-1}\hat{\Sigma}_\mu\Sigma_\nu) = \frac{\sigma^2}{n}\partial_\lambda\lambda\,\mathrm{Tr}((\hat{\Sigma}_\mu+\lambda I)^{-1}\Sigma_\nu). \tag{38}$$

By assumption $\lambda(\hat{\Sigma}_\mu+\lambda I)^{-1} \simeq \kappa_\mu(\Sigma_\mu+\kappa_\mu I)^{-1}$. Exchanging limits and the derivative (which is justified by the assumption of bounded trace norm) we get the deterministic equivalent

$$\frac{1}{n}\partial_\lambda\kappa_\mu\,\mathrm{Tr}((\Sigma_\mu+\kappa_\mu I)^{-1}\Sigma_\nu) = \frac{1}{n}\partial_\lambda(\kappa_\mu)\,\mathrm{Tr}((\Sigma_\mu+\kappa_\mu I)^{-2}\Sigma_\mu\Sigma_\nu) = \partial_\lambda(\kappa_\mu)\alpha_{\mu\nu}. \tag{39}$$

To find the derivative, we differentiate the fixed-point equation

$$\kappa_\mu - \kappa_\mu T_\mu = \lambda \qquad \rightarrow \qquad \partial_\lambda(\kappa_\mu) - \partial_\lambda(\kappa_\mu T_\mu) = \partial_\lambda(\kappa_\mu)(1-\alpha_{\mu\mu}) = 1, \tag{40}$$

where in the first equality on the right we used the chain rule and $\partial_{\kappa_\mu}(\kappa_\mu T_\mu) = \alpha_{\mu\mu}$. Thus, $\partial_\lambda(\kappa_\mu) = 1/(1-\alpha_{\mu\mu})$, which plugged into the expression above proves the result.

### A.7 Analysis of the minimal model for covariance

Recall that our minimal model is

$$\Sigma = \sigma_c \sum_{k=1}^{d_c} u_k u_k^\top + \sigma_w \sum_{k=d_c+1}^{d} u_k u_k^\top \tag{41}$$

where the first $d_c$ eigenvectors $u_k = (v_{0,k} + v_{\perp,k})/\sqrt{2}$ represent coupling modes, and the remaining $u_k$ complete the orthonormal basis. Note that when the coupling and weak directions have the same strength ($\sigma_c = \sigma_w$), we reduce to the isotropic case. We thus are interested what changes as $\sigma_c/\sigma_w$ grows, which we study by taking the $\sigma_w \to 0$ limit.

The fixed-point equation for $\kappa$ is

$$\kappa \left(1 - \gamma_c \frac{\sigma_c}{\sigma_c + \kappa} + (\gamma - \gamma_c) \frac{\sigma_w}{\sigma_w + \kappa}\right) = \lambda. \tag{42}$$

This has the same solutions as a cubic in $\kappa$. One option is to directly study the large $\sigma_c$ limit, in which case the equation becomes independent of $\sigma_c$. We instead take the over-parameterized ridgeless limit ($\lambda \to 0$ and $\gamma > 1$), where $\kappa$ solves

$$1 = \gamma_c \frac{\sigma_c}{\sigma_c + \kappa} + (\gamma - \gamma_c) \frac{\sigma_w}{\sigma_w + \kappa}. \tag{43}$$

Comparison to training symmetrization must be delicate. The effective ridge parameter solves

$$\kappa_{\text{inv}} \left(1 - \gamma_c \frac{\bar{\sigma}}{\bar{\sigma} + \kappa_{\text{inv}}} + (\gamma_0 - \gamma_c) \frac{\sigma_w}{\sigma_w + \kappa_{\text{inv}}}\right) = \lambda \tag{44}$$

where $\bar{\sigma} = (\sigma_c + \sigma_w)/2$. We again take $\lambda \to 0$. When $\gamma_0 < 1$ we obtain an effective ridge of $\kappa_{\text{inv}} = 0$. This is intuitive: if $d_0 < n$ we are back in the ordinary least squares regime once we project the data down into $V_0$. If $d_0 = O(1)$ (i.e. the number of invariant features in the problem is finite) then we are in the $\gamma_0 \to 0$ regime of Theorem 1, where training symmetrization helps. However, as in the isotropic example, if $\gamma > 1$ but $0 < \gamma_0 < 1$ then $R(\hat{\beta}_{\text{inv}})$ can still grow arbitrarily large as we approach the new interpolation threshold. (This also means the order one takes the $\gamma_0 \to 0$ and $\gamma \to \infty$ limits matters; taking the latter first, for example fixing $d_0$ and $n$ and taking $d \to \infty$, still shows harmful effects for training symmetrization.)

#### A.7.1 Proof of Theorem 2

We consider the case $\gamma_0 > 1$ and $\lambda \to 0$, in which

$$1 = \gamma_c \frac{\bar{\sigma}}{\bar{\sigma} + \kappa_{\text{inv}}} + (\gamma_0 - \gamma_c) \frac{\sigma_w}{\sigma_w + \kappa_{\text{inv}}}. \tag{45}$$

This has the same form as the equation for $\kappa$. Indeed, we can write $\kappa = \kappa(\sigma_c, \sigma_w, \gamma)$ and $\kappa_{\text{inv}} = \kappa(\bar{\sigma}, \sigma_w, \gamma_0)$ where $\kappa(s, w, g)$ solves the quadratic system

$$\kappa(s,w,g)^2 + b(s,w,g)\kappa(s,w,g) + c(s,w,g) = 0 \tag{46}$$

$$b(s,w,g) = (s+w) - \gamma_c s + (g - \gamma_c)w \tag{47}$$

$$c(s,w,g) = (1-g)sw \tag{48}$$

For $g > \gamma_c$, one can observe $\kappa(s,w,g)$ is increasing in its arguments. Thus, $\kappa_{\text{inv}} \leq \kappa$ — training symmetrization has a smaller effective regularization. In the "strong correlation" limit $w \to 0$, we have $\kappa(s,0,g) = \max(0, s(\gamma_c - 1))$. That is, we have a new threshold, corresponding to when the model is over-parameterized with respect to the number of correlational modes.

Similarly, $\alpha = \alpha(\sigma_c, \sigma_w, \gamma)$ and $\alpha_{\text{inv,inv}} = \alpha(\bar{\sigma}, \sigma_w, \gamma_0)$ where

$$\alpha(s,w,g) = \gamma_c \left(\frac{s}{s + \kappa(s,w,g)}\right)^2 + (g - \gamma_c)\left(\frac{w}{w + \kappa(s,w,p)}\right)^2. \tag{49}$$

The second term and approaches $(1 + \kappa'(s,0,g))^{-1}$ as $w \to 0$ when $\gamma_c < 1$, where we use $'$ to denote differentiation with respect to $w$. Evaluating the derivative, in the regime of $\gamma_c < 1$ we have $\alpha(s,w,g) \to \gamma_c + \frac{(1-\gamma_c)^2}{g - \gamma_c}$, and thus $\alpha_{\text{inv,inv}} > \alpha$.

In the correlationally over-parameterized regime $\gamma_c > 1$, the second term vanishes as $w \to 0$, and we get $\alpha(s,w,p) \to \gamma_c^{-1}$ (using our result for $\kappa(s,0,g)$), which we note is independent of $s$ and $g$. So, in the limit of strong correlations, $\alpha = \alpha_{\text{inv,inv}}$. We thus examine the derivatives $\alpha'(s,0,p)$. Doing so, we again find that $\alpha_{\text{inv,inv}} > \alpha$ in a neighborhood of $w = 0$ when $\gamma_0 - (\gamma_c/2) < 1/2$, i.e. when a good portion of the invariant features are captured in correlational modes.

Since $x \mapsto x/(1-x)$ is monotonically increasing, the above behavior fully describes how $V_X(\hat{\beta})$ compares asymptotically to $V_X(\hat{\beta}_{\text{inv}})$.

Understanding the biases

$$B_X(\hat{\beta}) \simeq \frac{\kappa^2}{1-\alpha}\left(\frac{\sigma_c}{(\sigma_c+\kappa)^2}\sum_{k=1}^{d_c}(u_k^\top\beta)^2 + \frac{\sigma_w}{(\sigma_w+\kappa)^2}\sum_{k=d_c+1}^{d}(u_k^\top\beta)^2\right) \tag{50}$$

$$B_X(\hat{\beta}_{\text{inv}}) \simeq \frac{\kappa_{\text{inv}}^2}{1-\alpha_{\text{inv,inv}}}\left(\frac{\bar{\sigma}}{(\bar{\sigma}+\kappa_{\text{inv}})^2}\sum_{k=1}^{d_c}(v_k^\top\beta)^2 + \frac{\sigma_w}{(\sigma_w+\kappa_{\text{inv}})^2}\sum_{k=d_c+1}^{d_0}(v_k^\top\beta)^2\right) \tag{51}$$

requires handling the dependence on $\beta$. Since $\beta$ is assumed invariant, and thus $\|\beta\|^2 = \sum_{k=1}^{d_0}(v_k^\top\beta)^2$,

$$\sum_{k=d_c+1}^{d}(u_k^\top\beta)^2 = \|\beta\|^2 - \sum_{k=1}^{d_c}(u_k^\top\beta)^2 = \|\beta\|^2\left(1-\frac{C(\beta)}{2}\right), \tag{52}$$

where we define the coupling factor

$$C(\beta) = \sum_{k=1}^{d_c}(v_k^\top\beta)^2/\|\beta\|^2. \tag{53}$$

The expressions for biases become

$$B_X(\hat{\beta}) \simeq \frac{\kappa^2\|\beta\|^2}{1-\alpha}\left(\frac{\sigma_c}{(\sigma_c+\kappa)^2}\frac{C(\beta)}{2} + \frac{\sigma_w}{(\sigma_w+\kappa)^2}\left(1-\frac{C(\beta)}{2}\right)\right) \tag{54}$$

$$B_X(\hat{\beta}_{\text{inv}}) \simeq \frac{\kappa_{\text{inv}}^2\|\beta\|^2}{1-\alpha_{\text{inv,inv}}}\left(\frac{\bar{\sigma}}{(\bar{\sigma}+\kappa_{\text{inv}})^2}C(\beta) + \frac{\sigma_w}{(\sigma_w+\kappa_{\text{inv}})^2}(1-C(\beta))\right). \tag{55}$$

The $\gamma_c > 1$ regime is straightforward reusing our previous calculations, giving

$$B_X(\hat{\beta}) \simeq B_X(\hat{\beta}_{\text{inv}}) \simeq \frac{\sigma_c(\gamma_c-1)C(\beta)\|\beta\|^2}{2\gamma_c}, \tag{56}$$

at $\sigma_w = 0$, while for $\gamma_c < 1$ both go to zero with $\sigma_w \to 0$.

### A.7.2 Simulation details

We now describe the simulations used to obtain Figure 3. We first describe the hyperparameter settings, and then the group symmetry.

We fix values of $n = 100$, $d = 5n$, $d_0 = 2n$, and $d_c = \lfloor n/2 \rfloor$, which puts us in the over-parameterized regime, but where the model is "correlationally under-parameterized" ($\gamma_c < 1$). In this setting, our theory predicts that as $\sigma_w \to 0$, both methods become unbiased, but data augmentation has higher variance. This is indeed what we observe in simulations. To generate Figure 3, we set $\sigma_c = 1$, so that we examine $\sigma_w$ as a fraction of $\sigma_c$. The noise is generated as $\varepsilon_i \sim \mathcal{N}(0,\sigma^2)$ with $\sigma = 0.5$, and we set nominal regularization $\lambda = 10^{-8}$ to approximate the ridgeless setting.

In order to set $d_0$, we use the permutation group $G = S_{d-d_0+1}$ acting on the first $d-d_0+1$ coordinates of $\mathbb{R}^d$. The invariant space $V_0$ then consists of a one-dimensional subspace of $\mathbb{R}^{d-d_0+1}$ (the one with equal entries) together with the remaining $d-(d-d_0+1) = d_0-1$ coordinates unaffected by $G$. We therefore indeed get $d_0$ total invariant directions.

For the rightmost panel of the figure, we trained a 3-layer MLP with hidden dimension 256 as the classification network.

# B LEARNING THEORETIC CONTEXT FOR $m(p_X)$

To formalize the intuition associated with $m(p_X)$, we piece together some learning theoretic context below.

First, what would the classifier metric actually measure, if we had infinite data? In other words, if $\mathscr{F}$ is our class of neural networks, $\ell$ is a binary classification loss function, $p$ is our data distribution and $\tilde{p}$ is its randomly symmetrized version, we want to understand the following:

$$\min_{f\in\mathscr{F}} \frac{1}{2}\int_x \ell(f(x),0)dp + \frac{1}{2}\int_x \ell(f(x),1)d\tilde{p} \tag{57}$$

Since these are continuous integrals rather than finite-sample approximations, this is an "infinite-data" setting.

In fact, this expression has been studied extensively in various settings (see Sriperumbudur et al. (2009), Lopez-Paz & Oquab (2017) and references within), which usually vary in their choice of $\mathscr{F}$ and $\ell$ (and with $\tilde{p}$ replaced by a more general second distribution $q$). For example, when $\mathscr{F}$ is the set of all measurable functions and $\ell$ is the 0/1 loss, eq. (57) is the optimal Bayes risk, classically known to be a simple affine transformation of the total variation norm.

When instead using the loss function $\ell(\alpha,0)=\alpha$ and $\ell(\alpha,1)=-\alpha$, Sriperumbudur et al. (2009) showed straightforwardly that eq. (57) is exactly the integral probability metric associated with $\mathscr{F}$:

$$\max_{f\in\mathscr{F}} \left| \int_x f(x)dp - \int_x f(x)d\tilde{p} \right| \tag{58}$$

Integral probability metrics recover a range of familiar quantities for different choices of $\mathscr{F}$. For example, when $\mathscr{F}$ consists of all functions with Lipschitz norm bounded by 1, eq. (58) reduces to the Wasserstein metric via Kantorovich-Rubinstein duality. Similarly, when the functions in $\mathscr{F}$ are norm-bounded in some Hilbert space, the resultant integral probability metric is the kernel maximum mean discrepancy (MMD), as used by Chiu & Bloem-Reddy (2023).

For other loss functions and with unrestricted class $\mathscr{F}$, Nguyen et al. (2009) showed that there exists some convex $f$ such that eq. (57) is equal to the corresponding $f$-divergence. For example, when $\ell$ is the exponential logistic loss and $\mathscr{F}$ is all measurable functions, eq. (57) reduces to known divergences (Hellinger and $\chi^2$, respectively).

Thus, while we cannot precisely articulate eq. (57) as it depends on both the exact class of neural networks and the loss function, it reduces to reasonable and familiar quantities in special cases.

We now turn to the finite sample complexity aspect of the metric. Since we cannot truly compute eq. (57), we follow standard learning practice and use a dataset of finite samples to approximate the continuous integrals. Standard generalization bounds apply, restricting how much our finite-sample approximation to eq. (57) can diverge. In particular, let $\delta\in(0,1)$, let $x_i$ be drawn with equal probability from $p$ or $\tilde{p}$ with $y$ denoting the corresponding binary class, and let $\mathscr{R}_m(\ell\circ\mathscr{F})$ be the Rademacher complexity, i.e.

$$\mathscr{R}_m(\ell\circ\mathscr{F}) := \mathbb{E}_{(x_1,y_1)\dots(x_m,y_m)}\mathbb{E}_{\sigma_i}\left[\sup_{f\in\mathscr{F}}\left(\frac{1}{m}\sum_{i=1}^{m}\sigma_i\ell(f(x_i),y_i)\right)\right] \tag{59}$$

Then a standard generalization bound (see e.g. Appendix A of Cohen et al. (2019)) tell us that, with probability $\geq 1-\delta$ over the randomness of the training set, the following holds $\forall f\in\mathscr{F}$:

$$\underbrace{\mathbb{E}_{(x,y)}[\ell(f(x),y)]}_{\text{optimized in } eq.\ (57)} \leq \underbrace{\frac{1}{|S|}\sum_{(x_1,y_1)\dots(x_m,y_m)}\ell(f(x_i),y_i)}_{\text{what we actually optimize}} + 2\mathscr{R}_m(\ell\circ\mathscr{F}) + \sqrt{\frac{8\ln(2/\delta)}{m}} \tag{60}$$

With these tools in hand, we now interpret what learning theory has to say on the impact of the dataset size and model family on $m(p_X)$.

**Impact of dataset size** The dataset size with which we train our metric affects only the generalization bound from finite to infinite sample loss, not the underlying pseudometric itself. According to the generalization bound above, the the dataset size contributes inversely to an additive term in the overall generalization error, and should scale roughly with $\log(1/\delta)$.

**Impact of model family $\mathscr{F}$** The choice of $\mathscr{F}$, i.e. the family of neural networks, affects both the generalization bound eq. (60) and the pseudometric itself eq. (57). In particular, as the architecture class becomes more expressive, the pseudometric eq. (60) grows "stronger" (i.e. can better discern subtle distributional asymmetries, with the TV norm between distributions as the limiting case), but the generalization bound eq. (60) also grows larger (i.e. the risk of overfitting is greater). In practice, of course, generalization bounds are not perfectly predictive of modern deep learning, and more nuanced bounds are possible (e.g. which take into account the complexity of the data distribution itself, rather than just the hypothesis class).

# C Task-dependent metric

## C.1 Derivation and explanation

$m(p_X)$ does not capture whether distributional symmetry breaking contains useful information for the task at hand. If it does, for example in cases of inherent symmetry breaking as in Figure 1, then we predict that performing full-group data augmentation is a poor choice, as it discards task-relevant information contained in the exact position within the orbit. However, if the distributional symmetry breaking is superficial in the sense that it has no relation to the task of interest, then it is more subtle whether full-group data augmentation will hurt performance, as shown in Section 5. As such, we seek to refine the metric from Section 2 to produce a stronger signal for when data augmentation is harmful.

We now derive a potential task-dependent metric from first principles. Intuitively, we wish to capture how much information about the task labels are captured by the non-uniformity in the data points' orbits. Let $c\colon \mathscr{X} \to G$ be a canonicalization function, such that $c(x)$ denotes where on each orbit $x$ is[7]. Since data augmentation and invariant featurizations destroy any information contained in $c(x)$, we wish to understand the dependence between orientations $c(x)$ and labels $y(x)$. A standard information-theoretic quantity for measuring dependence is the mutual information, which is the KL-divergence between the joint distribution and the product of the marginals

$$\mathrm{MI}(c(\cdot), f(\cdot)) := \mathrm{KL}\Big((c(x), f(x)) \,\Big|\Big|\, (c(x), f(x'))\Big)$$

Here, $x$ and $x'$ are independent draws from $p_x$. However, the KL divergence is inefficient to approximate with finite samples, places stringent requirements on the distributions' supports, and does not capture any notion of ease of learnability or computability. Instead, we replace this divergence between product distributions with the classifier distance $d_{class}\Big((c(x), f(x)), (c(x), f(x'))\Big)$ referred to as the task-dependent detection metric below. In other words, we train a small network to classify whether pairs of group elements and labels are mismatched. Note that the task-independent and task-dependent metric are not necessarily correlated; one can be high while the other is low, and vice versa, as verified in Section 5.

One complication for this metric is that it depends on the choice of canonicalization $c(\cdot)$. We assume there is some "natural" choice of $c(\cdot)$, i.e. which is easily computable by a neural network, as we care about the implications of distributional symmetry-breaking on downstream learning tasks. To give an example of a "bad" choice, imagine a $c(\cdot)$ which is discontinuous in $x$, or which is so complex to compute that even if it correlates very well with $f(\cdot)$, it would be difficult for a network to compute it as a feature. Therefore, we parametrize $c(\cdot)$ via a *small* equivariant network, which can be either trained alongside the binary classifier for $d_{class}$ or just randomly initialized.

[7] Formally, all this requires is that $c(gx) = gc(x)$. Although such a map is not well-defined for objects $x$ with self-symmetry, we ignore this issue for the sake of exposition. Note that $c(\cdot)$ makes an arbitrary, but hopefully logical (barring unavoidable discontinuity (Dym et al., 2024)) choice of which $x$ to assign to the identity element of the group.

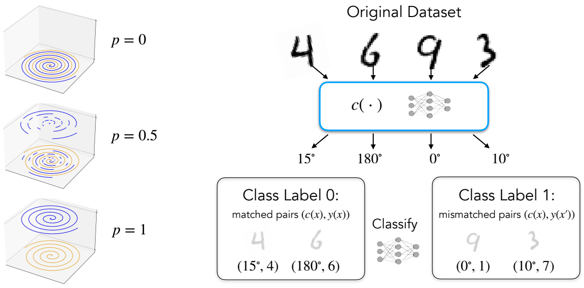

Figure 7: (Left) The swiss roll dataset (Wang et al., 2024b) provides varying levels of dependence between the canonicalization (with respect to the group of discrete vertical translation), and the task. Augmentation by vertical shifts destroys the useful canonicalization of the $p = 1$ dataset, forcing the network to learn a complicated rather than a simple decision boundary. (Right) Input datapoints are assigned orientations by a small equivariant network $c(\cdot)$, and we create pairs of orientations with labels that may or may not match. A binary classifier network then tries to distinguish between matched and mismatched (orientation, labels) pairs, as a proxy for how informative the orientation is for the task.

In Appendix C.3, we show that this metric is closely related to the accuracy of predicting $f(x)$ directly from $c(x)$ (referred to as the direct task-dependent metric in our experiments). This is in turn closely related to the concepts of V-information (Xu & Raginsky, 2017) and the information bottleneck (via the canonicalization) (Tishby et al., 1999). We find empirically that the direct task-dependent metric (preliminary results presented in 5.2), is easier to optimize and the performance is reasonable on test cases.

### C.2 Results

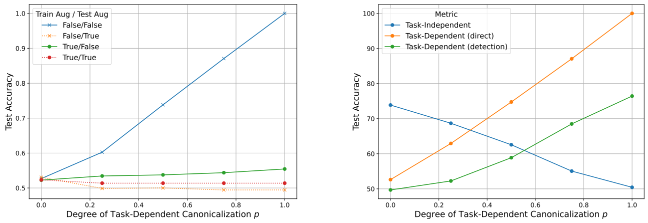

Figure 8: MNIST task-independent metric (left) and swiss roll augmentation performance and metrics (center and right) as functions of dataset canonicalization.

**Swiss Roll** As shown in Figure 7, the swiss roll dataset consists of two interleaved spirals (Wang et al., 2024b). The spirals have distinct $z$ values, so they are easily separable by a horizontal plane. However, there is also a more complex function fitting the data that is invariant to $z$-shifts (the group $Z_2$). Following (Wang et al., 2024b), we create a continuous family of datasets in which only a $p$-fraction of one spiral are separated vertically. This creates a spectrum of tasks, where $p = 1$ is canonicalized in a task-useful way, whereas $p = 0$ is not. We find that augmentation of a simple MLP indeed hurts performance on this task, with the effect increasing along with $p$ (Figure 8). This is captured by the task-dependent metrics, which increases along with $p$. However, the task-independent metric cannot capture the dataset canonicalization, as this would nearly require solving the hard spiral task itself!

To elaborate, we can think of the $p = 1$ distribution as a perfectly canonicalized dataset. The reason that our task-dependent metric does not pick up on this, and instead has only 50% accuracy, is essentially that the canonicalization was not simple – in fact, it effectively solved the prediction task (i.e. given a point $(x, y, -)$, $z$ was set based on $spiral - class(x, y)$). So, it is hard for a small network to detect on its own whether an input is canonicalized or not.

When $p = 0$ (see Figure 3), the classifier knows that any datapoint with $z = 1$ came from the transformed distribution, since the original $p = 0$ distribution always has $z = 0$. The classifier can guess the label corresponding to the original dataset when $z = 0$, and this will achieve 75% accuracy as shown. Moving from $p = 0$ to $p = 1$ simply interpolates between these two scenarios, and this is why the task-independent metric drops. In a sense, as $p$ goes from 0 to 1, we continuously transform from a task-useless canonicalization to a task-useful canonicalization, which is reflected more accurately by the task-dependent metrics.

**MNIST** The task-dependent metric is essentially 50% (related to the small size of $|G| = 4$, Appendix D.2), which is consistent with this behavior.

**QM9** We train both the task-dependent detection metric and the direct task-dependent metric for QM9 to determine if certain properties are more impacted by distributional symmetry breaking than others. We observe that both task-dependent metrics vary slightly per property.

**QM7b Response Properties** The task-dependent detection metric with $c$ untrained for the dipole vector $\vec{\mu}$ yields an accuracy of 66%. For the scalar property $\alpha_{\text{iso}}$, the metric is 52%, thus not yielding a significant signal. This aligns with the intuition that orientation should matter more for predicting vectors than scalars. See Appendix D.7 for further exploration of task-dependent canonicalizations and impacts on predicting $\vec{\mu}$.

**ModelNet40** For the task-dependent detection metric, we follow (Kaba et al., 2023) and use a vector neuron network (Deng et al., 2021) for canonicalization. For the direct prediction task-dependent metric, we use a four-layer MLP. The direct prediction achieves 24.98% accuracy, and binary detection 57.54%—both better than chance, indicating task-informative asymmetry.

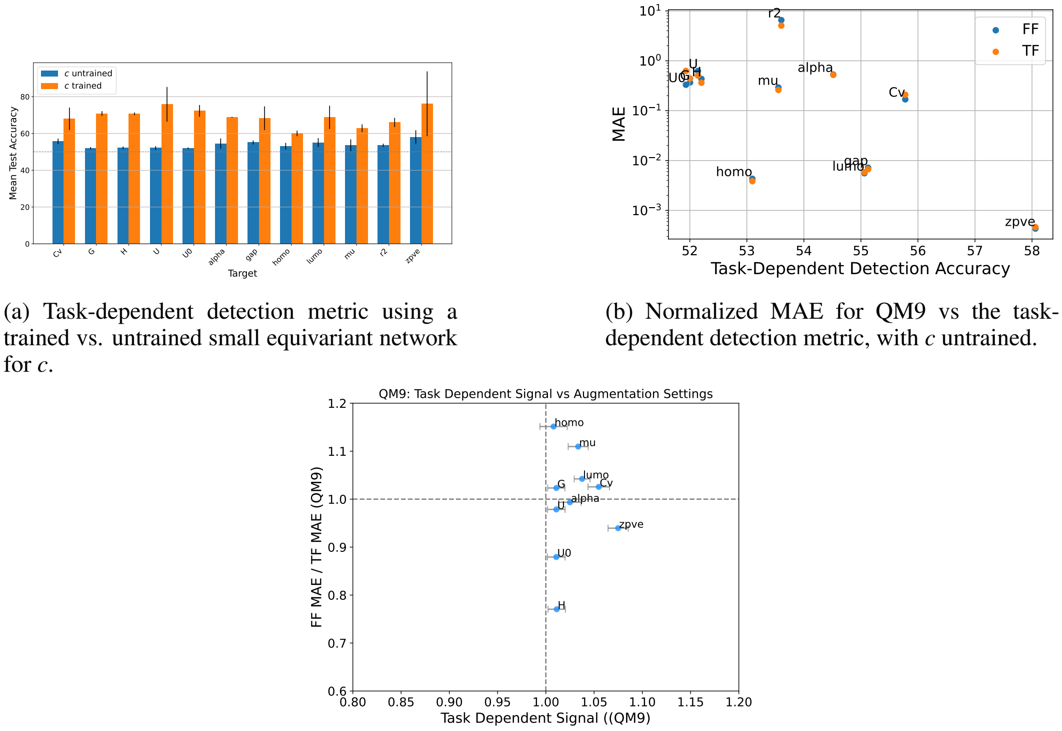

(a) Task-dependent detection metric using a trained vs. untrained small equivariant network for $c$.

(b) Normalized MAE for QM9 vs the task-dependent detection metric, with $c$ untrained.

(c) MAE FF/TF improvement vs QM9 direct task-dependent metric.

Figure 9: QM9 task-dependent detection metric figures with MAE table and plots.

As shown in Table 3 and Table 4, the task-dependent detection metric is overly sensitive to the canonicalization and classifier network architectures.

Table 3: Ablations on the canonicalization network architecture for task-dependent metric, averaged over 2 independent runs on QM9. As shown, there is indeed variation in the task-dependent metric with the architecture of the canonicalization network. Although we expect some variation—since the task-dependent metric is supposed to pick up on a "simple" canonicalization, we did intend to restrict the maximum size of the network—the ablations below surprisingly demonstrate that the highest accuracies were achieved by the smallest networks. We note that the loss curves were fairly unstable, possibly pointing to optimization difficulties with tensor product equivariant networks that might be alleviated for smaller/shallower networks. For a fair comparison in practice, one should fix an architecture size, and only compare accuracies computed with the same architecture.

| Layers | Irrep Dimension | Test Accuracy | Parameters | acc_mean | acc_std | param_float |
|---:|---|:---:|---:|---:|---:|---:|
| 4 | 16x0e + 4x1e | $72 \pm 3$ | 38,000 | 72 | 3.0 | 38,000 |
| 2 | 16x0e + 4x1e | $69 \pm 0.9$ | 19,000 | 69 | 0.9 | 19,000 |
| 2 | 32x0e + 8x1e | $72 \pm 2$ | 74,000 | 72 | 2.0 | 74,000 |
| 4 | 32x0e + 8x1e | $76 \pm 2$ | 150,000 | 76 | 2.0 | 150,000 |
| 3 | 32x0e + 8x1e | $74 \pm 1$ | 110,000 | 74 | 1.0 | 110,000 |
| 3 | 16x0e + 4x1e | $86 \pm 2$ | 29,000 | 86 | 2.0 | 29,000 |
| 2 | 8x0e + 2x1e | $89 \pm 0.1$ | 5,400 | 89 | 0.1 | 5,400 |
| 4 | 8x0e + 2x1e | $89 \pm 0.4$ | 10,000 | 89 | 0.4 | 10,000 |
| 3 | 8x0e + 2x1e | $88 \pm 2$ | 7,900 | 88 | 2.0 | 7,900 |

Table 4: Ablations on the classifier network architecture for task-dependent metric. The classifier network is an MLP, for which we vary the number of layers and the hidden dimension.

| Depth | Hidden Dimension | Test Accuracy | Parameters |
|---:|---:|---:|---:|
| 4 | 32 | 68.2 | 3,800 |
| 4 | 128 | 88.1 | 52,000 |
| 2 | 64 | 88.2 | 5,200 |
| 4 | 64 | 70.0 | 14,000 |
| 8 | 64 | 87.6 | 31,000 |
| 2 | 32 | 74.9 | 1,600 |

### C.3 Theory

For simplicity, throughout this section we assume $c(\cdot)$ is not learned, e.g. coming from a small equivariant network with frozen weights as in the experiments.

We introduced the task-dependent metric as a measure of the dependence between the canonicalization $c(x)$ and the label $f(x)$. Instead of using the mutual information, as below,

$$\text{MI}(c(\cdot), f(\cdot)) := \text{KL}\Big((c(x), f(x)) \,\Big|\Big|\, (c(x), f(x'))\Big),$$

we used the classifier distance (from the task-independent metric) between the joint distribution and the product of the marginals. Recall the classifier distance:

$$d_{class}\,(p_0, p_1)) = \mathbb{E}_{b \sim \text{Bern}(\frac{1}{2})} \mathbb{E}_{x \sim p_b} \left[\mathbb{1}\big(\text{NN}(x) = b\big)\right]$$

Specializing to our distributions, where $p_0$ is the joint and $p_1$ is the product of marginals:

$$\begin{aligned} m_1(c(\cdot), f(\cdot)) := d_{class}\left((c(x), f(x)), (c(x), f(x'))\right) = & \frac{1}{2}\mathbb{E}_x \left[\mathbb{1}\big(\text{NN}(c(x), f(x)) = 0\big)\right] + \\ & \frac{1}{2}\mathbb{E}_{x,x'} \left[\mathbb{1}\big(\text{NN}(c(x), f(x')) = 1\big)\right] \end{aligned}$$

In other words, we assess a classifier (NN)'s ability to distinguish between pairs of canonicalization and label that are matched, vs mismatched. In practice, we of course train NN on a training set, and then approximate this expectation via a held-out test set.

However, another natural measure of the dependence between $c(x)$ and $f(x)$ is to assess how predictive $c(x)$ is of $f(x)$, that is: how well can a neural network predict $f(x)$ directly from $c(x)$? If there is no dependence between them, then it can do no better than random. Letting $\ell$ be a loss function, we define

$$m_2(c(\cdot), f(\cdot)) := \mathbb{E}_{x,x'}\left[\ell(\mathrm{NN}'(c(x)), f(x'))\right] - \mathbb{E}_x\left[\ell(\mathrm{NN}'(c(x)), f(x))\right]$$

Here, the second term captures how well $c(x)$ can be used to predict $f(x)$, while the first term regularizes/calibrates by how well NN performs with independent inputs.

Intuitively, $m_1$ and $m_2$ are quite related to each other, and it is a straightforward exercise to make this precise. Letting $\ell$ be the $0/1$ loss (i.e. 0 if $\mathrm{NN}'(c(x)) = f(x)$ and 1 otherwise), one can obtain one direction of a bound between $m_1$ and $m_2$ by using NN' to define NN. In particular, define $\mathrm{NN}(c, f) := 0$ if $\mathrm{NN}'(c) = f$, and 1 otherwise. Then,

$$\begin{aligned}
m_2(c(\cdot), f(\cdot)) &:= \mathbb{E}_{x,x'}\left[1 - \mathbb{1}(\mathrm{NN}'(c(x)) = f(x'))\right] - \mathbb{E}_x\left[1 - \mathbb{1}(\mathrm{NN}'(c(x)) = f(x))\right] \\
&= \mathbb{E}_x\left[\mathbb{1}(\mathrm{NN}'(c(x)) = f(x))\right] - \mathbb{E}_{x,x'}\left[\mathbb{1}(\mathrm{NN}'(c(x)) = f(x'))\right] \\
&= \mathbb{E}_x\left[\mathbb{1}(\mathrm{NN}(c(x), f(x)) = 0)\right] - \mathbb{E}_{x,x'}\left[\mathbb{1}(\mathrm{NN}(c(x), f(x')) = 0)\right] \\
&= \mathbb{E}_x\left[\mathbb{1}(\mathrm{NN}(c(x), f(x)) = 0)\right] - \mathbb{E}_{x,x'}\left[1 - \mathbb{1}(\mathrm{NN}(c(x), f(x')) = 1)\right] \\
&= 2m_1(c(\cdot), f(\cdot)) - 1
\end{aligned}$$

In the other direction, we could start with NN and define $\mathrm{NN}'(c)$ to be any $f$ such that $\mathrm{NN}(c, f) = 0$.

Therefore, when optimizing independently over NN and NN', $m_2$ is at least $2m_1 - 1$, while at the same time, $m_1$ is at least $\frac{m_2+1}{2}$. The two quantities are thus related by an affine transformation — at least under a certain choice of loss (and optimization practicalities notwithstanding).

These quantities are also very related to $V$-information (Xu & Raginsky, 2017). In particular, when $\ell$ in the definition of $m_2$ is the cross-entropy loss, $m_2$ is essentially the predictive $V$-information from $c(\cdot)$ to $f(\cdot)$ (Xu & Raginsky, 2017). In subsequent experiments, when we report $m_2$ (the "task-dependent direct prediction" metric), we report only the latter term $\mathbb{E}_x\left[\ell(\mathrm{NN}'(c(x)), f(x))\right]$.

#### C.3.1 Task-dependent metrics for finite and infinite groups

When $G$ is finite and $|G|$ is much smaller than the number of class labels, then it is clear that $c(x)$ can not be expected to predict $f(x)$ perfectly (hence the role of the first term in the expression for $m_2$). In the case of MNIST, for example, the group of 90° rotations has 4 elements, while there are 10 digits to classify (which occur with equal probabilities). Therefore, directly predicting the digit label from $c(x)$ is impossible, regardless of the dataset distribution; one can only associate one label to each of the four elements of $c(x)$. (Indeed, Fano's inequality can provide a lower bound on this probability of error.)

On the other hand, when $G$ is infinite and the dataset is essentially canonicalized according to our main, task-independent metric, an element $c(x) \in G$ can information theoretically capture exactly the identity of $x$, i.e. such that $x$ can be recovered from $c(x)$, for sufficiently expressive choice of $c$. The extent to which this generalizes will depend on the smoothness of the canonicalization, but not necessarily on how "task-correlated" it is (if NN is powerful enough to simply recover $x$ from $c(x)$ and use it to predict $f(x)$). Thus, considering the version of the task-dependent metric that aims to predict $f(x)$ directly from $c(x)$, overfitting is a concern, and may explain some of the sensitivity to architecture choice from Table 3 and Table 4.

### C.4 Practical Flowchart for Practitioners

We present a flowchart (Figure 10) that practioners can use to determine how to use $m(p_X)$ and the task-dependent metric and what the implications may be.

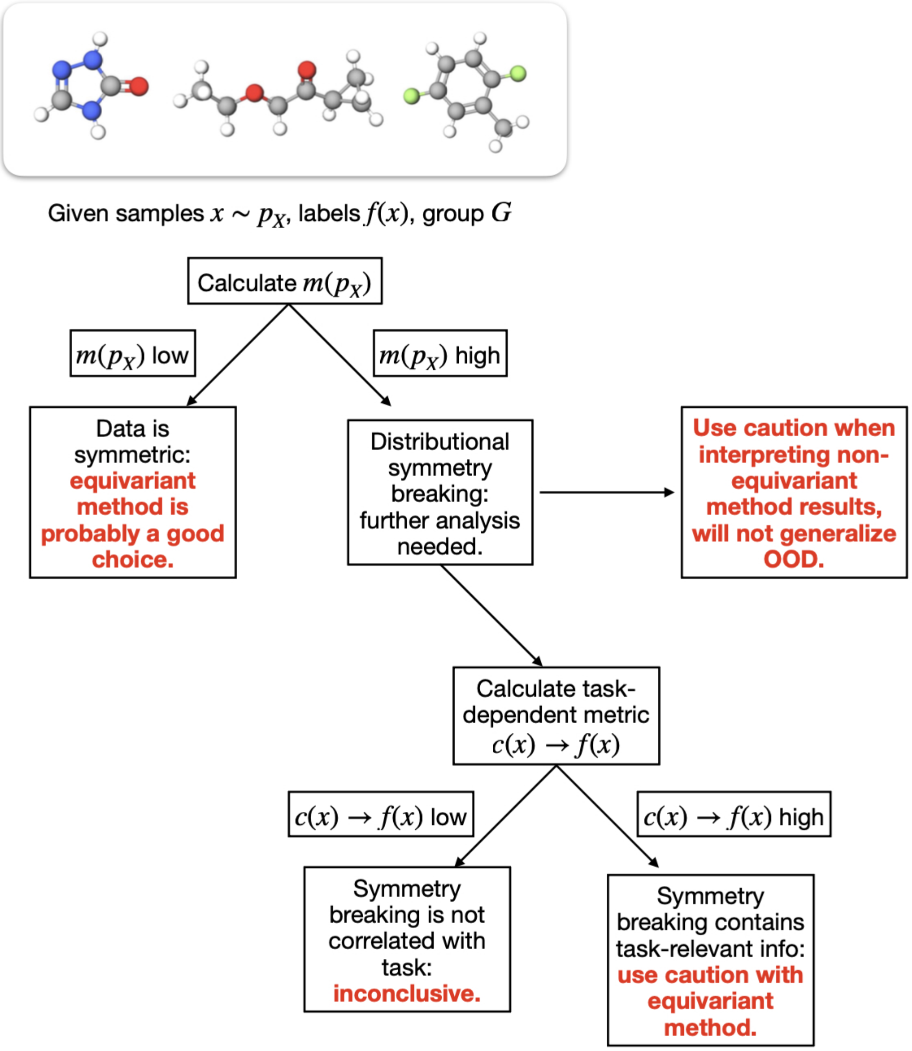
Given samples $x \sim p_X$, labels $f(x)$, group $G$
Calculate $m(p_X)$
$m(p_X)$ low
$m(p_X)$ high
Data is symmetric: equivariant method is probably a good choice.
Distributional symmetry breaking: further analysis needed.
Use caution when interpreting non-equivariant method results, will not generalize OOD.
Calculate task-dependent metric $c(x) \rightarrow f(x)$
$c(x) \rightarrow f(x)$ low
$c(x) \rightarrow f(x)$ high
Symmetry breaking is not correlated with task: inconclusive.
Symmetry breaking contains task-relevant info: use caution with equivariant method.

Figure 10: Advice for practitioners on using our metrics for model selection.

# D EXPERIMENTS

For all experiments, we provide further details on the training, model specifications, and results. To reproduce our experiments, we include a `README.md` file in the supplemental codebase, specifying the exact commands for each dataset and setting. We also summarize the task-independent metric in Table 5. As shown, every dataset experiences distributional symmetry-breaking, to varying (but all high) degrees.

| **Dataset** | **Test Acc.** |
|---|---|
| rMD17 Aspirin | 97.869 |
| rMD17 Ethanol | 79.834 |
| OC20 Surface+Adsorbate | 99.280 |
| OC20 Adsorbate | 96.529 |
| QM9 | 97.6 |
| Local QM9 | 67.6 |
| QM7b | 89.93 |
| MNIST | 87.50 |
| ModelNet40 | 92.45 |
| Local ModelNet40 $N = 10$ | 55.6 |
| Local ModelNet40 $N = 100$ | 81.5 |
| LLM Materials | 95 |

Table 5: Task-independent metric on selected datasets (omitting the toy Swiss Roll dataset and ModelNet40 reported per class in Figure 12).

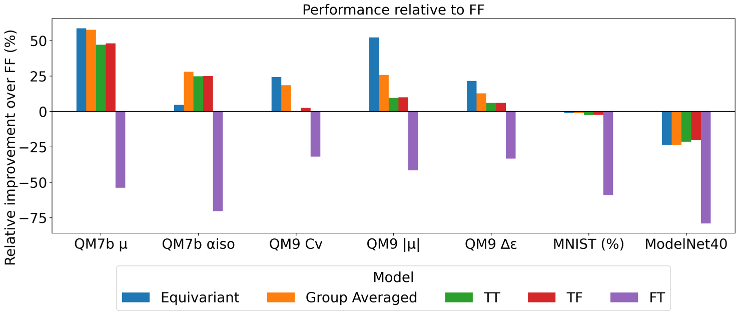

Figure 11: To complement Table 1, we show the percentage improvement relative to the FF setting for the different augmentation settings (TT, TF, FT), equivariant, and group averaged models. We see that the relative improvement is largest for the vector quantity $\vec{\mu}$, and there is no improvement for MNIST/ModelNet40.

## D.1 MODELNET40

### D.1.1 CLASSIFICATION RESULTS ON TRANSFORMER MODEL

To show that the results in the main text are not specific to the Graphormer architecture, we also run experiments with a transformer architecture. We train a transformer with the four different augmentation settings and report the test accuracies: TF=76.778%, TT=75.723%, FT=7.86%, and **FF=84.49%**. Thus, for this dataset, FF setting is better which aligns with the results in the main text.

### D.1.2 RELATION BETWEEN THE DEGREE OF CANONICALIZATION AND ACCURACY ON FF/TF AUGMENTATION SETTINGS PER CLASS

We show the scatterplot of the FF/TF test accuracy vs. the degree of canonicalization per class in Figure 12. As above, FF indicates no augmentation at train or test time and TF indicates augmentation at train but not test time. We do not notice a trend in the relative improvement between FF and TF as a function of the task-independent metric, but is interesting to note a weak positive trend between the task-independent metric and both test accuracies. It is unclear why this is the case. We hypothesize that perhaps certain classes are defined by simple features, which would then tend to result in both the task-independent metric and the test accuracy being higher – but further exploration is needed to truly explain this phenomenon.

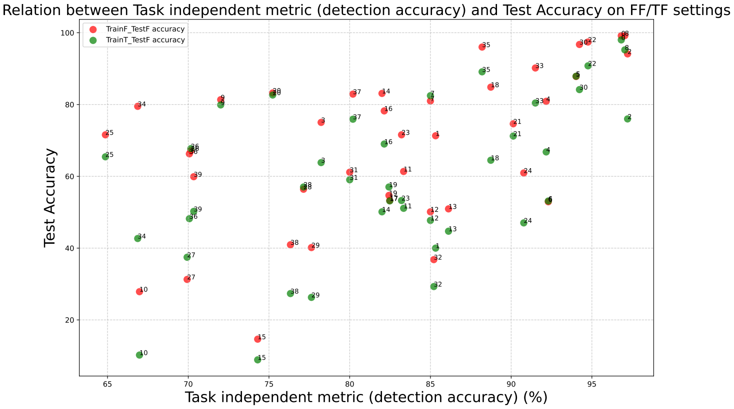

Figure 12: Relation between task independent metric and accuracy on FF/TF augmentation settings.

### D.1.3 Training Curve

We show the training curve of ModelNet40 classification task with different augmentation settings in Figure 13. The training curve shows that the FF setting achieves the best performance all the time, while TF and TT settings achieve similar performance, and FT setting achieves the worst performance. It is interesting to contrast this result with QM9, where the best-performing setting on the unaugmented test-set is to still augment (TF). This suggests a fundamental difference between ModelNet40 and QM9.

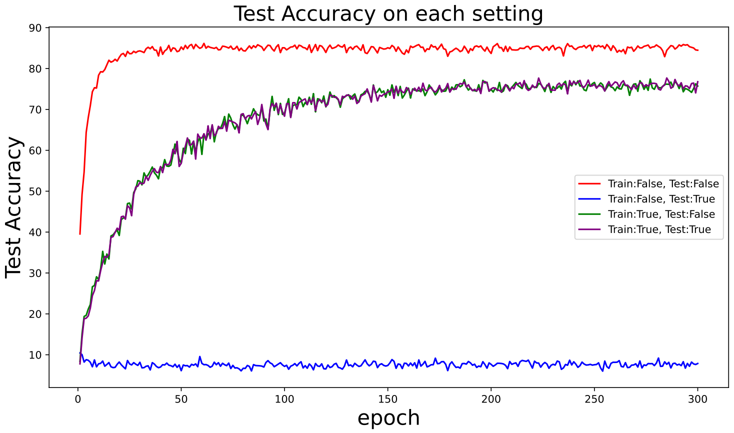

Figure 13: Test accuracy curve of ModelNet40 classification task with different augmentation settings.

### D.1.4 Model details

For training the task-independent metric, we use a four layer transformer architecture with four attention heads and 128 hidden dimensions as the backbone. The number of parameters in the model is 793k. For the task-dependent detection metric and task-dependent direct prediction metric, we use a three layer vector neuron network (Deng et al., 2021) as the canonicalization network, and a four layer MLP as the prediction backbone, respectively. The number of parameters for the vector neuron network is 6.1K, and for the MLP is 14.2K for direct prediction and 13.8K for detection. To ensure fair model comparison, we use the Graphormer model used in QM9/QM7b for the classification task in the main text Shi et al. (2022). In this setting, each point cloud is uniformly downsampled to 512 points. We run the base Graphormer setup with 4 blocks, 6 transformer layers, 8 heads, an FFN width of 256, and distance encodings using 32 Gaussian kernels. The regularization applied is dropout=0.1 on attention and on the final layer only—no dropout is used on inputs or intermediate activations. The number of parameters in this model is 822K.

For the equivariant counterpart, we build on e3nn(Geiger et al., 2022; Kleinhenz & Daigavane). Graph edges are defined via k-nearest neighbors with $k = 15$. Point embeddings are first lifted to the mixed representation irreps hidden = 64x0e + 16x1o. Edge attributes derive from relative offsets within a cutoff distance (max radius = 5.0) and are then expanded in spherical harmonics with irreps sh = 1x0e + 1x1o to encode angular structure. We stack three equivariant convolutional stages with gated nonlinearities and include linear self-interaction terms. The head performs global node pooling and an equivariant MLP, producing outputs with irreps out = 40x0e. The number of parameters in this model is 772K.

For the transformer baseline, the architecture we use is a six layer transformer architecture with eight attention heads and 256 hidden dimensions as the backbone. The number of parameters in this model is 4.7M.

### D.1.5 TRAINING DETAILS

The data split for all ModelNet40 experiments is 80/10/10 for training/validation/testing. The training details of classification experiments in the main text are as follows: Graphormer uses Adam with learning rate 1e$-$4 and batch size 16. The e3nn uses Adam at 1e-3 with batch size 16. To make the comparison fair, we implement a stochastic, group-averaged Graphormer: at each forward pass we sample $n = 3$ random rotations from $SO(3)$, run the network on each, and average the resulting predictions. For transformer models, we trained each setting for 300 epochs with batch size 128.

We train the task-independent metric for 30 epochs, the task-dependent detection metric for 1200 epochs and the direct prediction task-dependent metric for 300 epochs. All models are trained on one NVIDIA GeForce RTX 4090. The training time for the task-independent metric was about 20 minutes, for the task-dependent detection metric was about 9.5 hours, and the direct prediction task-dependent metric was about 8.5 hours. The classification task took about two hours and a half for each setting for transformer model. For graphormer model, it will take about 8 hours for each setting. For the equivariant model, it will take about 16 hours for each setting.

## D.2 MNIST

### D.2.1 Training and model details

All experiments were run on a single NVIDIA RTX A5000 with batch size 128, 50 epochs, and standard 3e-4 learning rate for the Adam optimizer, which took roughly 30 minutes each. For the data splits, we split the original training set of 60k images, and split it into 60%/20%/20% for train, validation, and test. MNIST training runs with/without augmentation used as a base network a basic 421k-parameter CNN with two convolutional layers, followed by a two-layer MLP. For the task-independent metric, the training hyperparameters and model architecture were the same, with only the final number of model outputs modified from 10 to 2. The group-averaged model used this base architecture taking the average over the $C_4$ group at each forward pass. Note this is equivalent to an equivariant model over a discrete group.

For the task-dependent detection metric, we use as the canonicalization network $c(\cdot)$ a 19k-parameter 90°-rotation equivariant classifier outputting a four-dimensional vector, corresponding to the four elements of $G$ (90°-rotations). (The classifier essentially applies a 2-layer CNN to all four rotations of the input image.) To obtain a single element of $G$ from this vector, we simply apply a softmax with low temperature (1e-3), effectively setting it to be one-hot at the index of maximum value. For the network that predicts a binary class from pairs $(c(x), f(x))$, we simply concatenate all of these inputs into a 4-layer 13.5k-parameter MLP, with 64 hidden features per layer.

### D.2.2 Task-independent and -dependent metrics

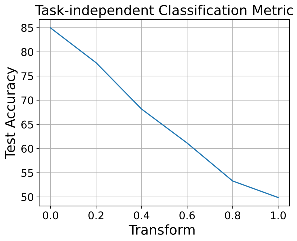

Figure 14: MNIST task-independent metric as function of proportion randomly rotated.

In Figure 14, we report $m(p_X)$ as a function of what fraction of the dataset was randomly rotated, and recover the predicted optimal accuracies.

In Figure 15 and Figure 16, we report the task-dependent metrics. They all performed quite poorly, possibly as a result of on how much information can be encoded in a canonicalization with respect to a group of only four elements (see Appendix C.3), or possibly because the orientation is not practically that informative for most of the digits (despite the 6/9 toy example).

### D.2.3 Loss curves

See fig. 17. We can also analyze the test accuracy per class as in fig. 18.

### D.2.4 Selective augmentation using the trained classifier

We have focused on evaluating whether or not a dataset with equivariant labels has distributional symmetry breaking, and what the implications are on whether or not to employ group augmentation. However, augmenting versus not augmenting does not have to be a strict dichotomy – one can apply a restricted set of augmentations, or only on certain datapoints. Indeed, this is the approach taken by methods which learn how to augment, including e.g. Augerino (Benton et al., 2020b). We now explore how one might selectively augment using our trained classifier, interpolating between full data augmentation (when there is no distributional symmetry-breaking) and no data augmentation (when there is significant distributional symmetry-breaking).

As a first step towards this goal, we use the binary classifier (that was trained to compute $m(p_X)$) as part of a *mechanism for deciding how to augment an input datapoint*. For now, we use a simple

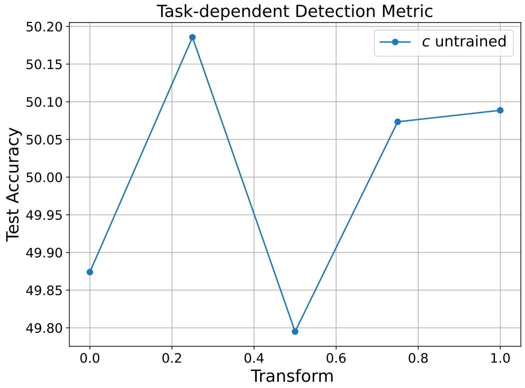

Figure 15: MNIST task-dependent detection metrics.

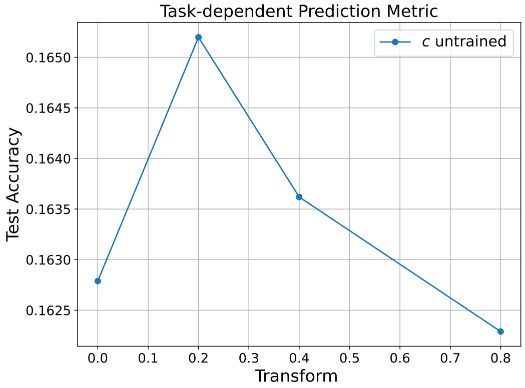

Figure 16: MNIST task-dependent prediction metrics.

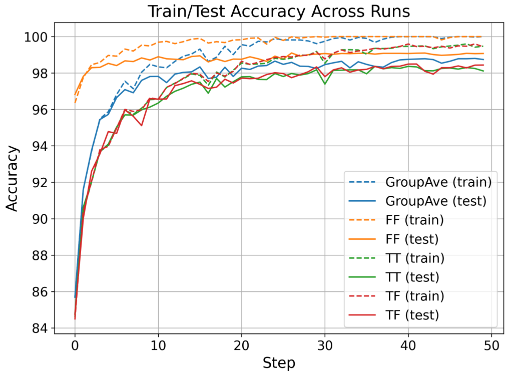

Accuracy over the course of training for the MNIST classification task, in different augmentation settings (“TF” = augmentation for training, no augmentation for testing, etc).

Figure 17: MNIST loss curves. Dashed lines indicate test losses, while solid lines indicate train losses. We omit the FT setting as the test accuracy was around 40%.

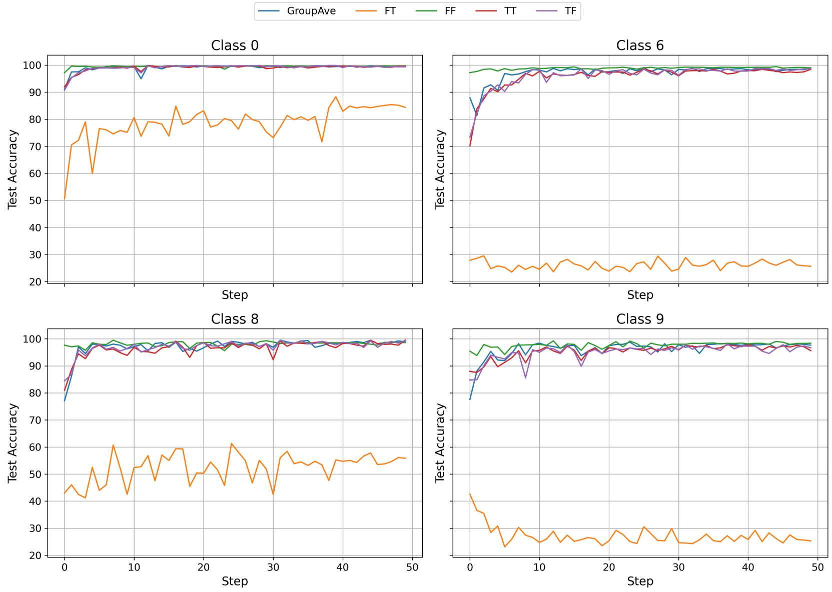

Figure 18: MNIST loss curves per selected classes. It is interesting to note the variability in the FT setting, which corresponds to whether test-time augmentation destroys useful information or not. For example, FT is much worse than the other settings for 6/9. However, for more symmetric shapes like 0/8, FT performs better.

heuristic as a proof of concept, but more advanced methods of harnessing the classifier should be possible. In particular, we threshold at 0.45 the probability the trained classifier placed on each rotation of the input being from the original (non-rotated) half of the dataset. We then only augment from the set of per-datapoint elements which pass this threshold. The threshold is a hyperparameter, but our rationale for choosing 0.45 is based on the behavior of an optimal classifier on a simplified dataset with finite orbits, as evaluated at the end of section 2. In particular, for an input $x$, let $\mathcal{O}_x := \{gx : g \in G\}$ be the orbit of $x$, and let $S \subseteq \mathcal{O}_x$ denote the subset of the orbit of $x$ on which the natural data distribution places probability mass. For simplicity, we assume each element of $S$ is equally likely under the data distribution. The true log odds between the original dataset and the rotated dataset, for each datapoint, is $\frac{1/m}{1/|\mathcal{O}_x|} = \frac{\mathcal{O}_x}{m} := r$. Setting $\frac{p}{1-p} = r$, we obtain $p = \frac{r}{1+r}$. Thus, for inputs $x$ in the support of the data distribution, the optimal $p$ can range between $\frac{1}{2}$ – when all elements of the orbit appear under the data distribution (no distributional symmetry breaking) – and $\frac{|\mathcal{O}_x|}{|\mathcal{O}_x|+1}$ – when only one element of the orbit is natural to the data distribution. Thus, we threshold near 0.5, augmenting only on inputs that the classifier believes are likely to fall in-distribution. In an ideal world, this method should automatically interpolate between "no augmentation" and "full augmentation": if the classifier is always 50/50, then we always augment, and if the classifier is very confident that a datapoint is or is not natural, we do or do not augment accordingly.

In Figure 19, we try this out with three variants of MNIST: with the original dataset ("None"), a rotated version ("All"), and a partially rotated version with only certain digits rotated ("345"). To make the task harder and therefore benefitting from augmentation, we randomly select a subset of 1,000 images to use. The selective augmentation method described above automatically interpolates between no augmentation and full augmentation, performing near the best of the two in each case. These are promising first results, and can be investigated further in future work.

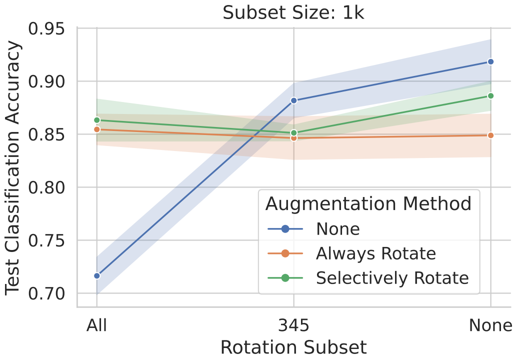

Figure 19: Classification results with a CNN using selective augmentation, averaged over 4 trials. In each trial, a new data split was used and a new detection network was trained.

## D.3 Swiss Roll

### D.3.1 Training and model details

All experiments were run on a single NVIDIA RTX A5000. The swiss roll dataset was originally proposed by Wang et al. (2024c), and as described in the main body, consists of two interleaved spirals with different labels, separated by a horizontal plane. In our work, we modified the swiss rolls of their extrinsic equivariance setting by adding a hyperparameter $p$, to denote how much of the data on top spirals are randomly chosen to be flipped to the bottom spiral.

All experiments were trained with the Adam optimizer with learning rate 3e-4, batch size 100, and for 150 epochs. The model is a 3-layer 67k-parameter MLP for the original classification task and for the detection task; for the task-dependent metrics, a $C_2$-equivariant network with 3k parameters is used to canonicalize, composed with a 4-layer 13k-parameter MLP to perform the final prediction. The dataset consists of $1,000$ examples, split randomly as 60%/20%/20% train/validation/test.

### D.3.2 Loss curves

See Figure 20 and Figure 21.

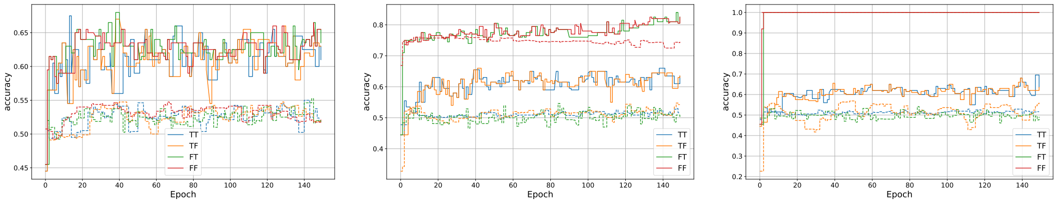

(a) $p = 0$

(b) $p = 0.5$

(c) $p = 1.0$

Figure 20: Accuracy over the course of training for the swiss roll classification task, in different augmentation settings ("TF" = augmentation for training, no augmentation for testing, etc). Dashed lines indicates test losses, while normal lines indicate train losses.

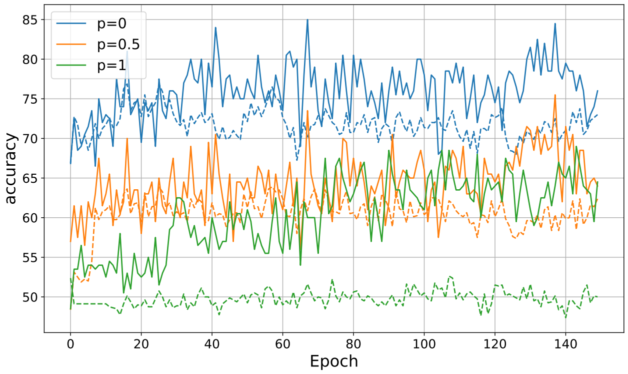

Figure 21: Accuracy over the course of training for the task-independent detection metric on the swiss roll dataset, at different levels of task-correlatedness ($p$). Dashed lines indicates test losses, while normal lines indicate train losses.

### D.4 QM9

The test accuracy for the task-independent metric was 97.60%, indicating a high degree of canonicalization in the QM9 dataset. We now describe setup details, as well as further experiments on (1) the symmetry-breaking of local motifs and (2) interpreting the learned classifier.

#### D.4.1 Dataset, Models, and Training Details

We obtain the QM9 dataset (Ramakrishnan et al., 2014) from `https://doi.org/10.6084/m9.figshare.c.978904.v5`. The original dataset has 133885 molecules, 3054 of which are uncharacterized, as found in `https://springernature.figshare.com/ndownloader/files/3195404`. The uncharacterized molecules are removed during preprocessing. We follow (Anderson et al., 2019) and split the dataset into training/validation/test partitions consisting of 100k, 18k, and 13k molecule examples.

For the task-independent metric, we train a generic transformer architecture with 812k parameters for 20 epochs and the Adam optimizer at learning rate 1e-5 and batch size 128. For the task-dependent metrics, we used a 3-layer, 28.5k parameter e3nn canonicalization network, using Gram-Schmidt orthogonalization to turn the `2x1e` outputs into a proper rotation matrix, and a basic 4-layer, 13.8k parameter MLP for the final task-dependent predictions. We used the Adam optimizer with learning rate 3e-4, 50 epochs, and batch size 128.

For the regression tasks, as we are studying the need for data augmentation, the principal model used should be non-equivariant/non-invariant. We note that many of the recent top performing models on QM9 are equivariant or invariant, so we use a slightly older Graphormer Shi et al. (2022); Ying et al. (2021) architecture from 2021. We include an embedding depending on the position of each atom (not solely the relative position) so the model is not invariant. Each node in the graph thus has a scalar feature (the atom number) and a 3D position associated with it. We use an embedding dimension $d_{\text{embed}} = 128$ for both the atom positions (embedded with a learnable linear layer) and for the atom types. The edges between atoms are encoded using a set of learned Gaussian radial basis functions. We adopt the following parameters of the Graphormer base architecture: 4 blocks, 8 layers, 32 attention heads, a feedforward dimension of 128, and 32 Gaussian kernels for distance encoding. Regularization uses a dropout rate of 0.1 for both attention and final layer dropout, with no input or activation dropout. We train a separate model for each property with different data augmentation settings (TT = train/test augmented, FF = none, TF = train-only, FT = test-only). For training Graphormer, we use the Adam optimizer with a learning rate of $3e-5$.

For QM9 property regression, we compare to a simple equivariant convolutional neural network architecture using e3nn(Geiger et al., 2022; Kleinhenz & Daigavane), as by equivariance, predictions should not change whether train/test are augmented or not. The network uses a learnable embedding (embedding dimension = 32) for atomic species and lifts the atom embeddings into a mixed representation `irreps hidden = 64x0e + 16x1o`. Edge features are computed through relative between atoms within a cutoff radius (`max radius = 5.0`). These features are then projected to spherical harmonics transforming as `irreps sh = 1x0e + 1x1o`, capturing the angular dependence. Radial dependence is captured via Gaussian radial basis functions applied to interatomic distances. We then use 3 layers of equivariant convolutions with gated non-linearities and linear self-interactions. The final layer pools over nodes and uses an equivariant MLP to return the final output as `irreps out = 1x0e` (a scalar for example for predicting one of the QM9 properties). The E3ConvNet model is trained with the Adam optimizer and a learning rate of $1e-4$. For an apples to apples comparison, we implement a stochastic group-averaged variant of Graphormer, in which $n = 5$ random rotations of the input are sampled from $SO(3)$ at each forward pass, and the corresponding outputs are averaged to produce the final prediction. While neither of these architectures are near state-of-the art for QM9, for our studies it suffices to use smaller models (each with approximately 800k parameters) to understand how augmenting impacts results. For both the e3nn model and the Graphormer model with augmentation settings for each property , we train each model for 150-200 epochs (depending on property) on a NVIDIA RTX A5000, which takes 2-3 hours. Minimum test MAE values and test MAE curves are reported in Table 6 and Figure 22.

Table 6: MAE on the QM9 dataset for Graphormer under different data augmentation settings (TT = train/test augmented, FF = none, TF = train-only, FT = test-only). We include an e3nn convolutional neural network model with a similar number of parameters for comparison. The best-performing model is in bold, and the best performing-model within the augmentation settings is underlined.

| Target | Unit | TT | FF | TF | FT | E3NN | GroupAve |
|---|---|---|---|---|---|---|---|
| $\mu$ | D | 0.263 | 0.291 | 0.262 | 0.412 | **0.139** | 0.216 |
| $\alpha$ | $a_0^3$ | 0.523 | 0.516 | 0.519 | 0.793 | **0.382** | 0.410 |
| HOMO | eV | 0.100 | 0.116 | 0.101 | 0.153 | 0.102 | **0.094** |
| LUMO | eV | 0.133 | 0.139 | 0.133 | 0.188 | **0.105** | 0.114 |
| $\Delta\varepsilon$ | eV | 0.183 | 0.195 | 0.183 | 0.260 | **0.153** | 0.170 |
| $R^2$ | $a_0^2$ | 5.763 | 5.253 | 5.707 | 9.624 | 4.908 | **3.049** |
| ZPVE | eV | 0.012 | 0.012 | 0.013 | 0.013 | 0.012 | **0.009** |
| $U_0$ | eV | 10.214 | 8.951 | 10.178 | 12.798 | 13.992 | **3.996** |
| $U$ | eV | 9.764 | 9.274 | 9.477 | 12.583 | 11.403 | **5.796** |
| $H$ | eV | 10.705 | 8.244 | 10.699 | 11.561 | 12.648 | **5.642** |
| $G$ | eV | 8.784 | 8.461 | 8.268 | 12.132 | 14.666 | **5.599** |
| $c_v$ | cal/mol K | 0.157 | 0.158 | 0.154 | 0.207 | **0.119** | 0.128 |

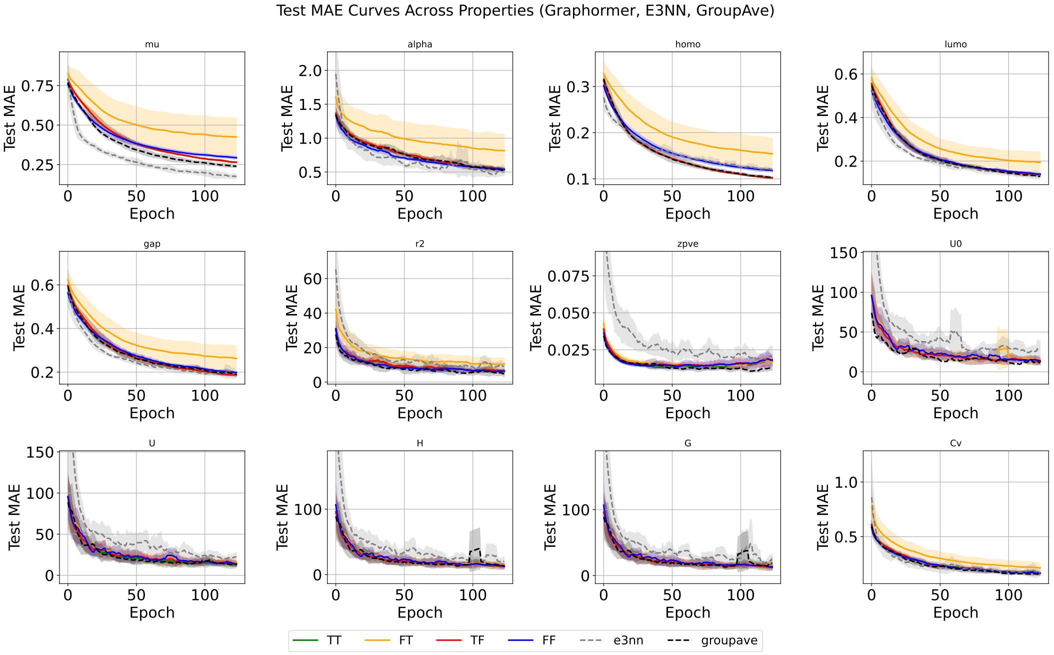

Figure 22: Test MAE per epoch for QM9 predicted properties using the Graphormer-like architecture. We show the augmentation types train/test aug=TT, train aug only=TF, test aug only=FT, no aug=FF. We also show an E3NN network with a similar number of parameters and a group-averaged graph transformer.

### D.4.2 Validation of Task-Independent Metric and p-values

As noted briefly in the main text, it is possible to obtain p-values from our method in the same way as Chiu & Bloem-Reddy (2023).

Figure 24 demonstrates the values used in our computation of the p-values for each method (on a row) and different levels of augmentation in the detection dataset (column). The p-value plots were computed using 20 samples (for each histogram) of size 1k, trained for 20 epochs (in the case of the classifier metric). All methods exhibit the expected behavior: as the augmented fraction increases —i.e. as the distribution becomes more similar to the reference, perfectly symmetrized

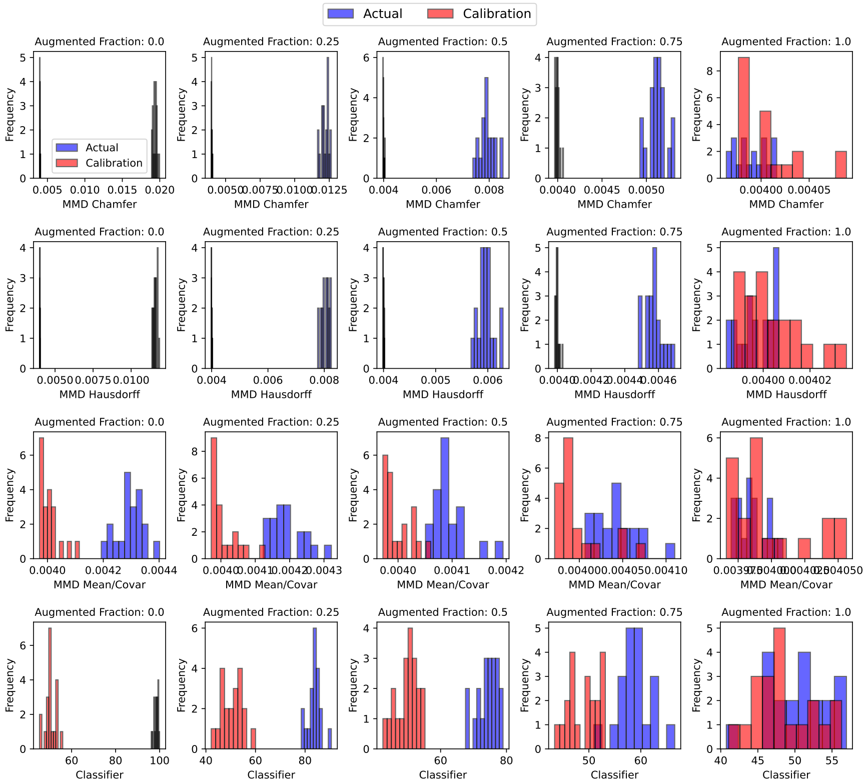

Figure 23: Distance metrics for different methods, and at different levels of augmentation for benzene (i.e. different levels of underlying distributional similarity).

distribution—the distance decreases. See also Figure 26 for the p-values; note that all methods agree at the level of p-value on the original dataset.

### D.4.3 Interpretability of Classifier for Distributional Symmetry Breaking

A primary motivator for using the classifier distance for distributional asymmetry detection is because of the opportunity to explore and interpret the trained classifier. As a first step, we focus on the task-independent classifier trained on the QM9 dataset with Anderson splits as outlined in the previous section. To probe the decision boundary, we evaluate the classifier predictions on the test set with no augmented rotations (e.g. all have label 0 and are from the original dataset). It is thus easy to interpret which molecules are "hard" for the classifier to distinguish as being from the original dataset. We apply PCA to the learned embeddings (i.e., the layer immediately preceding the final output layer) and visualize them in Figure 28, revealing that the misclassified examples tend to cluster together in PCA space.

We evaluate the sigmoid of the classifiers logits on a discrete grid of 3D rotations (representing the probability that the given sample has label 0 or is from the original dataset rather than the augmented version). In order to visualize the probabilities over $SO(3)$, rotations with non-negligible probability are plotted as dots using a Mollweide projection (Murphy et al., 2022; Klee et al., 2023), with rotations orthogonal to the sphere encoded as colors and the size of the dot representing the magnitude of the probability. We explore correctly classified molecules, incorrectly classified molecules, and samples that are close to the decision boundary and show examples of each. We also investigate the stability and robustness of the classifier's decision boundary by identifying rotations of a given sample that lead to a change in its predicted label. To probe the stability of the classifier, we identify

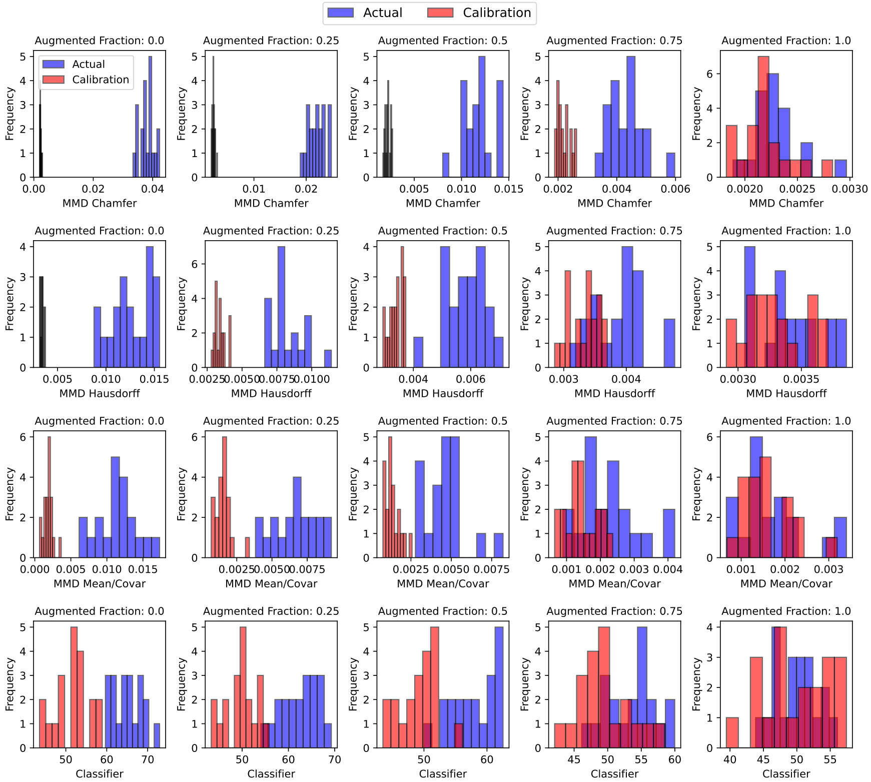

Figure 24: Distance metrics for different methods, and at different levels of augmentation (i.e. different levels of underlying distributional similarity).

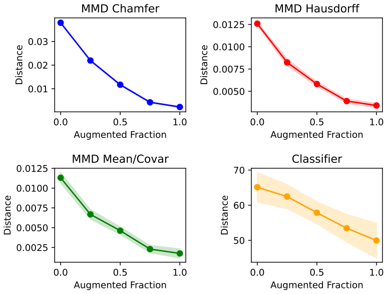

Figure 25: Different distance metrics from a perfectly symmetrized distribution, as a function of the degree of synthetic augmentation of the QM9 dataset. (Higher augmented fraction indicates a greater similarity to the symmetrized distribution.)

pairs of rotations that are close together yet lead to large changes in the classifier's output logits. Given two rotations represented by quaternions $p, q$, the distance between rotations is

$$\theta = 2 \arccos |<p,q>| \tag{61}$$

**Example Correctly Classified with High Probability.** We select a sample classified correctly with high probability as being from the original dataset and investigate the classifier outputs per rotation angle, as shown in Figure 29.

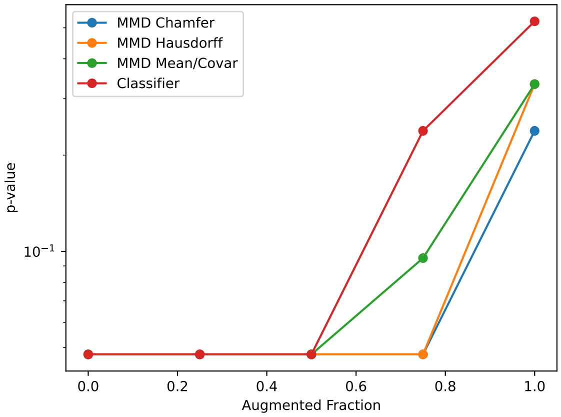

Figure 26: p-values for different methods, and at different levels of augmentation (i.e. different levels of underlying distributional similarity).

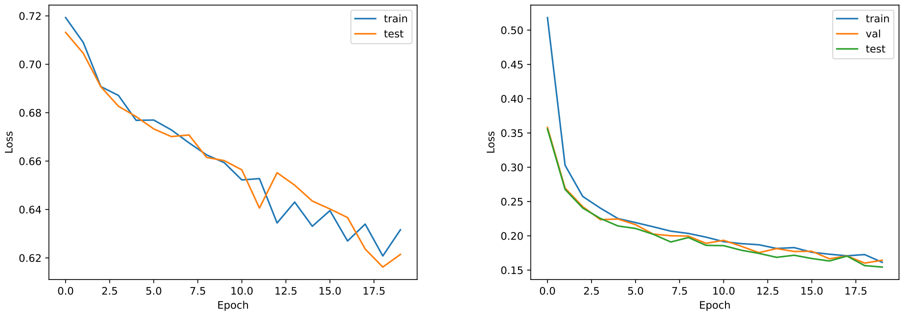

Figure 27: Left: the loss curve from one of the 20 training runs used to compute the classifier distance in the p-value computation, on 1k examples. Right: the loss curve from a training run used to compute the classifier distance over the full dataset. As shown, the loss converged much faster for the full dataset, whereas with only 1k examples (one one-hundredth of the size), convergence is much slower.

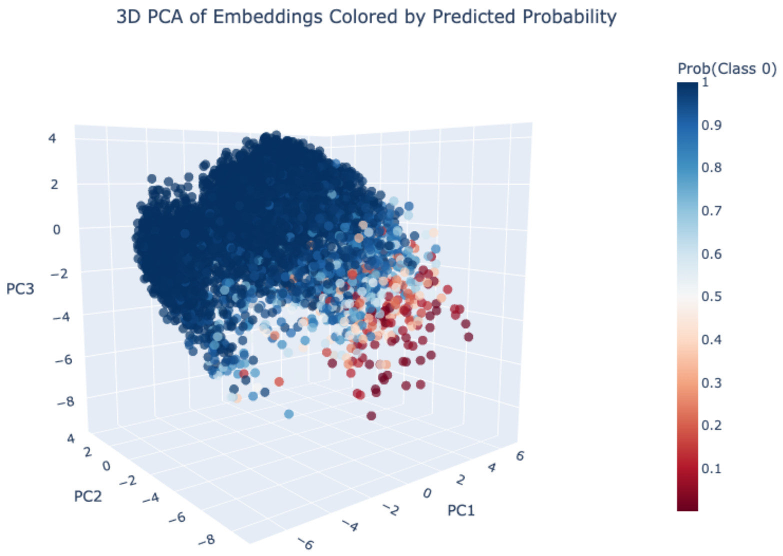

Figure 28: PCA of learned embeddings for the task-independent classifer for QM9 applied to the test dataset with no rotations. The misclassified examples thus are shown in red.

**Example Incorrectly Classified.** We select a sample classified incorrectly with low probability as being from the original dataset and investigate the classifier outputs per rotation angle, as shown in Figure 30.

**Example Close to the Decision Boundary.** We select also select an example from the non-augmented test set that the model assigns a 50% probability of belonging to the true dataset (correctly classified but close to the decision boundary).

It is interesting to note that for each example, we find instabilities in the decision boundary (rotations that are very close together but correspond to very large changes in the classifier output). This demonstrates that our method could perhaps be used to probe the instabilities of a given canonicalization – we know that each canonicalization has such instabilities (Dym et al., 2024), although we cannot guarantee that the instabilities in the model's predictions arise for this reason (and not e.g. due to a failure to learn). Nonetheless, the models probed achieved very high test accuracy, lending confidence that the identified example instabilities are genuine.

### D.5 Ablations

As shown in Table 7, the task-independent metric on QM9 is robust to the choice of architecture.

#### D.5.1 Hyperparameter ablations

We further ablate sample complexity, together with architecture and learning rate, for MNIST in Figure 32 and QM9 in Figure 33. To vary sample complexity (on the x-axes), we randomly select a subset of the original dataset of the specified size. As shown, there is little sensitivity to these factors, except when using a learning rate that is too large for the transformer architecture (but this is easily detectable from the loss curves). The greatest variation is visible at the lowest-sample regimes, but the classifier performance in all cases is still significantly better than random, which would be 50% accuracy (and recall that the optimal accuracy for MNIST is 85.7%, since the group of 90° rotations only has four elements). Overall, the metric is remarkably sample-efficient on these two datasets. This matches our intuition that the distributional symmetry-breaking is quite pronounced, as shown by the high accuracies, $m(p_X)$, for each. (In the language of Appendix B, we can think

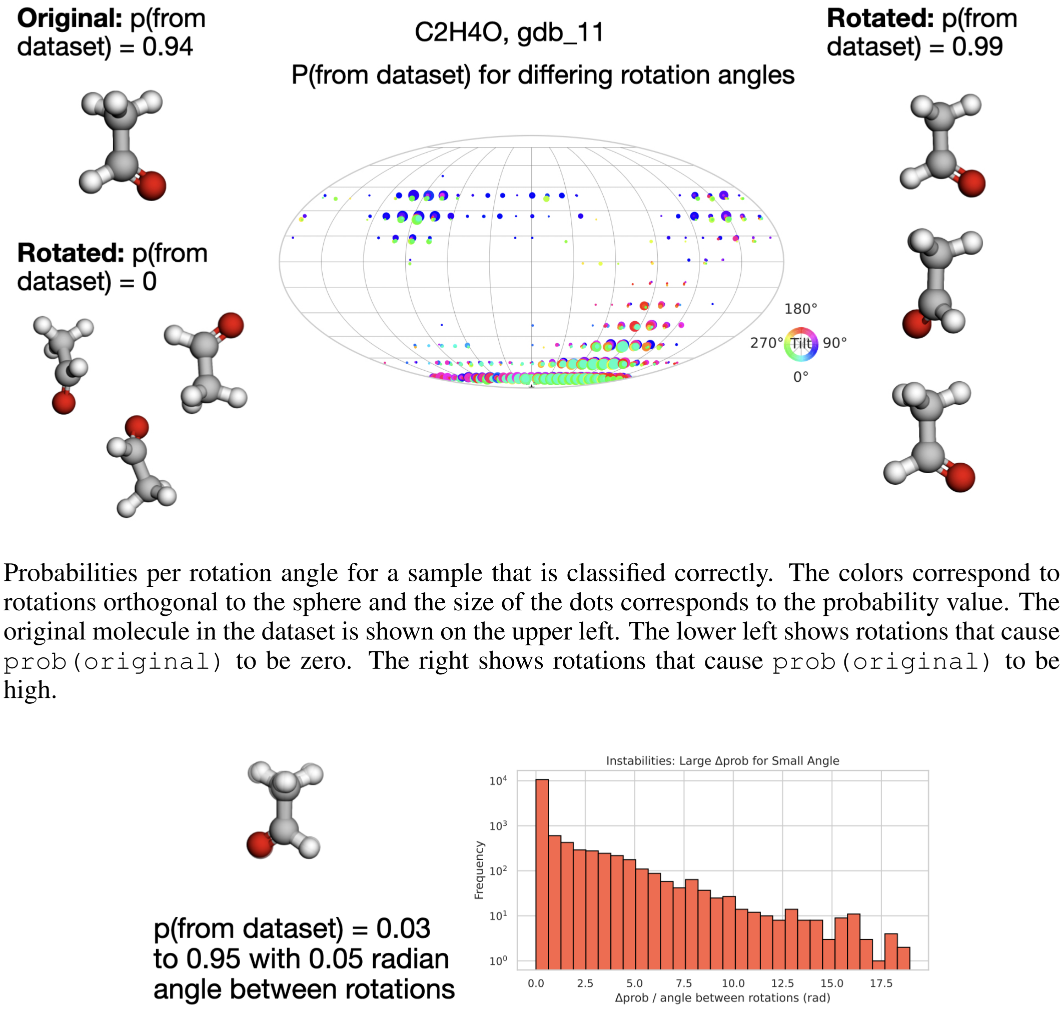

Probabilities per rotation angle for a sample that is classified correctly. The colors correspond to rotations orthogonal to the sphere and the size of the dots corresponds to the probability value. The original molecule in the dataset is shown on the upper left. The lower left shows rotations that cause `prob(original)` to be zero. The right shows rotations that cause `prob(original)` to be high.

Instability in the decision boundary (left): two nearby rotations cause a large change in predicted probability. Histogram (right): certain examples exhibit such instabilities more frequently.

Figure 29: Visualizations of classifier outputs for an example classified incorrectly.

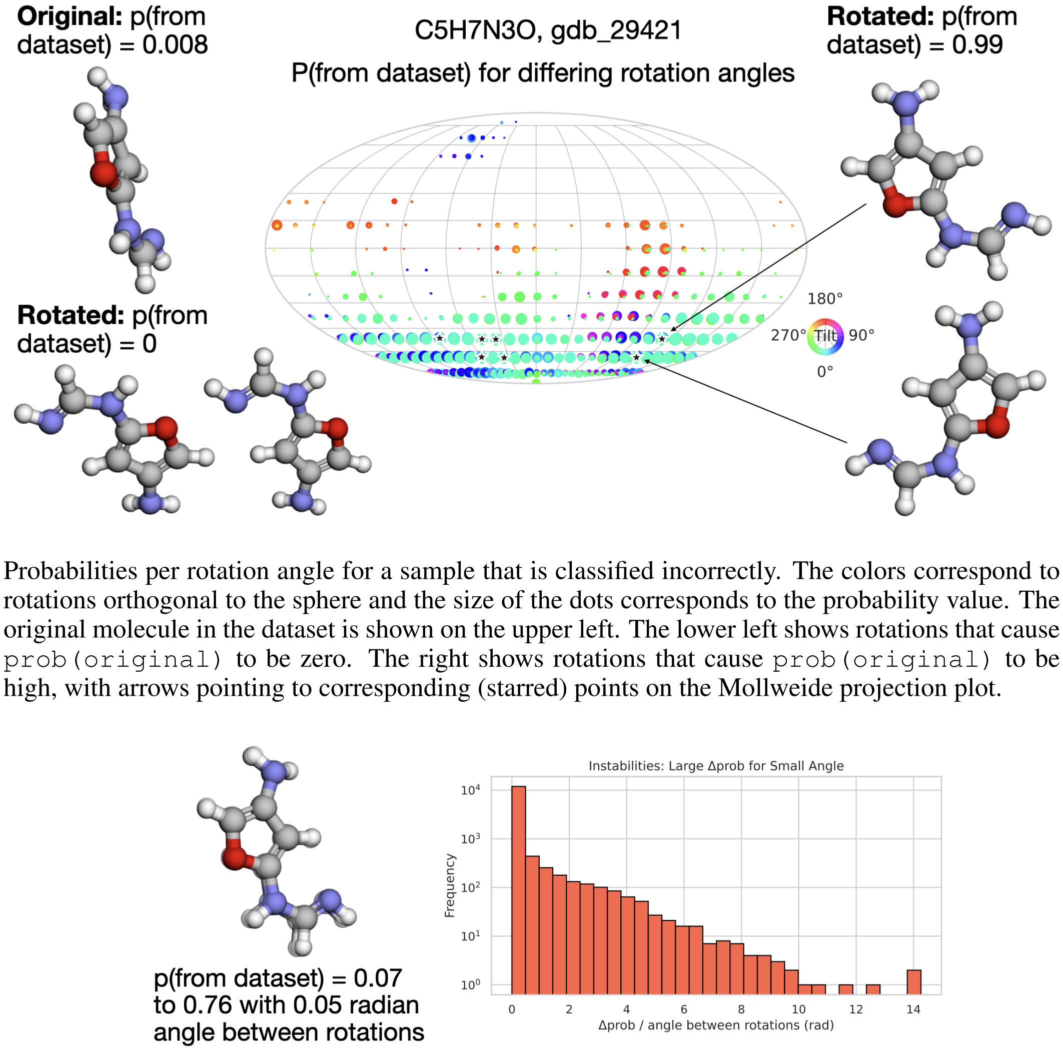

Probabilities per rotation angle for a sample that is classified incorrectly. The colors correspond to rotations orthogonal to the sphere and the size of the dots corresponds to the probability value. The original molecule in the dataset is shown on the upper left. The lower left shows rotations that cause `prob(original)` to be zero. The right shows rotations that cause `prob(original)` to be high, with arrows pointing to corresponding (starred) points on the Mollweide projection plot.

Instability in the decision boundary (left): two nearby rotations cause a large change in predicted probability. Histogram (right): certain examples exhibit such instabilities more frequently.

Figure 30: Visualizations of classifier outputs for an example classified incorrectly.

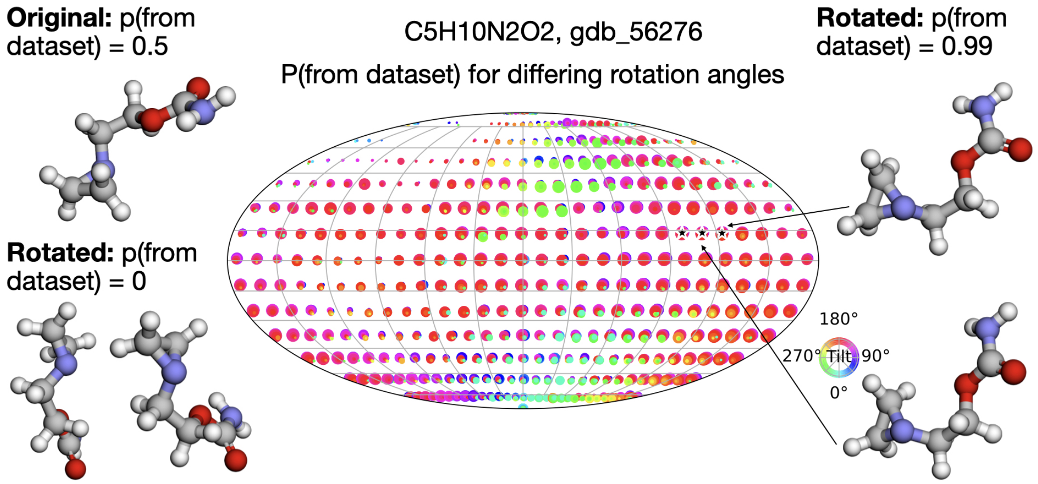

Probabilities per rotation angle for a sample on the decision boundary. The colors correspond to rotations orthogonal to the sphere and the size of the dots corresponds to the probability value. The original molecule in the dataset is shown on the upper left. The lower left shows rotations that cause `prob(original)` to be zero. The right shows rotations that cause `prob(original)` to be high, with arrows pointing to corresponding (starred) points on the Mollweide projection plot.

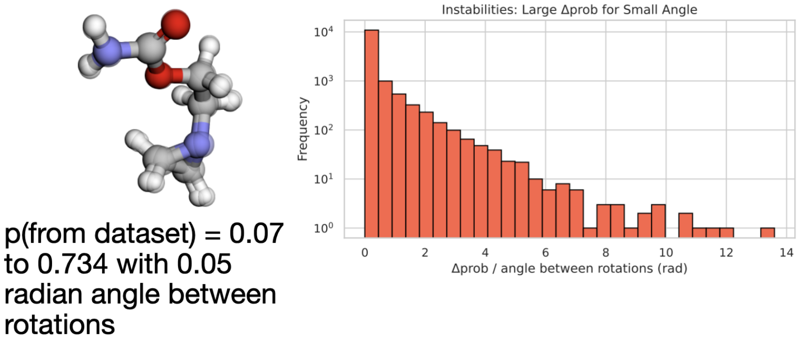

Instability in the decision boundary (left): two nearby rotations cause a large change in predicted probability. Histogram (right): certain examples exhibit such instabilities more frequently.

Figure 31: Visualizations of classifier outputs for an example close to the decision boundary.

Table 7: The classifier network is a transformer architecture, in which we vary the depth, number of heads, and hidden dimension. The task-independent metric is robust with respect to the architecture size.

| Setting | Depth | Heads | Hidden Dimension | Test Accuracy | Parameters |
|---|---|---|---|---|---|
| tiny | 2 | 2 | 64 | 98.3 | 110,000 |
| small_hidden | 4 | 4 | 64 | 98.6 | 210,000 |
| large_hidden | 4 | 4 | 256 | 98.4 | 3.2e6 |
| many_heads | 4 | 8 | 128 | 98.5 | 810,000 |
| shallow | 2 | 4 | 128 | 98.3 | 420,000 |
| micro | 2 | 2 | 32 | 98.0 | 27,000 |
| few_heads | 4 | 2 | 128 | 98.7 | 810,000 |
| deep | 8 | 4 | 128 | 98.7 | 1.6e6 |

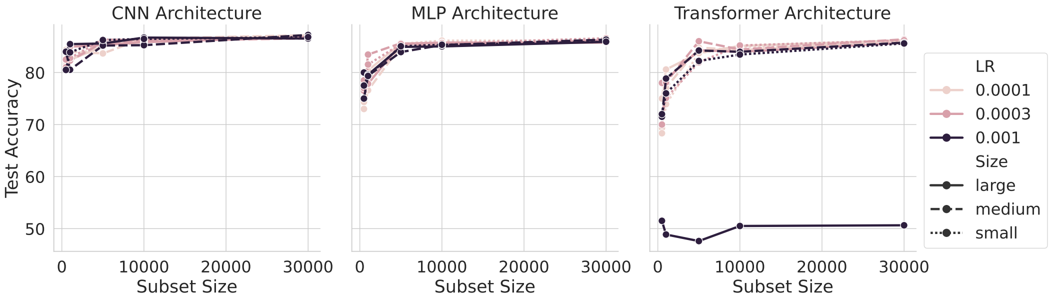

Figure 32: Ablations of $m(p_X)$ on MNIST with respect to architecture type, architecture size, learning rate, and dataset size. Curves are averaged over two random seeds.

of the hypothesis class/network family as being relatively simple; thus, the networks can be trained with even small fractions of each dataset.)

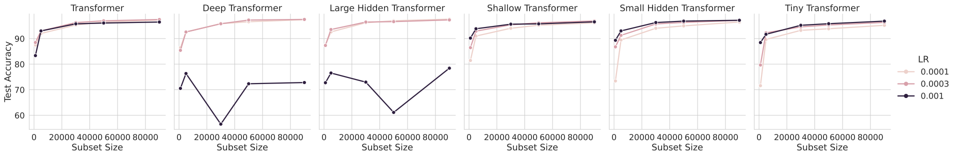

Figure 33: Ablations of $m(p_X)$ on QM9 with respect to architecture size, learning rate, and dataset size. Curves are averaged over two random seeds.

### D.6 Local QM9

We have shown that the QM9 dataset is highly canonicalized, yet data augmentation and equivariant methods both perform well even on the original, canonicalized test set. This behavior is distinct from ModelNet40, where train-time augmentation impedes performance on the (also canonicalized) test set. This poses a question: why are equivariant methods so helpful for QM9, even though it's already canonicalized? We explore the hypothesis that locality is an important factor impacting performance (which would be captured by equivariant methods, but not canonicalization). In particular, we seek to understand whether local graph motifs in QM9 are *less canonicalized* — i.e. more likely to appear in a variety of rotations — than the full molecules. If true, then augmentation and equivariant architectures might both benefit from exposing the network to full group orbits of local motifs.

Concretely, our question is: do the local motifs present in QM9 graphs experience distributional symmetry breaking? To address this, we create a new dataset from the original QM9 dataset by randomly selecting three nodes from each molecule, and creating a new molecule fragment out of only each node and its neighborhood (as determined by its edges/bonds). As shown in Figure 34, this often includes repeated neighborhoods. This creates a dataset of size 392k. We first simply apply the task-independent detection metric, asking a network to distinguish between rotated and unrotated motifs. (All experimental and model details are preserved from the ordinary QM9 setting). As shown in Table 8, the local dataset has lower accuracy than the QM9 dataset. However, this does not provide a maximally fine-grained distinction between different kinds of distributional symmetry breaking. For example, suppose a molecule always appears in one of two possible canonicalizations. With an infinite group like $SO(3)$, this detection problem is still likely to be perfectly solvable, as two orientations are still only a measure zero set of $SO(3)$. Yet, this case is distinct from the perfectly canonicalized case.

To assess whether a dataset is truly canonicalized, we train a network to predict $g$ from $gx$, where $g$ is drawn randomly from the Haar measure. **Solving this task to high accuracy is only possible when the distribution is truly canonicalized (only one element per orbit appears).** We use the same transformer architecture to output 9 values as the entries of a rotation matrix, and trained it according to the MSE. (Neither backpropagating through a Gram-Schmidt procedure to make it a proper rotation matrix, nor training an equivariant architecture, nor backpropagating through the angle of rotation error instead of the MSE, were as effective as this simple method, which also circumvents the symmetry-breaking that would be required to output a group element on symmetric inputs (Smidt et al., 2021).) As shown in Table 9, there is a discrepancy between the best test accuracy achieved on the original QM9 dataset, and that achieved on the local neighborhood version. **Therefore, it appears that the original QM9 dataset is more canonicalized, whereas the local motifs presented in the QM9 dataset can appear in several orientations (although still far from uniform over $SO(3)$).** This provides some evidence for the hypothesis that methods which involve equivariance to local motifs – including data augmentation and equivariance, but not canonicalization – may be providing an additional advantage on QM9.

As shown in Figure 35, it also took much longer to train these models (500 epochs took 6 hours on the original QM9 dataset, and nearly 15 hours on the local QM9 dataset, likely due to slower dataloading), which contrasts with the efficient convergence (around 30 minutes) of our main task-independent detection metric.

| $m(p_X)$ | Local QM9 | Global QM9 |
|---|---|---|
| Original | 67.6% | 98.5% |
| Rotated | 49.9% | 49.5% |
| Canonicalized | 99.8% | 99.8% |

Table 8: Distinguishing the distribution from its randomly rotated version, as well as sanity checks with artificially rotated and canonicalized datasets.

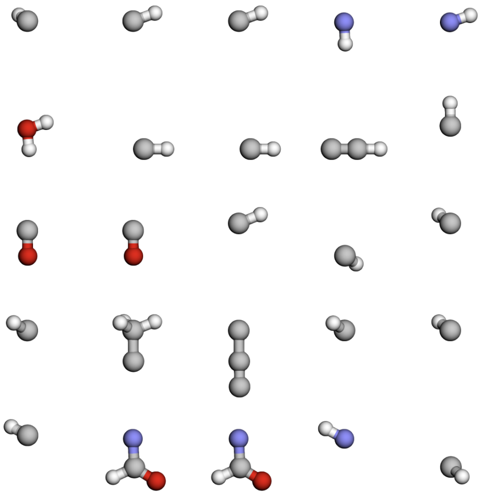

Figure 34: Local QM9 dataset visualization.

| | QM9 | Local QM9 |
|---|---|---|
| Test Error (degrees) | 13.5 | 53.7 |

Table 9: Predicting $g$ from $gx$.

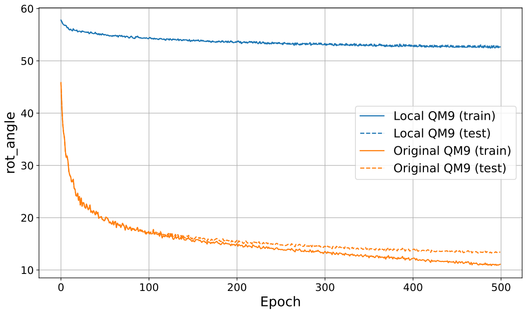

Figure 35: QM9 and local QM9 dataset training curves for predicting $g$ from $gx$.

## D.7 QM7B

### D.7.1 Dataset Details

In (Yang et al., 2019), density functional theory (DFT) and linear-response coupled-cluster theory including single and double excitations (LR-CCSD) is used to compute vector and tensorial molecular response properties for the 7,211 molecules in the QM7b database (Blum & Reymond, 2009; Montavon et al., 2013). LR-CCSD is generally more computationally expensive (scaling $O(N_e^6)$ with the number of electrons $N_e$) yet more accurate than DFT, which scales as $O(N_e^3)$. As the QM7b dataset is composed of small molecules, computing material response properties with LR-CCSD is feasible. Quantities computed include the dipole vector $\vec{\mu}$, polarizability $\boldsymbol{\alpha}$, and quadrupole moment $\boldsymbol{Q}$. The molecular dipole polarizability $\boldsymbol{\alpha}$ describes the tendency of a molecule to form an induced dipole moment in the presence of an external electric field (Yang et al., 2019). It can be computed by taking the second derivative of the electronic energy $U$ with respect to an applied electric field $\vec{E}$:

$$\alpha_{ij} = \frac{\partial^2 U}{\partial E_i \partial E_j}. \tag{62}$$

Scalar polarizability response quantities are the isotropic polarizability $\alpha_{\text{iso}}$ and the anistropic polarizability $\alpha_{\text{aniso}}$

$$\alpha_{\text{iso}} = \frac{1}{3}(\alpha_{\text{xx}} + \alpha_{\text{yy}} + \alpha_{\text{zz}}) \tag{63}$$

$$\begin{aligned}\alpha_{\text{aniso}} \quad = \quad & \tfrac{1}{\sqrt{2}}\Big[(\alpha_{\text{xx}} - \alpha_{\text{yy}})^2 + (\alpha_{\text{yy}} - \alpha_{\text{zz}})^2 \\ & +(\alpha_{\text{zz}} - \alpha_{\text{xx}})^2 + 6(\alpha_{\text{xy}}^2 + \alpha_{\text{xz}}^2 + \alpha_{\text{yz}}^2)\Big]^{1/2}\end{aligned} \tag{64}$$

The dipole moment is the first derivative:

$$\vec{\mu} = \frac{\partial U}{\partial \vec{E}}. \tag{65}$$

The quadrupole moment $\boldsymbol{Q}$ is a rank-2 tensor that characterizes the second-order spatial distribution of the molecular charge density, capturing deviations from spherical symmetry and providing information about the shape and anisotropy of the electron cloud beyond the dipole approximation:

$$Q_{ij} = \sum_{\alpha} q_\alpha \left(3 r_{\alpha i} r_{\alpha j} - \delta_{ij} r_\alpha^2\right). \tag{66}$$

$q_\alpha$ is the charge of particle $\alpha$, $\hat{r}_{\alpha i}$ is its $i$-th coordinate operator relative to the molecular center of mass, and $\delta_{ij}$ is the Kronecker delta.

Data can be downloaded from `https://archive.materialscloud.org/record/2019.0002/v3`. For our studies, we use the most accurate level of theory available in the dataset—linear-response coupled cluster with single and double excitations (LR-CCSD)—in combination with the d-aug-cc-pVDZ (daDZ) basis set, to reduce basis set incompleteness error (Yang et al., 2019) (specifically, the file CCSD_daDZ.tar.gz available at the link above). The data is then converted from XYZ format into a `torch_geometric` dataset.

### D.7.2 Model and Training Details

For the task-independent metric, we use the same generic transformer used for QM9 to find that the dataset is canonicalized. We train for 100 epochs with a batch size of 128 and a learning rate of 1e-5 with the Adam optimizer. From (Yang et al., 2019), this is expected as the molecules were reordered using a kernel-based similarity measure from (Bartók et al., 2013). For the task-dependent metric, we use $c$ untrained, as we found that using $c$ trained allowed the network to learn the dipole vector itself. We use the same parameters as for the task-dependent metric for QM9.

For the regression tasks, we use the same graph transformer architecture as described in Appendix D.4 and compare to the same $E(3)$-equivariant neural network (now with a vector or $\ell = 2$ output rather than a scalar as in QM9)/group-averaged network with 5 sampled rotations. We train each for 500 epochs with a batch size of 128 on a single NVIDIA RTX A5000. The E3ConvNet model is trained with a learning rate of 1e-4 and the Graphormer model is trained with a learning rate of 3e-5, both with the Adam optimizer. As anticipated, the $E(3)$-equivariant model achieves better performance than the Graphormer in predicting dipole moments, owing to its physically consistent treatment of vector-valued (non-scalar) quantities.

### D.7.3 Task-Relevant Canonicalization

To investigate the impacts of a task-relevant canonicalization, we run further experiments on the QM7b dataset. Consider aligning molecules such that their dipole moments coincide with the z-axis, filtering for molecules with non-zero dipole moments. This canonicalization clearly makes it easier for a non-equivariant model to solve the task, whereas an equivariant model will be unable to use this information. We test different data augmentation settings to illustrate the impacts of the task-useful canonicalization (train/test aug=TT, train aug only=TF, test aug only=FT, no aug=FF). Values reported in the table below are the MAE across the dipole vector components in atomic units (a.u). For the task-useful canonicalization, the FF setting (train/test fully canonicalized by dipole, no augmentation) outperforms the equivariant model (shown in bold). In the original dataset without canonicalizing based on the dipole, FF does not outperform the equivariant model. These results provide an interesting avenue for future work/for testing the task-dependent metric.

Table 10: Comparison of different augmentation types and models for dipole prediction. Lower values are better.

| Aug. Type / Model | TT | FF | TF | FT | e3nn | Group Ave 5 rot | Group Ave 10 rot |
|---|---|---|---|---|---|---|---|
| Dipole Canon | 0.057 | **0.034** | 0.055 | 0.16 | 0.043 | 0.044 | 0.042 |
| Orig Dataset | 0.055 | 0.104 | 0.054 | 0.16 | 0.043 | 0.044 | **0.042** |

### D.7.4 Loss Curves

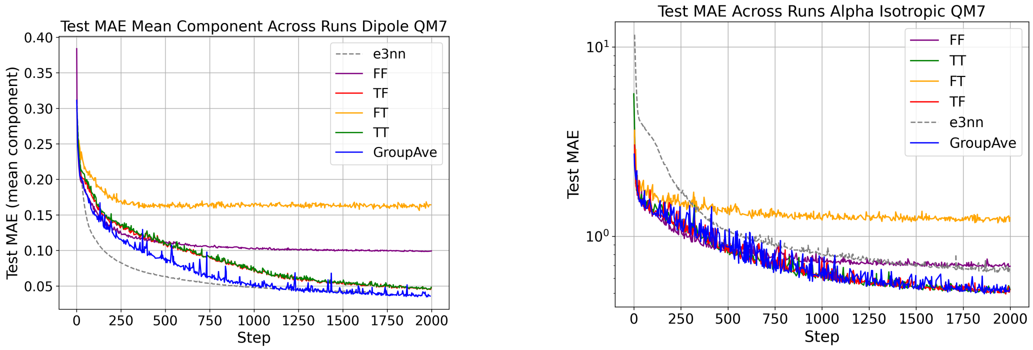

Figure 36: (left) Test MAE per epoch for predicting the dipole moment QM7b (with the e3nn model/group averaged shown for reference). (right) Test MAE per epoch for predicting the isotropic component of the $\alpha$ tensor.

### D.8 RMD17

We use the revised MD17 dataset Christensen & von Lilienfeld (2020), as the original MD17 dataset has a high level of numerical noise (Chmiela et al., 2017). The revised MD17 dataset was calculated with a more accurate DFT functional/convergence criteria than the original MD17. For this dataset, we currently have explored the task-independent metric. We use the provided five train/test splits from `https://figshare.com/articles/dataset/Revised_MD17_dataset_rMD17_/12672038` and train a separate model for each molecule. Note it is not recommended to train a model on more than 1,000 samples from rMD17 Christensen & von Lilienfeld (2020), even though the dataset has 100,000 conformers for each trajectory. We train a generic transformer with 812k parameters for 50 epochs on the train/test splits provided with the Adam optimizer at learning rate `1e-5` and batch size `128`.

As seen in Figure 37, all molecules are canonicalized. However, the task-independent metric of test accuracy yields significantly different values per molecules. For example, aspirin has a test accuracy of 97.869%, but ethanol yields 79.834 %. In Figure 37, ethanol and malohaldehyde have a noticeably lower degree of canonicalization.

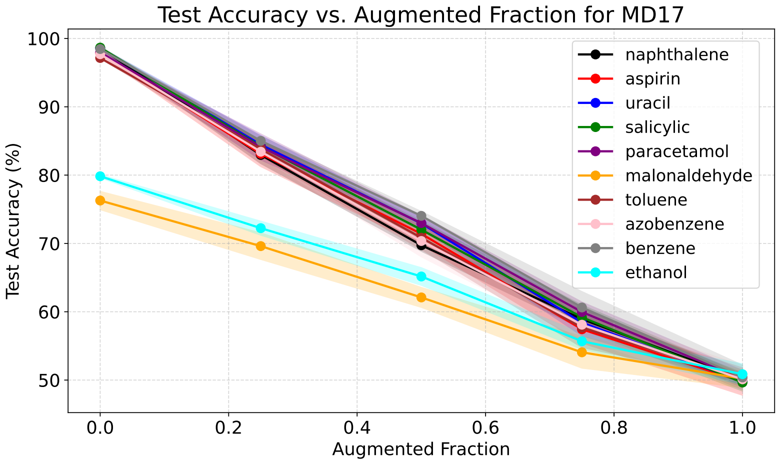

Figure 37: Test accuracy vs. augmented fraction for all molecules in rMD17. Note the difference between the 8 more canonicalized molecules and ethanol/malonaldehyde.

Figure 39 demonstrates the values used in our computation of the p-values for each method (on a row) and different levels of augmentation in the detection dataset (column) for one of the molecules in rMD17 (benzene). The p-value plots were computed using 20 samples (for each histogram) of size 1k corresponding to the given train/test splits, trained for 20 epochs (in the case of the classifier metric). As shown, all methods separate the calibration distances from the actual distances, resulting in identical, statistically significant p-values. As the tests are asked to distinguish between increasingly similar datasets (moving from left to right), the histograms gradually move closer together, until they overlap. For ease of visualization, Figure 38 plots the mean distance computed from each histogram for benzene (excluding the calibration distances). We also plot the p-value vs. the augmented fraction Figure 40. The Chamfer and Hausdorff kernels exhibit similar trends to the classifier, and the naive mean/covar kernel exhibits less reasonable behavior. This illustrates the importance of choosing a good kernel and provides a relative advantage of our method. All other molecules in rMD17 exhibted similar trends for the p-values.

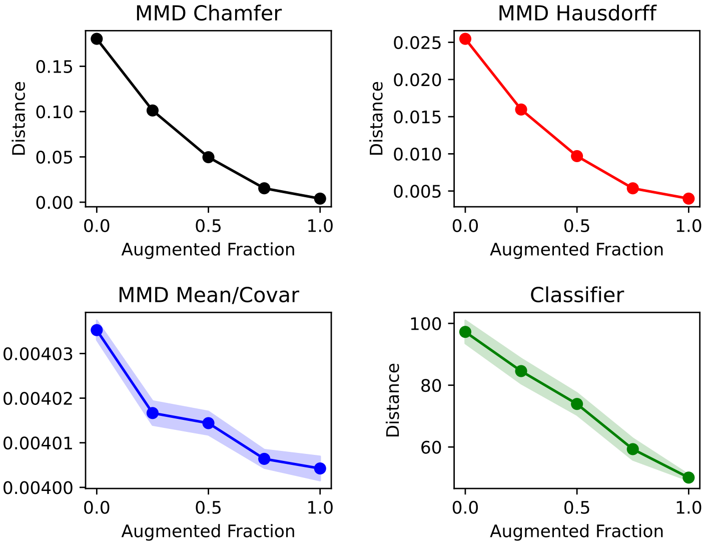

Figure 38: Different distance metrics from a perfectly symmetrized distribution, as a function of the degree of synthetic augmentation of the rMD17 dataset for benezene. (Higher augmented fraction indicates a greater similarity to the symmetrized distribution).

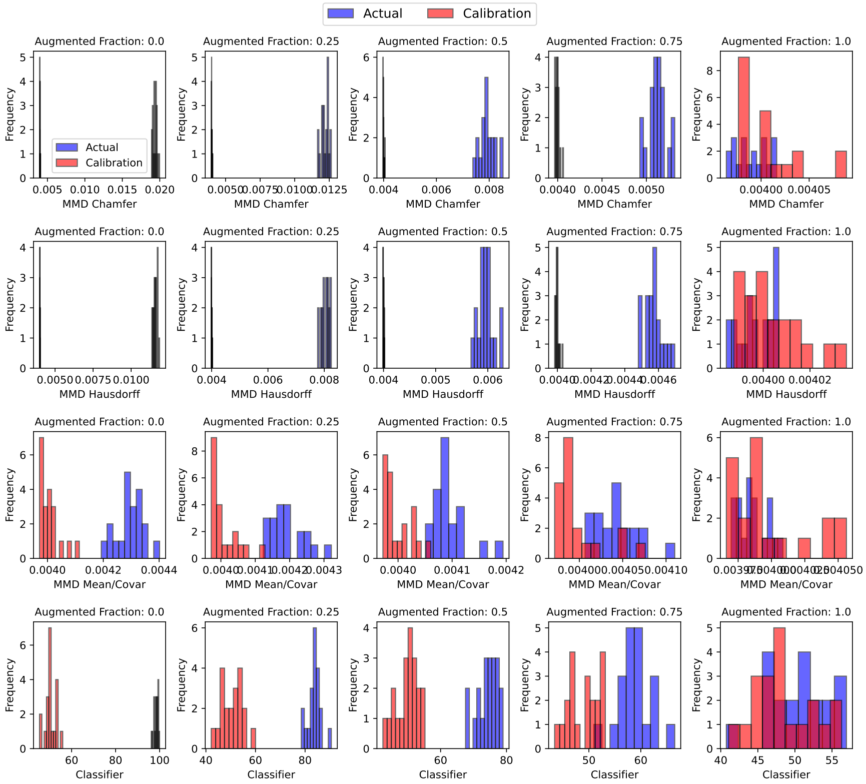

Figure 39: Distance metrics for different methods, and at different levels of augmentation for benzene (i.e. different levels of underlying distributional similarity).

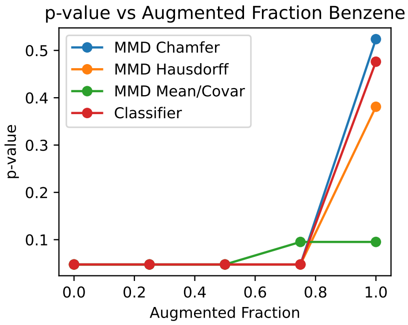

Figure 40: p-value vs augmented fraction for benzene rMD17.

### D.9 Open Catalyst Project 2020 (OC20)

For our study, we use the 200K subset from the structure to energy and forces (S2EF) task, available at https://fair-chem.github.io/core/datasets/oc20.html#structure-to-energy-and-forces-s2ef-task. For this dataset, we have explored the task-dependent metric. It would be interesting in the future to explore other tasks (e.g. Initial Structure to Relaxed Structure) and larger dataset sizes, as the OC20 dataset training set alone has 20 million structures. We use the preprocessing pipeline provided at https://fair-chem.github.io/core/datasets/oc20.html. Positions for each catalyst+adsorbate are tagged with 0: catalyst surface, 1: catalyst sub-surface, and 2: adsorbate. The unit cell for the catalyst is repeated twice in the $x$ direction, twice in the $y$ direction, and once in the $z$ direction, leading to the slab's alignment with the $xy$ plane. This alignment most likely trivially causes our metric to report distributional symmetry breaking. We also expect the adsorbate alone to be slightly less canonicalized than the combined catalyst surface–adsorbate system (as the adsorbate alone is not a periodically repeating slab). This is supported by the test accuracy, which is 96.529% for the adsorbate alone compared to 99.280% for the surface plus adsorbate system. It would thus be interesting in future work to consider how to treat periodic crystalline systems. The p-value plots were computed using 20 samples (for each histogram) of size 50k, trained for 20 epochs (in the case of the classifier metric). The p-values follow the expected trends as was the case for the other datasets.

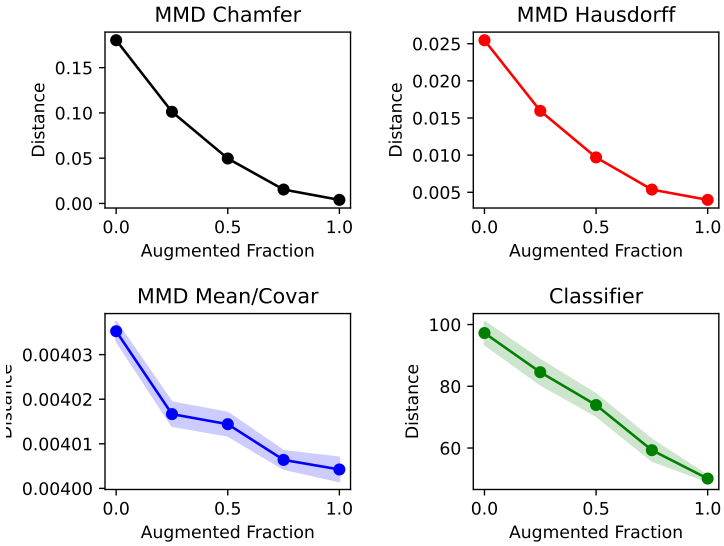

Figure 41: Different distance metrics from a perfectly symmetrized distribution, as a function of the degree of synthetic augmentation of the OC20 dataset. (Higher augmented fraction indicates a greater similarity to the symmetrized distribution).

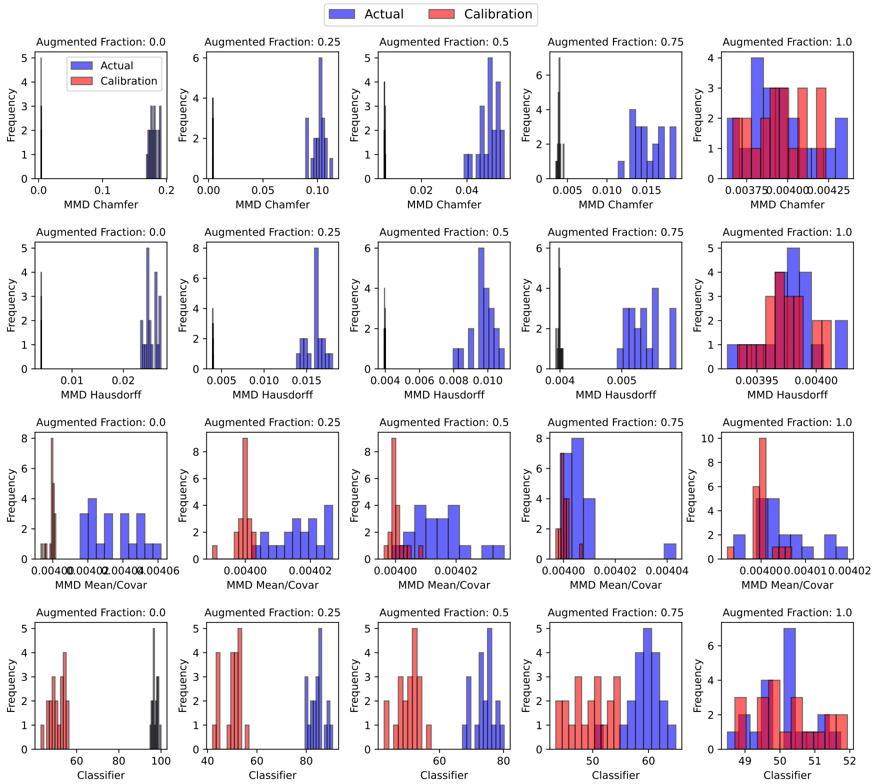

Figure 42: Distance metrics for different methods, and at different levels of augmentation for OC20 (i.e. different levels of underlying distributional similarity).

### D.10 Computation of p-values

Algorithm 2 outlines the process for computing p-values.

We sample $n_1$ training and test sets from the original dataset, apply a random rotation to each data point, and compute the distance between the two sets. This gives us a distribution of distances under the null hypothesis that the dataset is. We then sample $n_2$ training and test sets from the original dataset, apply a random rotation to a subset of the data, and compute the distance between the two sets. The mean of these distances is our test statistic. The p-value is then computed as the fraction of calibration distances that are greater than the test statistic.

**Algorithm 2** P-value Computation

```
Input: Training set $\mathcal{D}_{\text{train}}$, test set $\mathcal{D}_{\text{test}}$, calibration distances sample size $n_1$, actual distances
    sample size $n_2$, distance function Distance$(\cdot,\cdot)$.
Output: p-value
actual_dists ← []
calibration_dists ← []
                                        ▷ Compute calibration distances under null hypothesis
for $i = 1$ to $n_1$ do
    Sample training set $\tilde{\mathcal{D}}_{\text{train}}$ and test set $\tilde{\mathcal{D}}_{\text{test}}$ from $\mathcal{D}_{\text{train}}$ and $\mathcal{D}_{\text{test}}$.
    Apply rotation transformation to all data
    $d_c \leftarrow \text{Distance}(\tilde{\mathcal{D}}_{\text{train}}, \tilde{\mathcal{D}}_{\text{test}})$
    calibration_dists.append$(d_c)$
end for
                                        ▷ Compute actual distances
for $i = 1$ to $n_2$ do
    Sample training set $\tilde{\mathcal{D}}'_{\text{train}}$ and test set $\tilde{\mathcal{D}}'_{\text{test}}$ from $\mathcal{D}_{\text{train}}$ and $\mathcal{D}_{\text{test}}$.
    Apply rotation transformation to subset of data
    $d_a \leftarrow \text{Distance}(\tilde{\mathcal{D}}'_{\text{train}}, \tilde{\mathcal{D}}'_{\text{test}})$
    actual_dists.append$(d_a)$
end for
$\bar{d}_a \leftarrow \frac{1}{n_2}\sum_{i=1}^{n_2}$ actual_dists$[i]$          ▷ Compute mean of actual distances
count ← $|\{d_c \in \text{calibration\_dists} : d_c > \bar{d}_a\}|$
$p$-value ← $\frac{1+\text{count}}{1+n_1}$
    return $p$-value
```

### D.11 Maximum Mean Discrepancy (MMD) for Point Clouds

#### D.11.1 Maximum Mean Discrepancy (MMD)

MMD is a statistical distance metric that measures the discrepancy between two probability distributions $p_0, p_1$. Unlike many other distance metrics, MMD does not require any assumptions about the distributions or explicit density estimation. Thus, MMD is useful for high-dimensional or complex distributions. The definition of MMD is:

$$\text{MMD}^2(p_0,p_1) = \mathbb{E}_{x_0,x_0'\sim p_0}\left[k(x_0,x_0')\right] + \mathbb{E}_{x_1,x_1'\sim p_1}\left[k(x_1,x_1')\right] - 2\mathbb{E}_{x_0\sim p_0,x_1\sim p_1}\left[k(x_0,x_1)\right],$$

Where $k(\cdot,\cdot)$ is the kernel function. To compute the MMD, we can use the empirical MMD, which is an unbiased estimator of the true MMD and only needs a set of samples from each distribution. Algorithm D.11.1 provides pseudocode for the implementation of empirical MMD.

To compute the MMD, we need to choose a kernel function that is positive definite and characteristic. The choice of kernel can have a significant impact on the MMD value. Based on natural distance measures between point clouds, we implement three different kernels for our experiments: the naive kernel (Mean/Covar), the Chamfer distance kernel, and the Hausdorff distance kernel.

**Algorithm 3** Compute Maximum Mean Discrepancy (MMD)

```
Require: $x, y$ (input samples), $mask\_x, mask\_y$ (optional masks), $kernel\_func$ (kernel function)
$n_x \leftarrow$ length of $x$, $n_y \leftarrow$ length of $y$          ▷ Compute XX pairwise similarities
$xx\_indices \leftarrow$ upper triangular indices of $(n_x, n_x)$
if $mask\_x$ is not None then
    $xx\_distances \leftarrow kernel\_func(x[xx\_indices_0], x[xx\_indices_1],$
            $mask\_x[xx\_indices_0], mask\_x[xx\_indices_1])$
    $xx\_diag \leftarrow kernel\_func(x, x, mask\_x, mask\_x)$
else
    $xx\_distances \leftarrow kernel\_func(x[xx\_indices_0], x[xx\_indices_1])$
    $xx\_diag \leftarrow kernel\_func(x, x)$
end if
$xx\_mean \leftarrow \frac{2\sum xx\_distances + \sum xx\_diag}{n_x \cdot n_x}$
                                                  ▷ Compute YY pairwise similarities
$yy\_indices \leftarrow$ upper triangular indices of $(n_y, n_y)$
if $mask\_y$ is not None then
    $yy\_distances \leftarrow kernel\_func(y[yy\_indices_0], y[yy\_indices_1],$
            $mask\_y[yy\_indices_0], mask\_y[yy\_indices_1])$
    $yy\_diag \leftarrow kernel\_func(y, y, mask\_y, mask\_y)$
else
    $yy\_distances \leftarrow kernel\_func(y[yy\_indices_0], y[yy\_indices_1])$
    $yy\_diag \leftarrow kernel\_func(y, y)$
end if
$yy\_mean \leftarrow \frac{2\sum yy\_distances + \sum yy\_diag}{n_y \cdot n_y}$
                                                  ▷ Compute XY cross similarities
if $mask\_x$ is not None and $mask\_y$ is not None then
    $xy\_distances \leftarrow kernel\_func(x[:, None], y[None, :],$
            $mask\_x[:, None], mask\_y[None, :])$
else
    $xy\_distances \leftarrow kernel\_func(x[:, None], y[None, :])$
end if
$xy\_mean \leftarrow$ mean of $xy\_distances$
                                                  ▷ Compute final MMD value
$mmd \leftarrow xx\_mean + yy\_mean - 2 \cdot xy\_mean$
    return $mmd$
```

### D.11.2 Naive Kernel (Mean/Covar)

The most naive way to compute the distance between point clouds is to compute the distance between their respective means and covariances. We call this method "MMD Mean/Covar", as well as the naive kernel. Since the naive kernel only uses the means and covariances of the point clouds, it lacks the ability to capture the local information of the point clouds. AlgorithmD.11.2 gives an implementation of the Naive kernel:

**Algorithm 4** Naive Kernel Computation

```
Require: $x, y$ (input tensors), $mask\_x, mask\_y$ (optional masks, related to the variable numbers of
    nodes across input molecules), $\sigma$ (scaling parameter)
                                        ▷ Compute mean and covariance with or without masks
    if $mask\_x$ is not None and $mask\_y$ is not None then
        $mean_x \leftarrow \frac{\sum x}{\sum mask\_x}$
        $mean_y \leftarrow \frac{\sum y}{\sum mask\_y}$
        $cov_x \leftarrow \frac{\sum xx^T}{\sum mask\_x}$
        $cov_y \leftarrow \frac{\sum yy^T}{\sum mask\_y}$
    else
        $mean_x \leftarrow$ mean of $x$, $mean_y \leftarrow$ mean of $y$
        $cov_x \leftarrow \frac{\sum xx^T}{|x|}$
        $cov_y \leftarrow \frac{\sum yy^T}{|y|}$
    end if
                                        ▷ Compute embeddings
    $embedding_x \leftarrow$ concatenate($mean_x$, flatten($cov_x$))
    $embedding_y \leftarrow$ concatenate($mean_y$, flatten($cov_y$))
                                        ▷ Compute pairwise distance and apply Gaussian kernel
    $dist \leftarrow ||embedding_x - embedding_y||$
    $kernel\_val \leftarrow \exp(-dist^2/\sigma)$
        return $kernel\_val$
```

### D.11.3 Chamfer Distance Kernel

The Chamfer distance is a commonly used distance metric, measuring the similarity between two point clouds. It is defined as the sum of the average of squared Euclidean distances from each point in one set to its nearest neighbor in the other set. Formally, the Chamfer distance is defined as:

$$\mathrm{CD}(X,Y) = \frac{1}{|X|}\sum_{x\in X}\min_{y\in Y}||x-y||^2 + \frac{1}{|Y|}\sum_{y\in Y}\min_{x\in X}||x-y||^2,$$

where $X$ and $Y$ are two point clouds, $x$ and $y$ are points in the point clouds, and $||x-y||$ is the Euclidean distance between points $x$ and $y$.

Since the Chamfer distance kernel uses the minimum distance between points, it mainly captures local information, and always ignores global structure (such as the overall shape distribution and point cloud density). AlgorithmD.11.3 gives an implementation of Chamfer distance kernel.

### D.11.4 Hausdorff Distance Kernel

The Hausdorff distance is also a distance metric that measures the distance between two sets of points. By replacing the average operation in Chamfer distance with the maximum operation, we obtain the Hausdorff distance as:

$$\mathrm{HD}(X,Y) = \max\left(\max_{x\in X}\min_{y\in Y}||x-y||, \max_{y\in Y}\min_{x\in X}||x-y||\right).$$

**Algorithm 5** Chamfer Kernel Computation

```
Require: $x, y$ (input tensors), $mask\_x, mask\_y$ (optional masks), $\sigma$ (scaling parameter)
                                                    ▷ Compute Chamfer distances
$dist_1 \leftarrow$ minimum pairwise Euclidean distance from $x$ to $y$
$dist_2 \leftarrow$ minimum pairwise Euclidean distance from $y$ to $x$
                                                    ▷ Handle masks if provided
if $mask\_x$ is not None and $mask\_y$ is not None then
    $masked\_min\_dist_1 \leftarrow dist_1 \cdot mask\_x$
    $masked\_min\_dist_2 \leftarrow dist_2 \cdot mask\_y$
    $chamfer\_dist \leftarrow \frac{1}{2}\left(\frac{\sum masked\_min\_dist_1}{\sum mask\_x} + \frac{\sum masked\_min\_dist_2}{\sum mask\_y}\right)$
else
    $chamfer\_dist \leftarrow \frac{1}{2}\left(\text{mean}(dist_1) + \text{mean}(dist_2)\right)$
end if
                                                    ▷ Apply Gaussian kernel transformation
$kernel\_val \leftarrow \exp\left(-\frac{chamfer\_dist}{2\sigma^2}\right)$
    return $kernel\_val$
```

Because the Hausdorff distance kernel uses the maximum distance between points, it is more sensitive to outliers than Chamfer distance. AlgorithmD.11.4 gives an implementation of Hausdorff distance kernel.

**Algorithm 6** Hausdorff Kernel Computation

```
Require: $x, y$ (input tensors), $mask\_x, mask\_y$ (optional masks), $\sigma$ (scaling parameter)
                                                    ▷ Compute pairwise minimum distances
$dist_1 \leftarrow$ minimum pairwise Euclidean distance from $x$ to $y$
$dist_2 \leftarrow$ minimum pairwise Euclidean distance from $y$ to $x$
                                                    ▷ Handle masks if provided
if $mask\_x$ is not None and $mask\_y$ is not None then
    $masked\_dist_1 \leftarrow dist_1 \cdot mask\_x$
    $masked\_dist_2 \leftarrow dist_2 \cdot mask\_y$
    $hausdorff\_dist \leftarrow \max\left(\max(masked\_dist_1), \max(masked\_dist_2)\right)$
else
    $hausdorff\_dist \leftarrow \max\left(\max(dist_1), \max(dist_2)\right)$
end if
                                                    ▷ Apply Gaussian kernel transformation
$kernel\_val \leftarrow \exp\left(-\frac{hausdorff\_dist}{2\sigma^2}\right)$
    return $kernel\_val$
```